UNIVERSITY OF CALIFORNIA,
IRVINE

Thermal Desorption Studies of Deuterium Oxide on Catalytically Relevant Metal Oxide Systems

DISSERTATION

submitted in partial satisfaction of the requirements
for the degree of

DOCTOR OF PHILOSOPHY

in Chemistry

by

Anthony D. Babore

Dissertation Committee:
Professor John C. Hemminger, Chair
Associate Professor Matt Law
Assistant Professor Shane Ardo

2018

DEDICATION

To:

My wonderful parents for their endless love and support

My lovely sisters for keeping life interesting and humorous

The boys for a never-ending supply of good times

My (*way* too many) hobbies for giving me balance

And

My amazing girlfriend Megan for awesome adventures,
constant encouragement, and for keeping me sane

In loving memory of
Bette Babore-Ulasevich
1921 – 2016

"You can go right or left, but you can't very well do both at once."
– Bruce Brown

TABLE OF CONTENTS

LIST OF FIGURES

LIST OF TABLES

ACKNOWLEDGMENTS

Perhaps a whole chapter of this thesis could be dedicated to the many people deserving of my utmost appreciation; for without them, none of this would be possible. But for the sake of the reader, I will attempt to limit myself to just this one page.

I first offer my deepest appreciation to my advisor, Professor John Hemminger. Obviously, none of this work would be possible without him, but more importantly he is a great role model whose depth of knowledge never ceases to amaze me. In addition, I truly value his sense of humor and good nature; it has ultimately made the time I have spent as a graduate student nothing but an enjoyable experience. I would also like to thank my other Committee members, Professor Matt Law and Professor Shane Ardo for pushing me to reach my highest potential. Furthermore, I am truly appreciative for all of the guidance of Professor Sergey Nizkorodov as well as my undergraduate advisors, Professor Louise Sowers and Professor Marc Richard, and my high school teacher Robert Citta who sparked my interest in chemistry.

I offer a most sincere thank you to my parents, Keith and Anna, for their immense love and guidance as well as their tremendous amount of support (especially for supporting my decision to move across the country). Also, I would like to thank my sisters, Kristina and Francesca, for being a constant source of laughs and entertainment, and the rest of my family for always being there for me. A very special thank you to my beautiful girlfriend Megan for every little thing she does, she brings out the best in me and makes life a never-ending adventure, for which I cannot appreciate enough.

Throughout out my time spent at UCI, I have made some amazing friendships that have provided an incalculable amount of good times. I would first like to acknowledge "The Ogle Street Blues Band", comprised of some of my best friends (and current roommates): Tyler, Jack and Stefan. I would also like to acknowledge the rest of "the boys", Josh, Luke, Tristan, and Deli, they are all truly good people, and I am forever grateful for their friendship. I must also thank Mallory Hinks and Alex White, who were integral in my success during advancement to candidacy, and for being great friends on top of it all. I would also like to mention my friends Stacey, Christina, Nate, Lucas, Kyle and Will (among countless others) for many beers shared and for just being an awesome group of people.

Last but certainly not least, I would like to thank the past and present Hemminger Group members (in no particular order). Past: Dr. James Taing, Dr. Paolo Reyes, Dr. Marijke Van Spyk, Dr. Safa Khan, Dr. Theresa McIntire, Dr. Alexandra Margarella, Dr. Yu Liu, Dr. Jayde Kwon, Dr. Michael Makowski, Fabian Rosner, Dr. Guofeng Sun, and Dr. Kathryn Perrine. Present: Joel Langford, Jarred Bruce, Amanda Haines, Dr. Randima Galhanage, Dr. Djawhar Ferrah, and Mohammed Alam. I have enjoyed interacting with all of these excellent people over the course of my doctoral studies and the countless scientific discussions that have ultimately educated me far beyond I thought possible. I must draw special attention to Dr. Kathryn Perrine who mentored me at the start of my graduate career and laid the foundation of my surface science and temperature programmed desorption know-how. Finally, I am extremely grateful for Jared Bruce for all his motivation, countless discussions, lunch outings, 2pm coffee strolls, and for being a great friend and coworker.

CURRICULUM VITAE

ANTHONY D. BABORE

205 Ogle Street #A, Costa Mesa, CA 92627 | (609)-287-4054 | ababore@uci.edu

EDUCATION

University of California Irvine
Irvine, CA
Ph.D. in Analytical Chemistry **2018**

University of California Irvine
Irvine, CA
M.S. in Chemistry **2017**

Stockton University
Pomona, NJ
B.S. in Chemistry **2012**

AWARDS

Research Poster Contest Winner **2012**

Who's Who Among Students in American Universities & Colleges Award **2011**

Research Experience for Undergraduate funding **2011**

Research Experience for Undergraduate funding **2010**

TEACHING EXPERIENCE

University of California, Irvine
Teaching Assistant – General Chemistry Laboratory (CHEM 1LC) **Spring 2013**
Prepared introductory lessons for each laboratory, performed experimental troubleshooting, graded lab reports and exams and administered and assisted students performing experiments

Teaching Assistant – General Chemistry Laboratory (CHEM 1LE) **Winter 2013**
Prepared introductory lessons for each laboratory, performed experimental troubleshooting, graded lab reports and exams and administered and assisted students performing experiments

Teaching Assistant – General Chemistry Laboratory (CHEM 1LD) **Fall 2012**
Prepared introductory lessons for each laboratory, performed experimental troubleshooting, graded lab reports and exams and administered and assisted students performing experiments
Richard Stockton College of New Jersey

Teaching Assistant – Physical Chemistry Laboratory (CHEM 3420) **Spring 2012**
Oversaw and assisted students performing experiments, demonstrated proper use of the differential scanning calorimeter for students.

Teaching Assistant – Experiential Chemistry (GNM 2148) **Spring 2011**
Oversaw and assisted students performing experiments, was expected to ask questions to encourage students to think about their experimental observations.

RESEARCH EXPERIENCE

University of California, Irvine
Graduate Student Researcher **2012 - 2018**
Developed an in depth understanding of the operation of ultra-high vacuum (UHV) systems and accompanying surface sensitive analytical techniques. Performed thermal desorption experiments on thin films and nanoparticles supported on highly oriented pyrolytic graphite. Performed thermal desorption experiments on sulfur doped oxide films on W (100). Gained knowledge in the operation of Auger electron spectroscopy and X-ray photoelectron spectroscopy. Performed troubleshooting for instrumentation and UHV equipment.

Stockton University
Undergraduate Researcher **2010 - 2012**
Gained knowledge of the research process, prepared standard solutions of trace explosives, developed gas chromatograph/ mass spectrometer methods for the analysis of trace explosive solutions, constructed and optimized a GC autosample-tray chiller, and studied the degradation of trace explosive solutions as a function of time and temperature.

PUBLICATIONS AND PRESENTATIONS

"Thermal desorption of D2O on TiO2 heterostructures supported on HOPG", A.D. Babore, K.A. Perrine, P. Reyes, J. Taing and J.C. Hemminger *Manuscript in preparation* (2018)

"Photodeposition/reduction of Pt oxide nanoparticles on TiO2 nanoparticles supported on HOPG", J.P. Bruce, A.D. Babore, R. Galhanage and J.C. Hemminger. *Manuscript in preparation* (2018)

“Water desorption from sulfur-doped oxide thin films on W (100)”, A.D. Babore and J.C. Hemminger. *Manuscript in preparation* (2018)

“Water desorption from sulfur-doped oxide thin films on W (100)”, A.D. Babore and J.C. Hemminger. Presented at AVS International Symposium & Exhibition, Nashville, TN (2016)

"Effect of Temperature on the Stability of Trace Explosives Using Gas Chromatography”, A.D. Babore and S.P. Cleary. Presented at Galloway Township high school, Pomona, NJ (2012)

"The stability of trace explosive standards in solution”, Poster, A.D. Babore, S.C. Cleary, B. O’Connell, M.R. Richard, L.S. Sowers. Presented at Stockton University, Pomona, NJ (2012)

ABSTRACT OF THE DISSERTATION

Thermal Desorption Studies of Deuterium Oxide on Catalytically-Relevant Metal Oxide Systems

By

Anthony D. Babore

Doctor of Philosophy in Chemistry

University of California, Irvine, 2018

Professor John C. Hemminger, Chair

With the importance and wide applicability of metal oxides in heterogeneous catalysis, understanding these materials on a fundamental level is paramount for the improvement of existing materials and design of new catalysts. Heterogeneous catalytic reactions occur at the interface; therefore, the surface of the material plays a key role in the reactivity. Thus, the work presented herein employs a number of surface sensitive techniques including temperature programmed desorption (TPD), Auger electron spectroscopy (AES), and scanning electron microscopy (SEM) to gain insight into the reactivity of model metal oxide systems of titanium dioxide (TiO_2) and tungsten oxide (WO_{3-x}).

The thermal desorption of deuterium oxide (D_2O) from oxidized tungsten (100), sulfurized tungsten (100), and mixed sulfurized/oxidized tungsten (100) was investigating using TPD. The relative amounts of sulfur and oxygen on each surface was determined using AES. The results show that increasing the amount of sulfur on the tungsten surface weakens the interaction of D_2O within the monolayer. In addition, only the fully sulfurized tungsten (100) resulted in dissociative D_2O adsorption and disproportionation.

Different TiO_2 heterostructures supported on highly oriented pyrolytic graphite were prepared using physical vapor deposition (PVD) and characterized using AES, SEM, and X-ray photoelectron spectroscopy (XPS). TPD using D_2O as a molecular probe reveled that morphological differences in the prepared surfaces lead to pronounced changes in the desorption kinetics.

In addition, a unique systematic TPD investigation was performed on photodeposited platinum nanoparticles supported on TiO_2 nanoparticles supported on HOPG. The results revealed that during the photodeposition process, the platinum adsorbs on the oxygen anion sites of the TiO_2 particles.

Lastly, D_2O thermal desorption was also used to gain insight into the consequences of sample plasma treatments prior to SEM imaging. Argon and oxygen plasma treatments on HOPG were shown to exhibit different D_2O desorption behavior attributed to the oxygen functionality induced by the oxygen plasma. Furthermore, oxygen plasma treated TiO_2/HOPG resulted in a defect site not observed on non-plasma treated TiO_2/HOPG. Moreover, high density TiO_2 nanoparticles prepared via argon and oxygen were compared using TPD and SEM in which no major differences could be elucidated.

CHAPTER 1

Introduction

1.1 Fundamental surface science

Surfaces represent a unique part of solid state materials. A surface serves as a break in the bulk periodicity of a given material and as a consequence, often possesses different structural, electronic, and vibrational properties.[1,2] The surface is usually considered to be ~2-10 atomic layers.[2] Naturally, the outer most region of a material is capable of interacting with its surrounding environment thus, understanding surfaces and interfaces is widely applicable to countless areas of science and industry including: catalysis, electrochemistry, thin films, semiconductors, and alloys.[3] As a result, the field of surface science has been constantly evolving in an effort to understand surfaces at a fundamental level. Over the last 60 years, numerous analytical surface spectroscopy and microscopy techniques have been developed to gain a deeper understanding of surfaces and their interactions, some of which include: Temperature programmed desorption (TPD), Auger electron spectroscopy (AES), X-ray photoelectron spectroscopy (XPS), high-resolution electron energy-loss spectroscopy (HREELS) scanning electron microscopy (SEM), and scanning tunneling microscopy (STM). With a rapidly changing world, there is a persistent need for the development of efficient catalysts, semiconductors, and corrosion resistant materials. With that, surface investigations play an important role in helping to piece together a more complete understanding to better improve such materials.

1.2 Ultra-high vacuum

When performing surface characterizations, it is often necessary to operate under ultra-high vacuum (UHV) conditions. UHV is usually considered to be the vacuum region between $10^{-7} – 10^{-10}$ Pa ($\sim 10^{-9} – 10^{-12}$ torr).[4] Performing analyses within this range minimizes the amount of residual gas in the analysis chamber, which serves two main purposes: to maintain a clean and consistent surface and maximize the mean free path of molecules, photons, electrons, etc. Of course, with constantly advancing technologies, it is now possible to achieve even lower pressures (i.e. extreme high vacuum, $< 10^{-10}$ Pa).

It is noteworthy to mention, that although the use of UHV in surface science is ubiquitous, a disconnect exists between the working conditions of industrial catalysts (high pressures and temperatures) and the conditions of a material in vacuum. This disconnect is known as the "pressure gap".[5] As a result, in recent years a new frontier has emerged to help bridge the "pressure gap" with the introduction of near-ambient pressure surface science techniques such as ambient pressure XPS (APXPS). The use of near-ambient pressures allows for relevant catalyst materials to be analyzed closer to working conditions. In addition, ambient pressure techniques have not only evolved the way sold/vapor interactions are studied but has also facilitated the analysis of liquid/vapor interfaces.[6]

1.3 Heterogeneous catalysis

Due to its applicability to a wide range of scientific genres, heterogeneous catalysis is one of the most intensely investigated areas of research today.[7] Since, heterogeneous catalytic reactions primarily occur at the interface , it is unsurprising that surface science analyses are

crucial to gain insight into the function of these materials. In doing so, surface science plays an integral role in the rational design of new catalysts and improving catalytic reactions.

One of the most interesting classes of heterogeneous catalyst materials are metal oxides. Historically, metal oxides have proved useful for catalyzing a variety of chemical reactions[8,9], though undoubtedly the most prevalent example of a metal oxide heterogeneous catalyst is titanium dioxide (TiO_2). In 1972 Fujishima and Honda reported for the first time the electrolysis of water upon irradiation with ultraviolet (UV) light in a cell containing a TiO_2 photoelectrode and a platinum counter electrode.[10] The result was oxidation of H_2O at the photoelectrode (by photogenerated holes) and reduction of H_2O at the counter electrode (by photogenerated electrons) resulting in the evolution of to O_2 and H_2, respectively.[10,11] In addition, TiO_2 is also readily employed for photo-degradation of organic pollutants, as an anti-bacterial agent, and in paints and protective coatings.[12] Furthermore, TiO_2 has found extensive use as a support for precious metals in metal/oxide model systems.[12] On example being Au or Pt supported on TiO_2 for the oxidation of CO.[13,14]

The photocatalytic properties of semiconducting metal oxides (such as TiO_2) also represent a huge area of developing research. Metal oxides contain a number of desirable properties that lend them useful for photocatalytic applications such as, low cost, reasonable photoactivity, and tunable properties.[15] One major realm of photocatalysis is visible light-driven water splitting. Of course TiO_2 is well known to accomplish water splitting under UV radiation, however its bang gap is too large (~3.0 eV) to absorb in the visible spectrum, which represents the largest part of solar radiation.[16] Thus, for the purpose of photocatalytic water splitting metal oxides with narrower band gaps are more suitable for generating higher photocurrents.[17]

Tungsten trioxide (WO_3) is an example of a semiconducting metal oxide that has been

shown to exhibit advantageous photocatalytic properties. Its relatively narrow band gap (~2.7 eV) is favorable for visible light absorption, however modification of the band structure is ultimately needed to achieve overall water splitting.[18–20] A more detailed discussion of the above is presented in section 3.1.

1.4 Overview of the thesis

The overall goal of this thesis is to shed light onto the reactivity of several relevant oxide catalyst and model catalyst systems. Chapter 2 presents general experimental procedures as well as the theoretical principles of the instrumentation used throughout this work. Chapter 3 shows a simple *in situ* sulfur-doped tungsten oxide system and water desorption experiments to evaluate the fundamental question of the effect of incorporating sulfur into a tungsten oxide material. Chapter 4 explores the effect of varying TiO_2 heterostructure morphology [supported on highly oriented pyrolytic graphite (HOPG)] on water adsorption and reactivity. Chapter 5 presents a unique systematic study in which TPD is used to reveal the active surface sites for platinum nanoparticle adsorption on TiO_2 nanoparticles supported on HOPG after photodeposition. Finally, Chapter 6 uncovers the effect of different plasma treatments (Ar, O_2) on water thermal desorption on HOPG and TiO_2/HOPG samples.

1.5 References

1. Woodruff, D. P. & Delchar, T. A. *Modern Techniques of Surface Science*. (Cambridge University Press, 1994). doi:10.1017/CBO9780511623172
2. Vickerman, J. C. *Surface Analysis– The Principal Techniques*. (John Wiley & Sons, Ltd, 2009). doi:10.1002/9780470721582

3. Chung, Y. W. *Practical guide to surface science and spectroscopy*. *Adsorption Journal Of The International Adsorption Society* **1,** (Elsevier, 2001).

4. Redhead, P. A. Extreme high vacuum. *Cern Eur. Organ. Nucl. Res.* 213–226 (1999).

5. Freund, H.-J. *et al.* Bridging the pressure and materials gaps between catalysis and surface science: clean and modified oxide surfaces. *Top. Catal.* **15,** 201–209 (2001).

6. Trotochaud, L., Head, A. R., Karslıoğlu, O., Kyhl, L. & Bluhm, H. Ambient pressure photoelectron spectroscopy: Practical considerations and experimental frontiers. *J. Phys. Condens. Matter* **29,** 053002 (2017).

7. Somorjai, G. A. The surface science of heterogeneous catalysis. *Surf. Sci.* (1994). doi:10.1016/0039-6028(94)90702-1

8. Védrine, J. Heterogeneous Catalysis on Metal Oxides. *Catalysts* **7,** 341 (2017).

9. Henrich, V. E. and C. P. A. *The Surface Science of Metal Oxides*. (Cambridge University Press, 1994). doi:10.1002/anie.199603471

10. Fujishima, A. & HONDA, K. Electrochemical photolysis of water at a semiconductor electrode. *Nature* **238,** 37–38 (1972).

11. Tentu, R. D. & Basu, S. Photocatalytic water splitting for hydrogen production. *Curr. Opin. Electrochem.* **5,** 56–62 (2017).

12. Diebold, U. The surface science of titanium dioxide. *Surf. Sci. Rep.* **48,** 53–229 (2003).

13. Ando, M., Kobayashi, T. & Haruta, M. Combined effects of small gold particles on the optical gas sensing by transition metal oxide films. *Catal. Today* **36,** 135–141 (1997).

14. Bamwenda, G. R. & Arakawa, H. The visible light induced photocatalytic activity of tungsten trioxide powders. *Appl. Catal. A Gen.* **210,** 181–191 (2001).

15. Chan, S. H. S., Yeong Wu, T., Juan, J. C. & Teh, C. Y. Recent developments of metal

oxide semiconductors as photocatalysts in advanced oxidation processes (AOPs) for treatment of dye waste-water. *J. Chem. Technol. Biotechnol.* **86,** 1130–1158 (2011).

16. Ahmad, H., Kamarudin, S. K., Minggu, L. J. & Kassim, M. Hydrogen from photo-catalytic water splitting process: A review. *Renew. Sustain. Energy Rev.* **43,** 599–610 (2015).

17. Li, W., Li, J., Wang, X. & Chen, Q. Preparation and water-splitting photocatalytic behavior of S-doped WO3. *Appl. Surf. Sci.* **263,** 157–162 (2012).

18. Butler, M. A., Nasby, R. D. & Quinn, R. K. Tungsten trioxide as an electrode for photoelectrolysis of water. *Solid State Commun.* **19,** 1011–1014 (1976).

19. Wang, F., Di Valentin, C. & Pacchioni, G. Doping of WO 3 for Photocatalytic Water Splitting: Hints from Density Functional Theory. *J. Phys. Chem. C* **116,** 8901–8909 (2012).

20. Di Valentin, C., Wang, F. & Pacchioni, G. Tungsten Oxide in Catalysis and Photocatalysis: Hints from DFT. *Top. Catal.* **56,** 1404–1419 (2013).

CHAPTER 2

Instrumentation and Experimental Techniques

2.1 Temperature programmed desorption chamber

All experiments were performed in a custom built, stainless steel (SS), ultra-high vacuum (UHV) chamber. The SS construction and quartz windows allow the chamber to be "baked" at temperatures of ~150 ºC to remove water and hydrocarbon adsorbed on chamber walls, in turn lowering the base pressure and providing a clean environment for experiments. A mass spectrum showing the chamber background before and after bake-out is shown in Figure 2.1 below, highlighting the decrease in the amount of water (m/z 18).

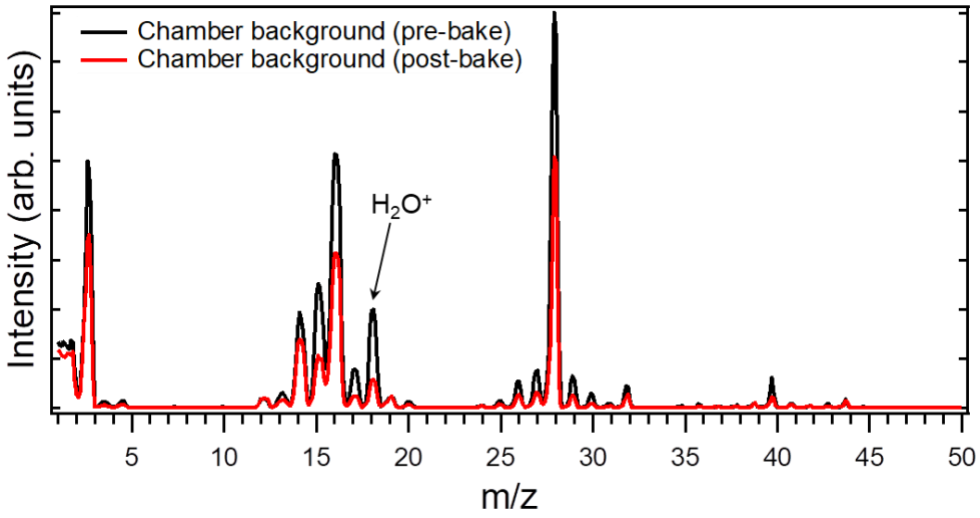

Figure 2.1. Typical chamber background mass spectrum before and after baking the chamber

The chamber's primary function is to perform temperature programmed desorption (TPD) experiments and prepare and characterize samples. These tasks are accomplished using a UTI 100C mass spectrometer (MS) to monitor desorption, a Perkin-Elmer 10-155 Auger electron

spectrometer for surface characterization, an ion gun powered by a Varian 981-2046 power supply for Ar^+ sputtering and multiple gas dosers to aid in sample cleaning and preparation. A detailed description of fundamentals of TPD and Auger electron spectroscopy (AES) will be discussed in section 2.3 and 2.4, respectively.

A schematic of the TPD chamber is shown in Figure 2.2 below.

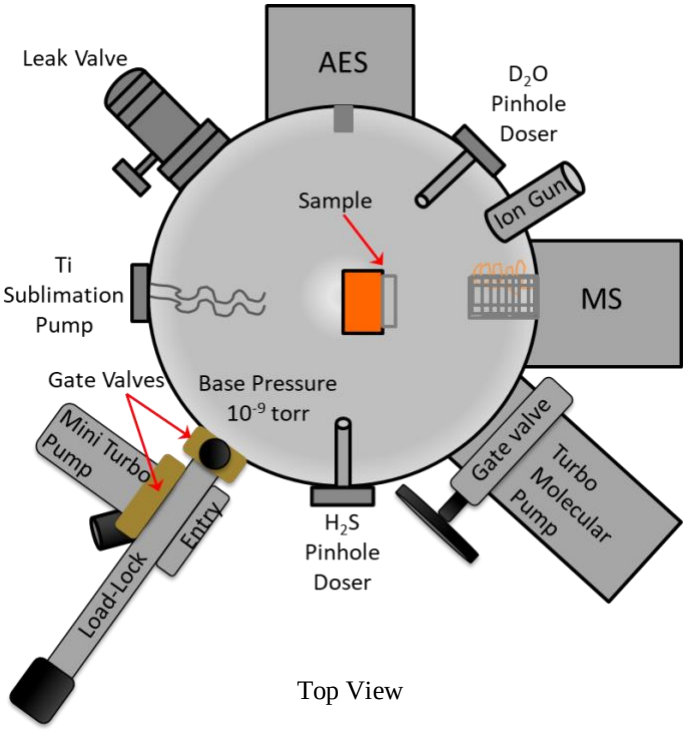

Figure 2.2. TPD chamber schematic.

The chamber base pressure (~1×10^{-9} torr) is maintained using a turbo molecular pump (Leybold TMP 361). A lower base pressure, needed for thermal desorption experiments (1×10^{-10} torr), is attained using a titanium sublimation pump (TSP). The chamber is also equipped with a fast loadlock entry pumped by a Balzer-Pfeiffer TPU 060 turbo molecular pump connected to

the chamber by a gate valve. This allows for samples to be quickly inserted and removed without venting the chamber. Various gases including D_2O, H_2O, H_2S and CO can be introduced into the chamber via two directional dosers, each fitted with a 1μm pinhole gasket to allow for controlled effusion of the gasses into the chamber by differential pumping. Additionally, the chamber is fitted with a standard leak valve primarily used for backfilling O_2 and Ar into the chamber.

2.2 Sample holder

The sample holder is mounted on a rotatable X,Y,Z manipulator and is electrically connected by copper feedthroughs connected to a GW-Instek PSM-2010 programmable power supply. The manipulator is also equipped with liquid nitrogen (LN_2) feedthroughs with SS flexible bellows welded to a copper reservoir to allow for conductive cooling of the sample. The different sample holder configurations for mounting highly oriented pyrolytic graphite (HOPG) substrates and single crystal samples are shown in Figure 2.3a and 2.3b, respectively. The opposing copper blocks of the sample holder are electrically isolated by a Macor block such that the sample bridges the electrical circuit thus enabling resistive heating. The sample holder sits on SS tracks on the manipulator putting it in direct thermal contact with the liquid nitrogen reservoir as well as completing the resistive heating circuit. The SS flaps of Figure 2.3 create a firm contact between the sample holder and the tracks on the manipulator. Poor contact with the tracks results in steps in the linear heating profile and insufficient cooling. In addition, the thermocouple (TC) ears fit into SS clips that relay the sample temperature through a UHV feedthrough to a LabView temperature monitoring program. For HOPG substrates, the TC junction is sandwiched between the HOPG substrate and an HOPG backing. The substrate and backing HOPG are held firmly together by molybdenum screws that fasten the SS clips to the

tantalum backing plates, creating a good contact between the sample and tungsten heating wires. For single crystal samples the TC is spot-welded directly on the edge of the crystal and the tungsten heating wires are tightly fit into a groove on the edge of the crystal. If a single crystal lacks a groove, then platinum wire can be spot-welded to the crystal as tungsten is brittle and difficult to spot-weld.

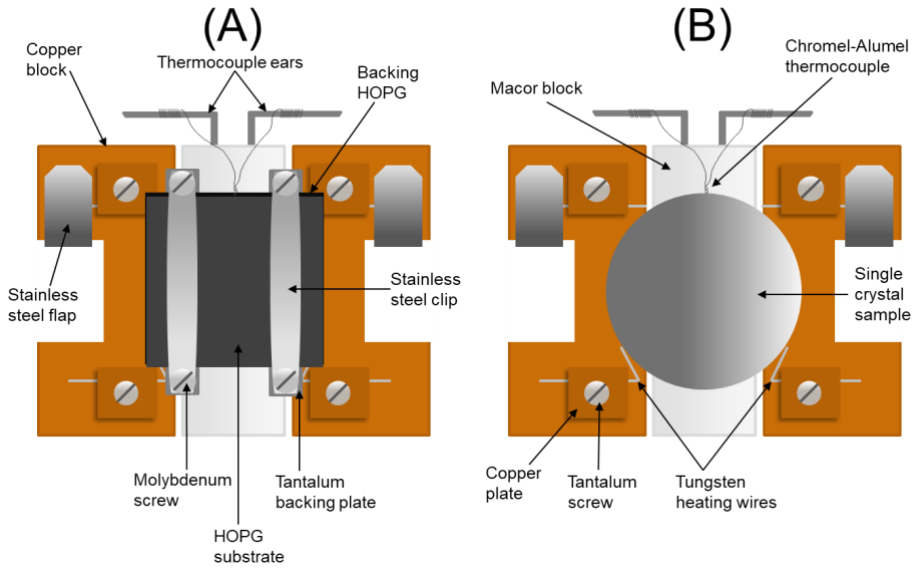

Figure 2.3. Sample holder schematic for the (a) HOPG substrate configuration and (b) single crystal configuration.

2.3 Temperature programmed desorption

2.3.1 *Overview*

Temperature Programmed Desorption (TPD), also referred to as thermal desorption spectroscopy (TDS), is an analytical technique used to probe the reactivity a gas adsorbed on a surface. A typical TPD experiment consists of exposing the surface to the probe molecule at low temperature (<130 K, or in some instances room temperature) and applying a linear temperature

ramp while simultaneously monitoring the mass to charge ratio (m/z) of the desorbing species with a mass spectrometer. The heating rate is described by the following equation:[1–3]

$$T = T_o + \beta t \tag{1}$$

where T is the temperature (K), T_o is the initial temperature (K), t is the time (s) and β is the heating rate (K/s) defined as:[1–3]

$$\beta = \frac{dT}{dt} \tag{2}$$

Accurate TPD measurements and extraction of kinetic parameters rely heavily on the linearity of the heating schedule.

By varying the exposure of the adsorbate, one can generate a TPD spectrum comprised of multiple traces in which the m/z intensity is plotted versus temperature (K). An example TPD spectrum of D_2O on HOPG is shown in Figure 2.4, where the m/z 20 intensity is plotted as a function of the temperature for exposures ranging from $4.2 \times 10^{12} - 5.1 \times 10^{14}$ molec/cm^2. In doing so, kinetic information such as the activation energy of desorption, desorption order, frequency factor as well as surface information such as specific adsorption sites, reactions, and surface coverage can be determined.

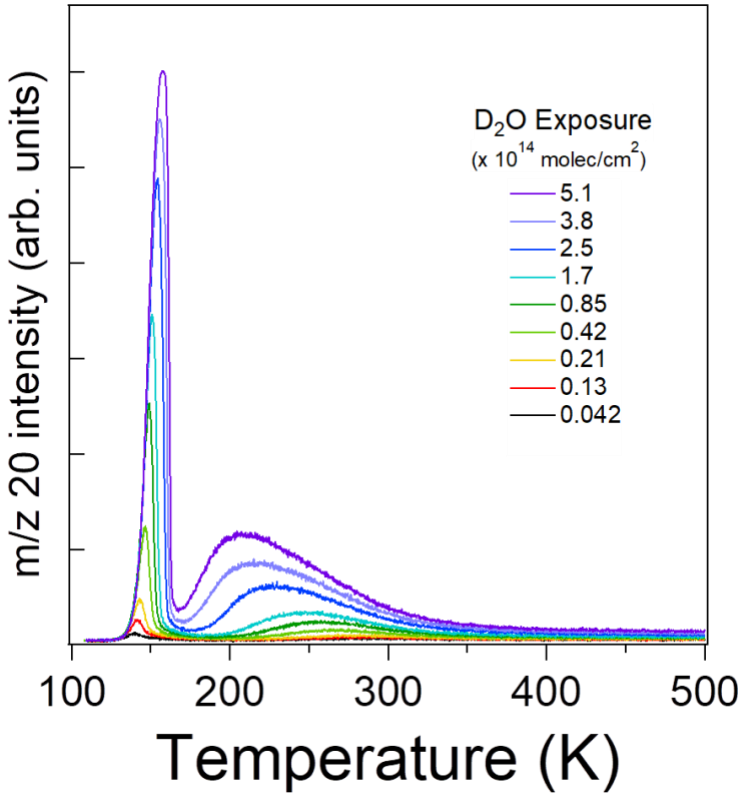

Figure 2.4. Example TPD spectrum: D_2O desorption from freshly cleaved HOPG.

2.3.2 *Desorption kinetics*

In a TPD experiment, several (valid) assumptions are made regarding both, the introduction of the probe gas into the chamber as well as desorption cycle; the first of which is that adsorption of gas onto the chamber walls considered to be negligible.[1] In this work, this assumption is especially valid since a pin-hole doser is employed instead of the more traditional backfilling method. Furthermore, it can be assumed that readsorption of the probe gas onto the sample surface is negligible at high pumping speeds and rapid desorption cycles.[1] In making these assumptions, one finds that the partial pressure of the desorbing gas is then proportional to the desorption rate ($-d\theta/dt$) such that the rate of desorption (r) can be written as:

$$r = -\frac{d\theta}{dt} = k\theta^n \tag{3}$$

where θ is the fractional surface coverage and n is the desorption order.[1–3]

Adsorption of a molecule on the surface can occur via three different pathways: Physisorption, chemisorption and dissociative chemisorption. For a physisorbed molecule, there are no major changes to the electronic structure of the molecule and the molecule is only bound to the surface by weak forces (i.e. Van der Waals forces). Chemisorption, is a process in which the molecule is chemically bound to the surface. Similarly, dissociative adsorption occurs when the molecule reacts on the surface and separates into two or more components bound to the surface (i.e. dissociation).[4] Figure 2.5 shows the potential energy curves for a physisorbed molecule (AB) and the reaction of A+B on the surface (S).[5]

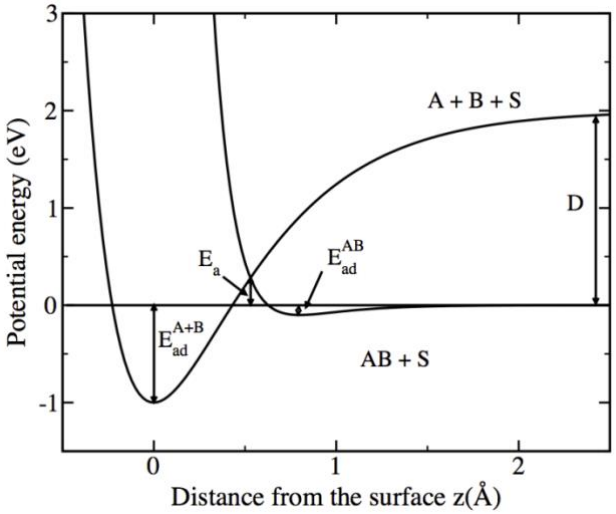

Figure 2.5. Potential energy diagram for a physisorption molecule (AB) and reaction of atoms A and B on a surface (S). Figure borrowed with permission from Ref. [5] (Copyright © 2009 Springer Nature).

For the physisorbed molecule AB, there is a small potential energy well with an adsorption energy of E_{ad}^{AB}, whereas the reaction of atom A and B has a deeper well with a greater adsorption energy of $E_{ad}^{A+B} + D$. In this case, the overlap of the two potential energy curves gives rise to a dissociation barrier E_a, such that if molecule AB is adsorbed on the surface, it may dissociate provided there is enough energy to overcome E_a. If E_a is less than 0 eV than AB will spontaneously dissociate upon adsorption. As a result, in order for an adsorbed molecule to desorb from the surface, it must also overcome an energy barrier. Thus, the desorption rate constant *k* is described by the Arrhenius equation:

$$k = v \exp\left(\frac{-E_{des}}{RT}\right) \tag{4}$$

where *v* is the frequency factor (sec^{-1}), E_{des} is the activation energy of desorption (J/mol), *R* is the ideal gas constant (J/mol·K) and *T* is the substrate temperature (K).[1–3] In substituting Equation 4 into Equation 3, one obtains the Polanyi-Wigner equation that of which fully describes the desorption process:[1–3]

$$-\frac{d\theta}{dt} = v\theta^n \exp\left(\frac{-E_{des}}{RT}\right) \tag{5}$$

By substitution of Equation 2 into Equation 5, the Polanyi-Wigner equation can be rewritten in terms of temperature yielding:

$$-\frac{d\theta}{dT} = \frac{v\theta^n}{\beta}\exp\left(\frac{-E_{des}}{RT}\right) \quad (6)$$

From the temperature dependent Polanyi-Wigner equation (Equation 6), kinetic simulations of TPD data can be obtained. Figure 2.6 shows simulated TPD spectra for (a) first order, (b) second order and (c) zero order cases.[6] The kinetic parameters used to generate the TPD data of Figure 2.6 are shown on the respective spectra.

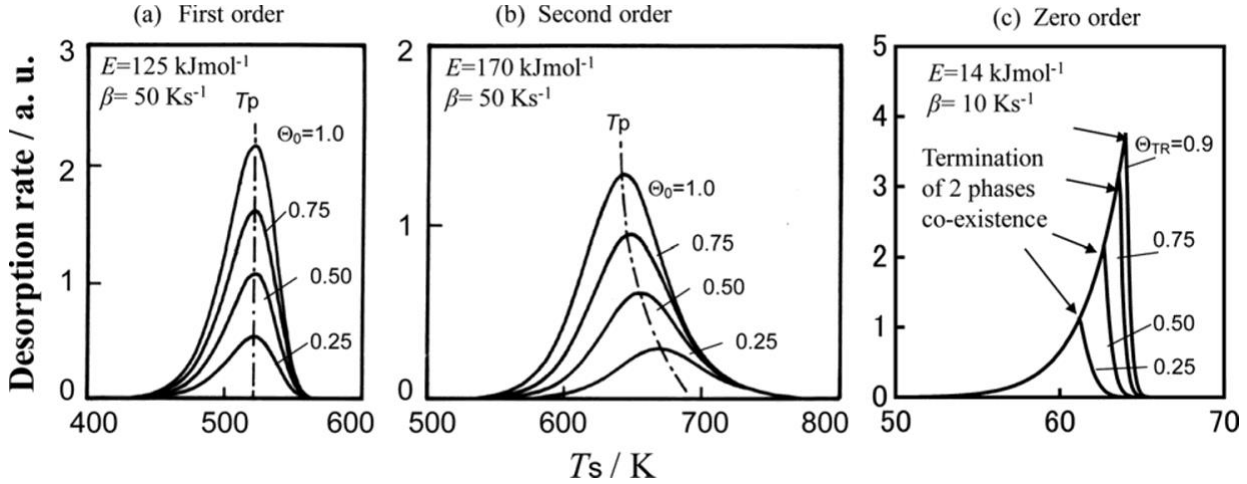

Figure 2.6. Kinetic simulations of TPD spectra for (a) first order, (b) second order and (c) zero order desorption kinetics using the Polanyi-Wigner equation. Figure borrowed with permission from Ref.[6] (Copyright © 2018 Elsevier Inc.).

In looking at Equation 6, the exponential term of the Polanyi-Wigner equation gives the initial rise in the desorption peak until the decreasing coverage term ($v\theta^n/\beta$) dominates the exponential term and depletes the desorption rate.[6] The above simulations are idealized cases of desorption; In reality, many factors come into play that affect the peak shape and position such as surface defects, lateral interactions between adsorbed molecules and surface heterogeneity. As a result, a complete understanding of the desorption kinetic parameters is difficult to obtain.

2.3.3 *Redhead analysis*

Undoubtedly, the most influential and widely used method for analyzing TPD data was first described by P.A. Redhead in 1962.[1] The Redhead method uses the desorption peak temperature as a way to estimate the activation energy of desorption (E_{des}). At the peak temperature maximum (T_p) the second derivative of Equation (6) ($-d^2\theta/dT^2$) is zero leading to the following expression:

$$\frac{E}{RT_P^2} = \frac{v}{\beta} n\theta^{n-1} \exp\left(\frac{-E}{RT_P}\right) \tag{7}$$

For a first order process, it becomes clear that desorption is independent of the coverage (θ) and the expression can be written as:

$$\frac{E}{RT_P^2} = \frac{v}{\beta} \exp\left(\frac{-E}{RT_P}\right) \tag{8}$$

In order to compute the energy using Equation 8 a value of v must be assumed, often 1×10^{13} sec^{-1}. Furthermore, Redhead states that the linear relationship between E_{des} and T_P yields a 1.5% error in the selection of the v provided the value is between 1×10^8 and 1×10^{13} sec^{-1} thus Equation 8 can be refined further to:[1,3,7]

$$\frac{E}{RT_P} = \ln\frac{T_P v}{\beta} - 3.64 \tag{9}$$

It is important to note that for first order desorption the desorption peak temperature does not vary with coverage in ideal cases. However, this is not often the case as the activation energy of desorption may be coverage dependent. A discussion of a method for evaluating the coverage dependent energy will be discussed in the section 2.3.6.

2.3.4 *Leading edge analysis*

The leading edge analysis is most widely applied to calculating E_{des} for spectra that follow zeroth order desorption behavior.[8] To do so, the linearized form of Polanyi-Wigner equation is evaluated for n=0 giving:

$$\ln\left(-\frac{d\theta}{dT}\right) = \frac{-E_{des}}{R}\left(\frac{1}{T}\right) + \ln\left(\frac{v}{\beta}\right) \tag{10}$$

The leading edge analysis utilizes the leading edge, or initial onset, of the desorption peak. Figure 2.7 shows an example of the application of the leading edge analysis for D_2O multilayer desorption from HOPG. At the initial onset of the multilayer (boxed in red) the desorption rate can be considered constant. By constructing an Arrhenius plot using Equation 10 (shown in the inset of Figure 2.7) and fitting a line to the small area of the leading edge, the slope of the line (-*E/R*) is used to calculate E_{des} and the y-intercept gives the frequency factor, *v*.[8,9] It is important to note that this method requires high quality TPD data as the slope of the line of the Arrhenius plot is susceptible to slight changes in the initial onset region.

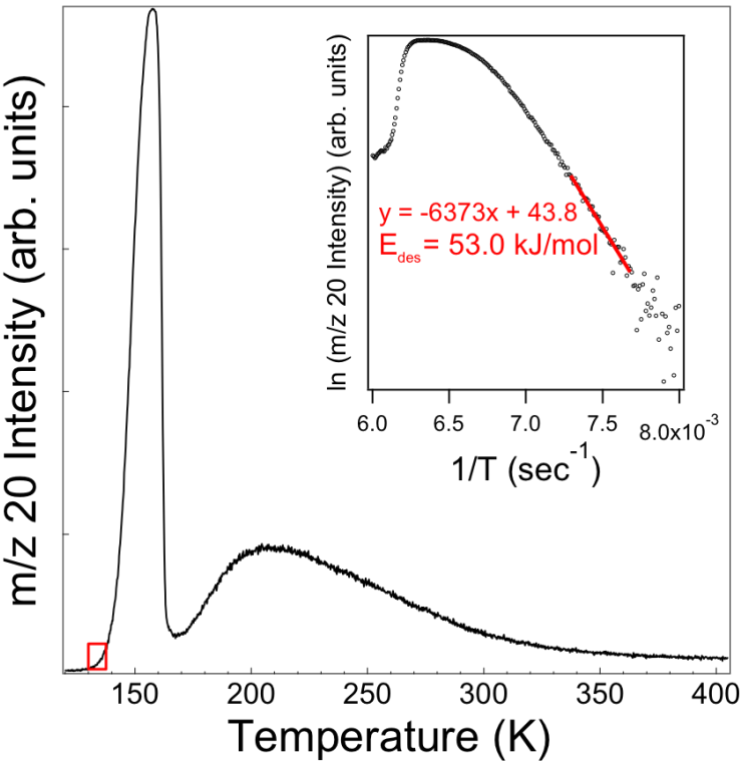

Figure 2.7. TPD spectrum of D_2O on HOPG demonstrating the leading edge analysis. The red box indicates the leading edge region. The inset shows the Arrhenius plot generated using Equation 10 for the leading edge and the calculated activation energy for desorption (E_{des}).

2.3.5 *Heating rate variation*

Another method for evaluating TPD spectra is known as the heating rate variation method. This method is done by obtaining multiple TPD traces of the same initial coverage but varying heating rates (β). In doing so a plot of $ln(\beta/T^2)$ vs. $1/T$ can be constructed with a slope equal to $-E/R$. The advantage of this method is that the value of the frequency factor does not need to be known however, the heating rate needs to be varied by orders of magnitude.[2,9]

2.3.6 *Coverage-dependent energy*

Bruce Kay and coworkers first described a method for calculating the activation energy of desorption as a function of the surface coverage of the adsorbed species, known as the inversion method.[10] This method employs a mathematically inverted form of the Polanyi-Wigner equation in which the coverage-dependent activation energy of desorption $E_{des}(\theta)$ is given by:

$$E_{des}(\theta) = -R\,T\,\ln\left[\frac{-d\theta/dt}{\nu\theta}\right] \tag{11}$$

where ν is assumed to be independent of the coverage and temperature. The coverage (θ), also referred to as the instantaneous coverage (i.e. the fractional coverage at a given temperature) is determined by integrating the desorption spectrum from right to left. In doing so a plot of $E_{des}(\theta)$ vs. θ can be constructed.[10] An example plot for a 0.05 ML initial coverage of D_2O on oxidized W (100) is shown in Figure 2.8 below. The inset of Figure 2.8 shows the corresponding desorption spectrum used in the calculation of $E_{des}(\theta)$ and the location of the peak temperature is indicated on the energy curve. Truly coverage-independent desorption kinetics would result in a discrete energy value given by a horizontal line; however, it can be seen that in the present case the energy varies with coverage.

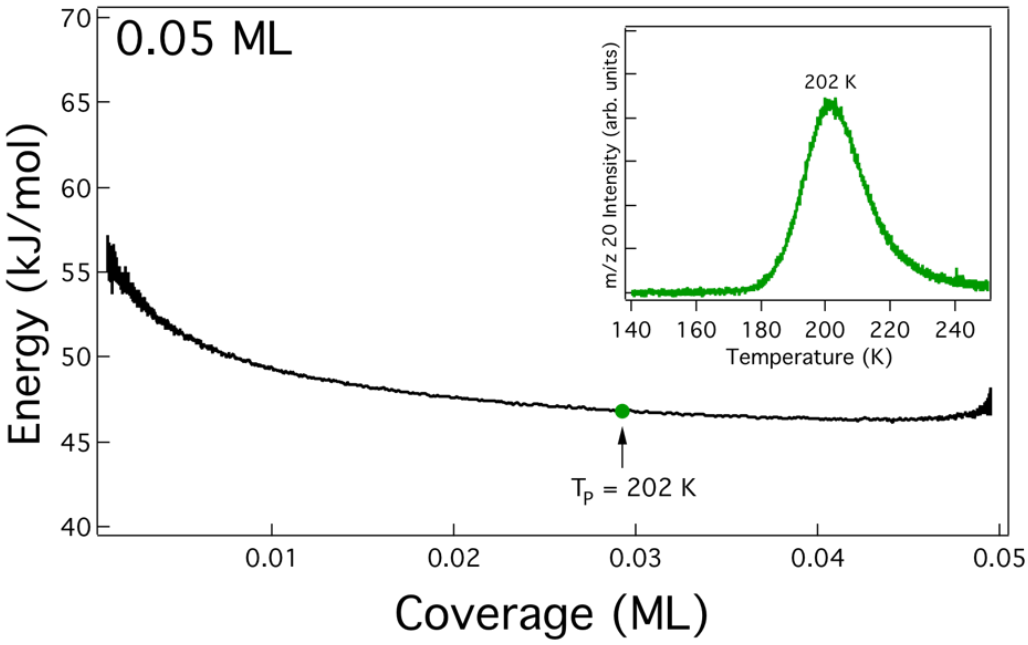

Figure 2.8. Example plot for the coverage-dependent activation energy of desorption $E_{des}(\theta)$ as a function of the coverage θ determined using the inversion method described by Kay et al.[10] for 0.05 ML initial coverage of D_2O on oxidized W (100). The inset shows the corresponding desorption spectrum. The peak temperature T_P (202 K) is indicated by the green marker on the energy curve.

The above sections highlight only a few of the methods available for evaluating desorption kinetics of TPD spectra. For a broader overview of additional techniques, the author referrers the reader to Ref.[9] in which multiple analysis methods are presented, assessed and compared.

2.3.7 *Isotope analysis*

Using D_2O as the probe gas can be exploited to obtain information about isotope exchange interactions on the surface. To do so, the total area of each individual TPD trace for m/z 18, 19 and 20 is obtained, where m/z 18 corresponds to OD^+ and H_2O^+, m/z 19 is to HOD^+ and m/z 20 is D_2O. Since HOD^+ can only result if an H-D exchange interaction has occurred, the

%HOD^+ can be used to obtain a semi-quantitative view of surface hydroxyl species present on the surface. The %HOD^+ is obtained from the following equation:

$$\%HOD^+ = \frac{area\ (m/z19)}{\sum area\ (m/z\ 18), area\ (m/z\ 19), area\ (m/z\ 20)} \times 100 \qquad (12)$$

It is to be noted, the semi-quantitative nature of this analysis arises due to exchange interactions that may occur with D_2O and H_2O in the gas manifold prior to exposures.

2.4 Auger electron spectroscopy

2.4.1 *Overview*

Auger electron spectroscopy (AES) is a non-destructive surface-sensitive technique used to determine the elemental composition of a sample.[11,12] AES makes use of the Auger effect (see section 2.42) in which Auger electrons are emitted from a sample after bombardment with electrons (or in some cases photons).[13,14] The kinetic energy of the ejected Auger electrons is analyzed using a cylindrical mirror analyzer (CMA) in which a DC sweep is applied to scan the Auger electron energies. This is then followed by signal amplification via an electron multiplier. Furthermore, a lock-in amplifier is then used to modulate the AC Auger electron signal and phase out AC noise. A schematic of a typical Auger electron spectrometer schematic is shown in Figure 2.9 below.

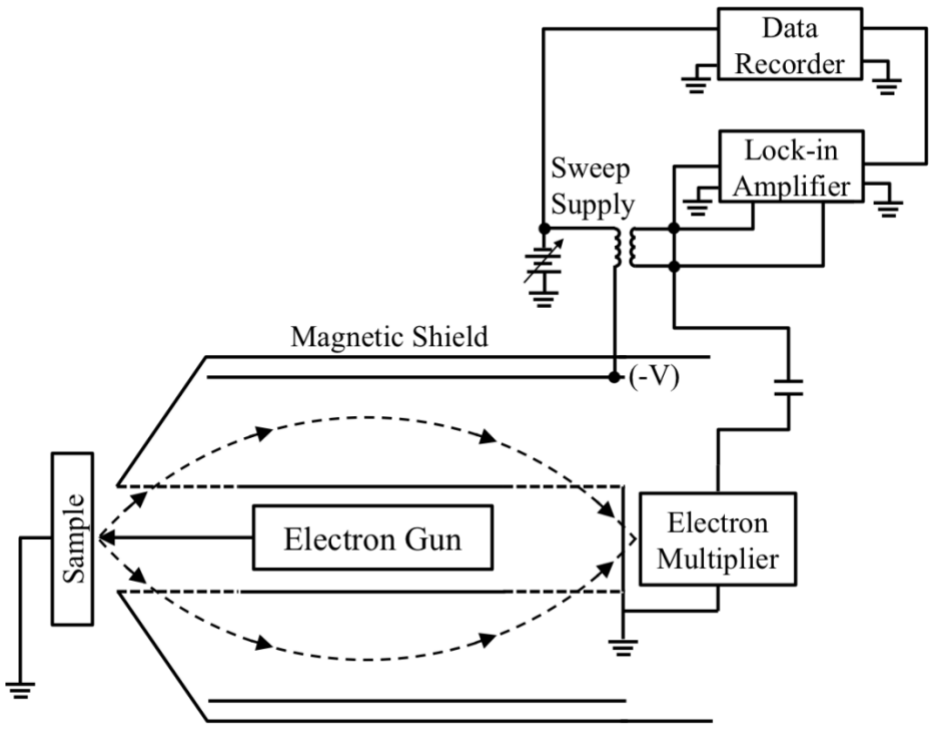

Figure 2.9. Schematic of a typical Auger electron spectrometer.

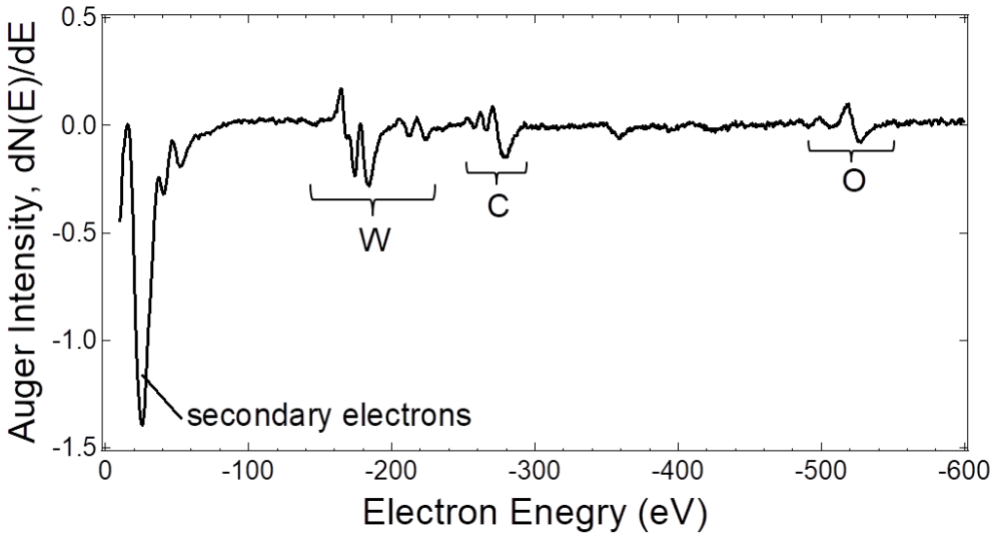

Figure 2.10. Example AES spectrum for a "dirty" W (100) sample

A raw Auger spectrum consists of the signal N(E) plotted as a function of the kinetic energy (eV). However, the derivative of the Auger signal *d(E)N/dE* is more often used as high energy backscattered electrons overshadow the Auger electrons. An example Auger spectrum is shown in Figure 2.10 highlighting some of the major elemental peaks for a "dirty" tungsten single crystal. Auger electrons resulting from a given element have a completely unique energy, thus AES is an extremely effective and sensitive technique for determining the composition of a surface. Its surface sensitivity arises as a result of the relatively low energy of the Auger electrons emitted that are capable of escaping from only the first few monolayers (3-20 Å) of the substrate.[15,16]

2.4.2 *Principles of AES*

The Auger process proceeds via a two-step process, given by the following:

$$A + e_i^- \rightarrow A^{+*} + e_i^{-\prime} + e_A^- \tag{13}$$

where an atom *A* is excited to A^+* by the electron beam e_i^-. Relaxation of A^+* results in the emission of an Auger electron e_A^- as well as the incident electron beam, post interaction with the atom. The relaxation process proceeds via:

$$A^{+*} \rightarrow A^{++} + e_A^- \tag{14}$$

where A^+* relaxes to a new state A^{++} such that a transfer in energy leads to the ejection of an Auger electron e_A^-.[15,17] An alternative and competitive relaxation process may also occur where:

$$A^{+*} \rightarrow A^{+} + h\nu_f \tag{15}$$

In this process, the excited atom A^{+*} relaxes back down to its original energy level and a photon $h\nu_f$ is given off, known as X-ray fluorescence.[15,17] The processes of Auger electron and X-ray ejection are illustrated in Figure 2.11 below.[12]

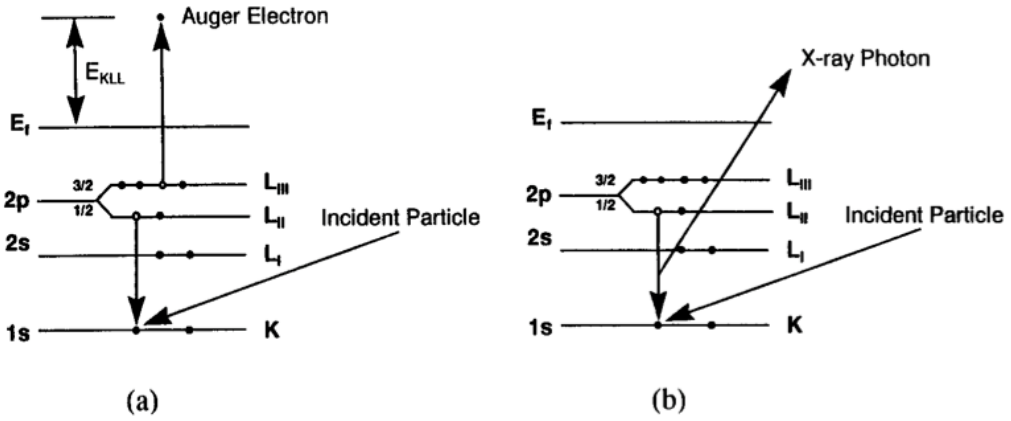

Figure 2.11. (a) Auger electron emission and (b) X-Ray photon emission processes. Figure borrowed with permission from Ref.[12] (Copyright © 2004 Taylor & Francis publishing).

The kinetic energy *E* of the ejected Auger electron can be represented by the following:

$$E = E_K - E_{L(II)} - E_{L(III)} \tag{16}$$

where E_K is energy of the core electron shell, $E_{L(II)}$ is the initial energy level of the relaxed electron and $E_{L(III)}$ is the initial energy level of the auger electron that is ejected.[15,17]

As previously mentioned, auger electron emission and X-ray fluorescence are competitive processes. It has been reported that for elements of lower atomic weight, the auger process is favored. Conversely, for heavier elements x-ray fluorescence is favored.[15,17] Whether process (a) or (b) occurs (from Figure 2.11) is dependent on if the energy of the electron beam exceeds the energy of the x-ray absorption edge of the core shell energy level.[13]

2.4.3 *Quantitative analysis of AES spectra*

Though AES is primarily a qualitative technique, quantitative information can be extracted with careful evaluation of the Auger spectra. This section will discuss two quantitative methods: determination of atomic concentrations of a sample and film thickness. To determine the atomic concentration using AES, relative sensitivity factors (RSFs) must be used for direct comparison of peaks in the Auger spectrum. Relative sensitivity factors $S_X(E_p)$ as a function of the primary beam energy E_p for a given element X can be calculated using the following equation:

$$S_X(E_p) = \left(\frac{A+B}{A}\right)\left(\frac{I_X}{K_X I_{Ag}}\right) \tag{17}$$

where A and B are obtained from the chemical formula of compound of interest (X_AY_B), K_X is a scaling factor and I_X and I_{Ag} are the peak-to-peak intensities, of the element X and a Ag standard, respectively.[18] The *Handbook of Auger Electron Spectroscopy*[18] lists RSF values calculated using Equation 16 for primary beam energies of 3 keV, 5 keV and 10 keV. However, the RSF values reported neglect to account for the derivative peak shapes resulting from Auger spectra collected in the *dN(E)/dE* mode. As a result, Susan Mroczkowski and David Lichtman reported

calculated RSF values normalized to the RSF values of the *Handbook of Auger Electron Spectroscopy* that take into account the *dN(E)/dE* peak shape.[19] In their calculation, the authors included ionization cross sections, atomic densities, electron escape depths, back scattering factors and transition probabilities.[19] Thus, RSF values for quantification used in this work were obtained from Mroczkowski and Lichtman.[19]

To determine atomic concentrations of a sample C_X the following equation is used:

$$C_X = \left(\frac{I_X}{S_X d_X}\right) \Big/ \left[\sum_\alpha \left(\frac{I_\alpha}{S_\alpha d_\alpha}\right)\right] \tag{18}$$

in which the peak-to-peak intensity of element X is ratioed to the sum of one peak-to-peak intensity per element I_α of the sample with their respective RSF values S_α. Furthermore, d_x and d_α are scaling factors that are a function of the sensitivity of the lock-in amplifier, modulation energy and primary beam current.[18]

Auger electron spectroscopy can also be used to determine the thickness of a thin film/overlayer via analysis of peak-to-peak intensities as described by P.H. Holloway.[20] The principle used is that the signal intensity of a substrate I_s decays exponentially as an overlayer of thickness x accumulates on the surface according to:

$$I_s = I_{0s} \exp(-x/\mu_s) \tag{19}$$

where I_{0s} is the signal intensity of a clean substrate and μ_s is the mean free path of Auger electrons from the substrate in the overlayer.[20]

2.5 Experimental procedures and sample preparation

2.5.1 *Sample preparation*

The nature of this work mainly involves two types of samples, those that utilize highly oriented pyrolytic graphite (HOPG) as the substrate, or single crystal samples namely, tungsten (100) and platinum (111). All sample preparation for HOPG substrates was performed *ex situ* whereas all single crystal samples were prepared *in situ*. The section herein will provide a general description of the sample preparation procedures, specific sample preparation procedures will be discussed in their respective sections.

In this work HOPG was used as a support for titanium dioxide (TiO_2) heterostructures, including thin films, dendritic structures and nanoparticles. For any given sample, a piece of HOPG (ZYB grade, Momentive Performance) was first freshly cleaved using the Scotch tape method.[21] HOPG substrates were then mounted in a bell jar vacuum chamber pumped down pressures on the order of 10^{-6} torr. Physical vapor deposition (PVD) was then used to evaporate titanium onto the surface at elevated temperatures (accomplished by resistive heating). Given that the pressure in the bell jar is in the high vacuum range, there is inherently residual water in the background that fully oxidizes the Ti to stoichiometric TiO_2 [determined by X-ray photoelectron spectroscopy (XPS)].

Depending on the substrate temperature used, different TiO_2 morphologies are grown on the surface of the HOPG.[22] At lower temperatures (~300 ºC) a TiO_2 thin film results on the surface. HOPG is an inert surface that contains step edges with long terraces, thus at elevated temperatures (~800 ºC) titanium adatoms on the surface are provided with substantial thermal energy such that they may move around on the surface, agglomerate and nucleate into particles at step edges, as shown in previous work.[22] Furthermore, pretreatment of the HOPG with oxygen or

argon plasma, generates defect sites distributed across the surface which promote the formation of a dense distribution TiO_2 nanoparticles on the HOPG surface.

For single crystals, the substrate is first mounted in the sample holder configuration shown in Figure 2.3b and introduced into the TPD chamber for surface preparation. To obtain a clean crystal sample, Ar^+ sputtering is performed using a beam energy, typically, between 0.5 and 2 keV to remove adventitious carbon and oxygen adsorbed on the surface, monitored using AES. For platinum single crystal samples, annealing in oxygen (> 800 K) was employed to further remove adventitious carbon as well as reorganize the surface (i.e. removed surface defects generated by Ar^+ bombardment). Note: Tungsten samples were unable to be cleaned using oxygen annealing as a much higher temperature is required (> 1300 K) that is beyond the resistive heating capabilities of the TPD instrument.

Oxide films on the W (100) surface were prepared by exposing the clean W (100) crystal to O_2 (research grade, AirGas) backfilled into the chamber via a leak valve at 800 K. AES was again used to monitor surface carbon species and saturated oxide growth. Sulfur films were generated by exposing the clean W (100) crystal to H_2S (5% balance N_2, CalGas) at room temperature via a 1 μm pinhole doser. Saturation coverages and surface species were again determined using AES. Furthermore, mixed oxide-sulfide films were generally prepared by exposing the clean tungsten surface to a sub-saturation amount of H_2S at room temperature followed by exposure to O_2 at 800 K.

2.5.2 *TPD experimental*

Prior to performing TPD experiments, the TSP is flashed for ~2 min to lower the base pressure to ~1×10^{-10} torr. The gas manifold and dosing line is then passivated with the probe gas

and pumped out 3-4 times. Majority of the experiments performed in this work utilize D_2O as the probe gas (Aldrich, 99.96% D) purified by freeze-pump-thaw cycles. It should be mentioned that D_2O is used as opposed to H_2O to account for a relatively high presence of H_2O in the chamber background. In addition, using D_2O also allows for monitoring isotope exchange interactions on the surface of interest, as discussed in section 2.3.7. After passivation of the dosing lines, a mass spectrum is acquired to ensure the D_2O is pure. The sample is cooled to 100-130 K by flowing liquid nitrogen through the LN_2 feedthroughs into a copper reservoir in direct contact with the sample holder, as previously mentioned. Before dosing the sample, at least one blank TPD ramp is done to remove any adsorbed species from the surface. Dosing of the sample is then done by again cooling, rotating the sample directly in front of the doser for a designated time (at pressure of 1 torr behind the pinhole, typically) followed by rotating the sample in front of the MS filament and initiating the TPD ramp (typically 2 K/s to ~700 K). Data is acquired using a LabView program in which the MS signal of a specified m/z ratio is monitored as a function of the temperature. A full TPD spectrum is compiled by obtaining multiple doses of varying exposure time.

2.5.3 *Exposure/coverage determination*

Traditional TPD experiments employ a leak valve to backfill the chamber with gas where the exposure is measured in units of Langmuirs (L). By definition, 1 Langmuir is 1×10^6 torr at 1 sec. For example, exposing a sample to a partial pressure of 5×10^8 torr for 120 sec would yield and exposure of 5.0 L. As previously mentioned, the present work primarily uses a pin-hole doser to expose the sample to a probe gas. In order to determine the exposure for a gas being leaked through the 1μm pin-hole orifice, the effusion rate of the gas must be calculated. This is

accomplished by first considering the collisional rate of the gas molecules with the aperture given by:

$$\frac{dN_c}{dt} = \tilde{N} A \frac{1}{4} v_{avg} \tag{20}$$

where, dN_c/dt is the collisional rate, $\tilde{N}$ is particle density, A is the area of the orifice being struck and v_{avg} average speed of the particles (m/sec).[23] If Equation 16 is divided by the area, the resulting is the collisional flux Z_c or the number of collisions as a function of time and area (m^{-2} sec^{-1}):

$$Z_c = \frac{dN_c/dt}{A} = \tilde{N} \frac{1}{4} v_{avg} \tag{21}$$

The average speed can be derived from the Maxwell speed distribution giving:

$$v_{avg} = \left(\frac{8RT}{\pi M}\right)^{1/2} \tag{22}$$

where R is the ideal gas constant, T is the temperature (K) and M is the molar mass (kg/mol).[23] For the present case, the particle density can be more appropriately written in terms of pressure by using the Ideal Gas Law such that:

$$\tilde{N} = \frac{n}{V} = \frac{PN_A}{RT} \tag{23}$$

where P is the pressure (Pa), n is the number of moles, N_A is Avogadro's number, and V is the volume (m^3).[23] Finally, substituting Equation 18 and 19 into Equation 17 yields:[23]

$$Z_c = \frac{PN_A}{(2\pi MRT)^{1/2}} \tag{24}$$

To determine the exposure of a given probe molecule during a TPD experiment, the pressure of gas behind the orifice (typically 1 torr) is first monitored using an MKS Baratron Model 622A. The molar mass (M) of D_2O (0.020 kg/mol) is then used to calculate Z_c. Once Z_c is obtained, it is then multiplied by the area of the orifice (πr^2) to obtain the effusion rate (sec^{-1}) of gas into the chamber. Additionally, simply multiplying the effusion rate by the exposure time and dividing by the area of the surface results in an exposure in units of molecules/cm^2. Furthermore, fractional coverage values (in monolayers, ML) can be obtained by evaluation of the TPD spectrum, provided monolayer saturation is observed.

2.6 References

1. Redhead, P. P. a. Thermal desorption of gases. *Vacuum* **12,** 203–211 (1962).
2. Barrie, P. J. Analysis of temperature programmed desorption (TPD) data for the characterisation of catalysts containing a distribution of adsorption sites. *Phys. Chem. Chem. Phys.* **10,** 1688 (2008).
3. King, D. A. Thermal desorption from metal surfaces: A review. *Surf. Sci.* **47,** 384–402 (1975).
4. Lüth, H. (Hans). *Solid Surfaces, Interfaces and Thin Films*. (Springer, 2001).

5. Groß, A. *Theoretical Surface Science*. *Theoretical Surface Science: A Microscopic Perspective* (Springer Berlin Heidelberg, 2009). doi:10.1007/978-3-540-68969-0

6. Matsushima, T. in *Reference Module in Chemistry, Molecular Sciences and Chemical Engineering* 1–5 (Elsevier, 2013). doi:10.1016/B978-0-12-409547-2.05647-X

7. Chan, C.-M., Aris, R., Weinberg, W. H. & Engineering, C. An analysis of thermal desorption mass spectra. I. *Appl. Surf. Sci.* **1,** 360–376 (1978).

8. Habenschaden, E. & Küppers, J. Evaluation of flash desorption spectra. *Surf. Sci.* **138,** L147–L150 (1984).

9. de Jong, A. M. & Niemantsverdriet, J. W. Thermal desorption analysis: Comparative test of ten commonly applied procedures. *Surf. Sci.* **233,** 355–365 (1990).

10. Tait, S. L., Dohnálek, Z., Campbell, C. T. & Kay, B. D. n-alkanes on MgO(100). I. Coverage-dependent desorption kinetics of n-butane. *J. Chem. Phys.* **122,** 164707 (2005).

11. Taylor, N. J. The role of Auger electron spectroscopy in surface elemental analysis. *Vacuum* **19,** 575–578 (1969).

12. NARUMAND, D. H. & CHILDS, K. D. Auger Spectrometers: A Tutorial Review. *Appl. Spectrosc. Rev.* **34,** 139–158 (2004).

13. Chang, C. C. Auger electron spectroscopy. *Surf. Sci.* **25,** 53–79 (1971).

14. Strobel, H. A. & Heineman, W. R. *Chemical Instrumentation: A Systematic Approach*. (John Wley & Sons, 1989).

15. Skoog, D. A., Holler, F. J. & Crouch, S. R. *Instrumental Analysis*. (Brooks Cole, 2007).

16. Chang, C. C. Auger electron spectroscopy. *Surf. Sci.* **25,** 53–79 (1971).

17. Strobel, H. A. & Heineman, W. R. *Chemical Istrumentation: A Systematic Approach*. (John Wiley & Sons, Inc., 1989).

18. Davis, L. E., MacDonald, N. C., Palmberg, P. W., Riach, G. E. & Weber, R. E. *Handbook of Auger Electron Spectroscopy*. (Perkin-Elmer Corporation, 1976).

19. Mroczkowski, S. & Lichtman, D. Calculated Auger yields and sensitivity factors for K L L – N O O transitions with 1–10 kV primary beams. *J. Vac. Sci. Technol. A Vacuum, Surfaces, Film.* **3,** 1860–1865 (1985).

20. Holloway, P. H. Thickness determination of ultrathin films by Auger electron spectroscopy. *J. Vac. Sci. Technol.* **12,** 1418–1422 (1975).

21. Yi, M. & Shen, Z. A review on mechanical exfoliation for the scalable production of graphene. *J. Mater. Chem. A* **3,** 11700–11715 (2015).

22. Taing, J., Cheng, M. H. & Hemminger, J. C. Photodeposition of Ag or Pt onto TiO 2 Nanoparticles Decorated on Step Edges of HOPG. *ACS Nano* **5,** 6325–6333 (2011).

23. Engel, T. & Reid, P. *Physical chemistry*. (Peason Education, Inc., 2010).

CHAPTER 3

Temperature programmed desorption studies of D_2O on oxide/sulfide films on W (100)

3.1 Introduction

Recently, tungsten trioxide (WO_3) has received considerable attention for is applications in gas sensing[1–4], electrochromics[5–7], and photocatalysis.[8–10] WO_3 exhibits a narrow bandgap (2.4-2.8 eV), possesses good transport properties, stability, low cost, and has been a proven material for oxygen generation from visible light – driven water oxidation.[9,11] However, due to the position of its conduction band minimum (+4 V vs. NHE at pH=0), WO_3 is not a suitable hydrogen generation photocatalyst.[8,9,12] As a result, there has been considerable effort to alter the band gap of WO_3 by non-metal doping to increase its photocatalytic efficiency for visible light – driven water splitting[13]; one of the most prevalent examples being incorporating S atoms into the WO_3 lattice.[12–17] Pacchioni and coworkers first performed density functional theory (DFT) calculations that suggest sulfur impurities will introduce S 3P states into the band gap that will effectively raise the valance band edge. In addition, the authors reported that S atoms may have the effect of introducing strain into the WO_3 lattice that will in-turn shift the conduction band minimum into the range for the redox potential of hydrogen evolution from water splitting.[12] Furthermore, Li and coworkers successfully prepared and tested the photocatalytic activity of S-doped WO_3 powders by measuring the amount of O_2 evolution from water oxidation. They reported a red shift in the fundamental absorption edge and oxygen evolution rates that were 1.25 and 1.57 times higher than un-doped WO_3 under ultra-violet (UV) and visible irradiation, respectively.[15]

From these theoretical and experimental investigations, it is clear that S-doping WO_3 is a material of great interest thus, in the present study we employ a fundamental approach to learn more about S-doped tungsten oxide systems. To do so, we describe herein a method for the preparation of a simple and reproducible mixed sulfide-oxide film on W (100) (WO_xS_y). In order to investigate the reactivity of the surface, we have performed temperature programmed desorption (TPD) experiments utilizing D_2O as a molecular probe to compare the desorption characteristics of the WO_xS_y surface with that of fully oxidized and sulfurized W (100), denoted WO_x and WS_x, respectively. Understanding the interaction of water with photocatalyst surfaces is an inherently necessary first step to understand the mechanisms involved in such reactions. Subsequently, the results of this work should serve as a starting point for future fundamental studies on S-doped tungsten oxides.

3.2 Experimental

3.2.1 *Sample Preparation*

All experiments and sample preparation were performed in an ultra-high vacuum chamber (UHV) with a base pressure of 1×10^{-10} torr, described in section 2.1 Sample surfaces were prepared *in vacuo* using a cleaned W (100) single crystal (10 mm, Princeton Scientific Corp.). The tungsten crystal was mounted on a sample holder in which tungsten heating wires were fitted into a groove around the crystal parameter to allow for resistive heating of the sample. A chromel-alumel thermocouple wire was spot-welded directly on the side of the crystal for temperature monitoring. The sample was cleaned by Ar^+ sputtering cycles using a 1 keV beam energy, 7.5×10^{-5} torr Ar (research grade, AirGas) and Auger electron spectroscopy (AES) was used to confirm the surface was free of impurities. The oxide surface was prepared by

annealing for 2 min in ~ 5×10^{-7} torr O_2 (research grade, AirGas) backfilled into the chamber via a Varian leak valve. AES was used to confirm the presence of a clean oxide layer free of adventitious carbon. Fully saturated sulfide surfaces were prepared by exposing the W (100) crystal to H_2S (Gasco, 5% H_2S balance N_2) leaked into the chamber via a directional doser with 1 μm pinhole gasket and a pressure of ~10 torr behind the doser at 300 K. Exposures (molecules) done in this manner were determined by calculating the effusion rate of the gas through the 1 μm pinhole according to section 2.5.3. For the mixed sulfide – oxide films, the surface was first exposed to a pre-saturated amount of H_2S (~1.25×10^{15} molecules) followed by exposure to oxygen (> 24 L) at 800 K.

3.2.2 *TPD measurements*

TPD experiments were performed by fist cooling the sample to ~115 K via liquid nitrogen UHV feedthroughs. A flash to at least 700 K was done prior to TPD measurements to remove any ambient adsorbates. D_2O (99.96%, Sigma Aldrich) was introduced into the chamber via a directional doser with a pressure between 1-5 torr behind a 1 μm pinhole gasket. D_2O was selected over H_2O due to a lower background concentration in the chamber as described in previous work.[18] Exposures were calculated by determining the effusion rate of the gas (3.6 $x10^{12}$ molecules/s) and by varying the dosing time, resulting in exposures ranging from 0.042 to 5.1 ($\times 10^{14}$ molecules/cm^2). TPD spectra were collected by applying a 2 K/s heating schedule and monitoring the D_2O signal as a function of temperature (K) using a UTI 100C quadrupole mass spectrometer.

3.3 Results

3.3.1 *AES and oxygen/sulfur uptake*

Figure 3.1a illustrates the AES spectra of W (100) with cumulative oxygen exposures ranging from 0.10 L to 79 L done at a sample temperature of 800 K. At initial exposures, it is observed that a small portion of adventitious carbon is present on the surface; however, with subsequent exposures at high temperature, the carbon peak (272 eV) becomes minimal as the oxygen peak increases (522 eV). Figure 3.1b shows the oxidation profile of W (100) performed at 800 K and 1000 K as a function of exposure (L). The oxygen to tungsten ratios (O:W) were obtained using normalized relative sensitivity factors obtained from Mroczkowski and Lichtman[19] for 522 eV (O) and 179 eV (W) Auger peak-to-peak intensities of Figure 3.1a. From Figure 3.1b it is seen that there is no difference between oxidation of tungsten at 800 K versus 1000 K, thus all subsequent oxidations were performed at 800 K. In addition, O:W saturates at ~3 at an exposure of ~10 L. However, based on previous studies[20–24] and the geometry of W (100) surface we believe O:W values obtained from the AES results of Figure 3.1a are over estimated and the stoichiometry of oxygen on the W (100) surface is approximately WO_2. The AES spectra presented in Figure 3.2a shows the increase in the sulfur peak (150 eV) with increasing H_2S exposure ($\times 10^{15}$ molec) on W (100) at room temperature. It is important to note that the tungsten surface was cleaned via light argon sputtering between subsequent H_2S exposures. The sulfur uptake curve (S:W) shown in Figure 3.2b, was calculated using RSF values[19] and the 150 eV and 179 eV Auger peaks for sulfur and tungsten, respectively. From Figure 3.2b it is seen that S:W saturates at ~2.5 with an exposure of 1.85×10^{15} molec. It is interesting to note that the sulfur uptake curve is linear over all pre-saturation exposures as opposed to a more Langmuirian-like behavior and will be discussed further in the proceeding.

Oxygen uptake at 800 K on pre-sulfurized (1.26×10^{15} molec H_2S) W (100) is shown in Figure 3.3. The AES spectra of cumulative oxygen exposures (Figure 3.3a) show the increase in the oxygen 522 eV peak with no change in the 150 eV sulfur peak. All AES spectra were again normalized to the 179 eV peak of tungsten. Figure 3.3b shows O:W and S:W during the oxidation of the pre-sulfurized W (100) surface. It is observed that O:W saturates ~2.7 at an exposure ~10 L, consistent with oxygen uptake on the clean W (100) (Figure 3.1b). In addition, it is observed that S:W remains unchanged over all oxygen exposures done at 800 K, demonstrating the stability of the sulfur on the surface.

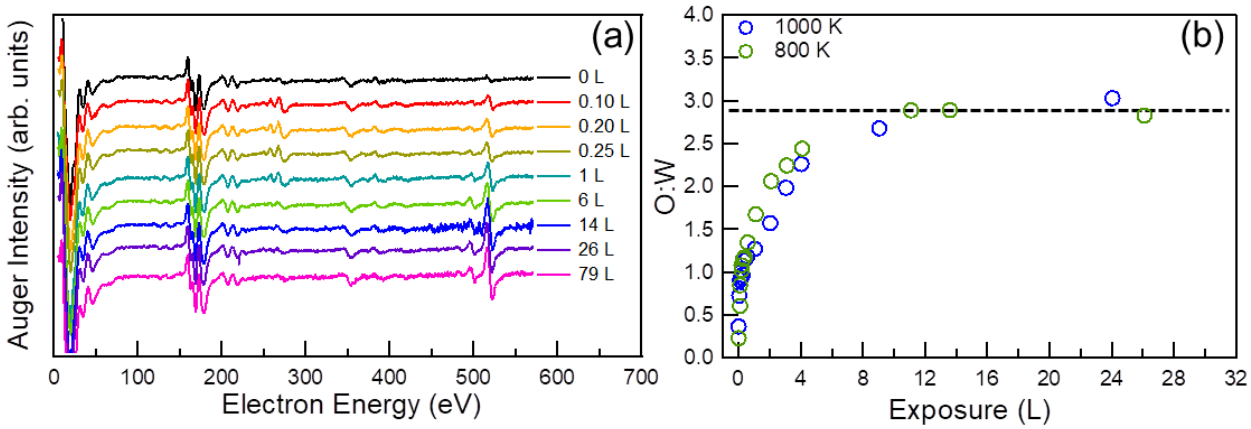

Figure 3.1. (a) AES of W (100) with varying oxygen exposure (L) and (b) corresponding oxidation profile (O:W vs exposure) done at 800 K (green points) and 1000 K (blue points). Each AES spectrum was normalized to the 179 eV peak-to peak intensity of tungsten.

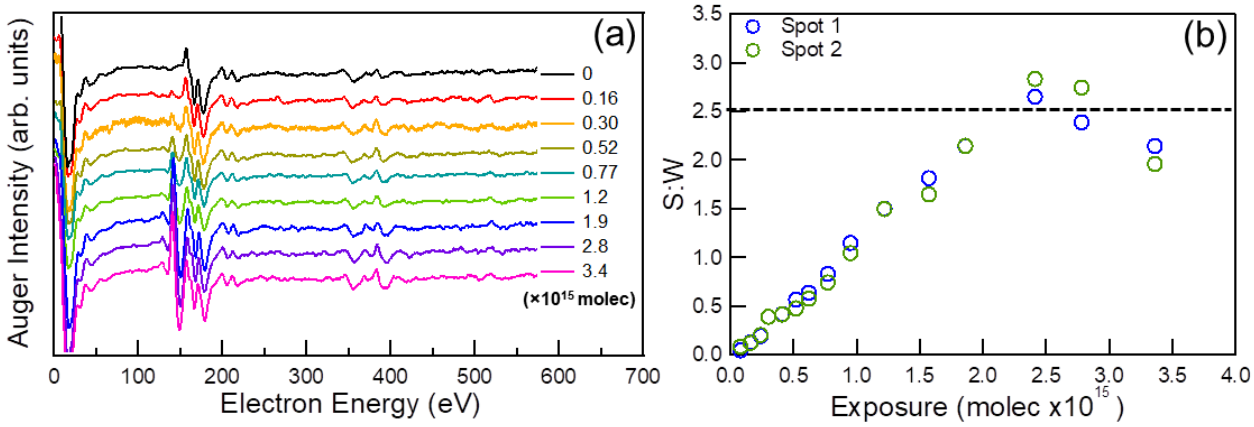

Figure 3.2. (a) AES of W (100) with varying H_2S exposure ($\times 10^{15}$ molec) and (b) corresponding sulfidation profile (S:W vs exposure). The S:W ratios were calculated for two arbitrary spots on the surface probed by the electron beam denoted spot 1 (blue points) and spot 2 (green points). Each AES spectrum was again normalized to the 179 eV peak-to-peak intensity of tungsten.

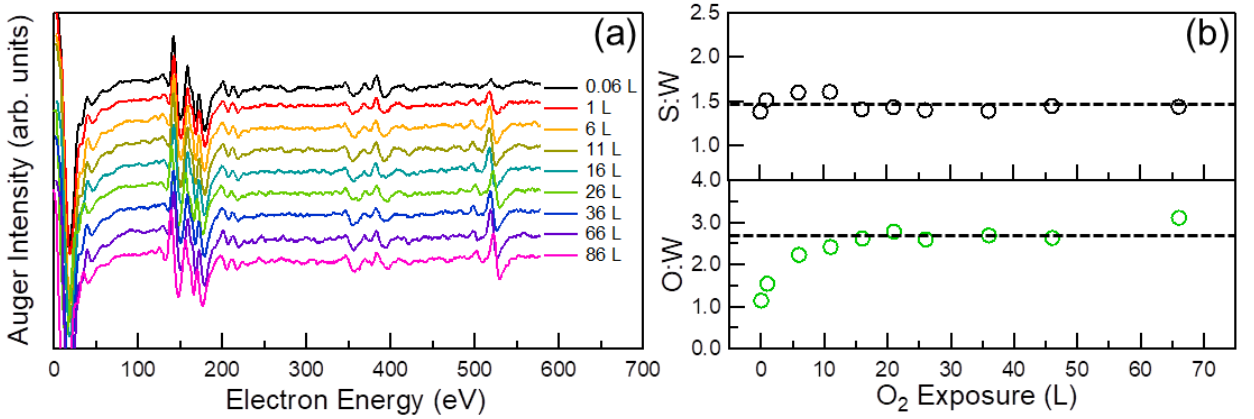

Figure 3.3. (a) AES spectra of varying O_2 exposures (L) on pre-sulfurized (1.26×10^{15} molec H_2S) W (100) and (b) corresponding oxidation (black points) and sulfidation profiles (green points), O:W and S:W, respectively. Each AES spectrum was again normalized to the 179 eV peak-to-peak intensity of tungsten.

3.3.2 *D_2O thermal desorption from WO_x, WS_x, and WO_xS_y*

The D_2O thermal desorption spectrum from oxidized tungsten (WO_x) is shown in Figure 3.4. Figure 3.4a displays the full desorption profile with monolayer coverages (ML) coverages ranging from 0.017-5.0 ML and Figure 3.4b shows "low coverages" from 0.017-0.10 ML. Coverages were determined based on the observed saturation of the monolayer in which 1 ML = 2.7×10^{15} molec/cm^2 which is in good agreement with water monolayer density on metal oxide surfaces (1×10^{15} molec/cm^2).[20,25] From Figure 3.4, four D_2O desorption states are observed on the WO_x surface. First, a high temperature state (~350 K) that is prevalent at low exposures (Figure 3.4b) is attributed to a small amount of dissociated D_2O due to defects generated during the cleaning process. The next desorption state is attributed to monolayer desorption given by peak at ~275 K that shifts to lower temperature with increasing coverage and saturates at ~190 K. An additional peak then propagates after saturation of the monolayer at ~180 K and shifts to ~167 K with increasing coverage. This state is assigned to D_2O bound in the second layer. Additionally, though not resolvable, the existence of ice multilayers becomes apparent at the highest exposures given by overlap of the leading edge for the 3.8 and 5.0 ML TPD traces. Furthermore, the high temperature desorption states of Figure 3.4a are due to D_2O desorption from the sample holder.

Figure 3.5a and 3.5b show the D_2O desorption spectra from a fully sulfurized W (100) surface and selected low doses, respectively. From the TPD spectrum, we observe a desorption state that occurs at 340 K and shifts to ~275 K and saturates at 0.5 ML. This state is tentatively assigned to OD surface species that disproportionate to desorbed D_2O. In addition, a new peak begins to grow in at 215 K and shifts to lower temperature with increasing coverage. We will again attribute this peak to a mixed monolayer and second layer that are unresolved. Lastly,

evidence of multilayer D_2O is observed at the highest coverages (3.8 and 5.0 ML) given again by the overlap of the initial onset of the desorption peak as well a slightly resolved peak at ~165 K. The high-signal intensities above 250 K observed at high exposures are again due to D_2O desorption from the sample holder.

Figure 3.6 shows desorption of D_2O from the WO_xS_y surface, where Figure 3.6a shows the full desorption profile and 3.6b shows low coverages ranging from 0.017 to 0.1 ML. From Figure 3.6b, two initial desorption states are observed. The higher temperature peak (340 K) is due to defects from sample processing and the second peak is the start of monolayer desorption beginning at ~265 K. From Figure 3.6a, the monolayer state shifts to ~180 K and saturates. A peak on the low temperature side of the monolayer state begins to populate and is ascribed to second layer D_2O which at the highest coverages is mixed with the multilayer desorption state.

For a comparative look at D_2O desorption from the three different surfaces (WO_x, WO_xS_y, and WS_x), Figure 3.7 presents overlaid TPD spectra for 0.2 ML (Figure 3.7a) and 5.0 ML (Figure 3.7b). From Figure 3.7a, it is observed that 300 K disproportionation peak is only prevalent on the WS_x surface. Additionally, the start of a monolayer desorption (215 K) becomes apparent for the WS_x spectrum and is consistent with the monolayer states of the other two tungsten surfaces. Looking at Figure 3.7b, differences in the monolayer peak for the three surfaces becomes apparent in that the monolayer peak is red shifted with increasing sulfur content on the surface. Furthermore, the blown-up region of Figure 3.7b shows the more resolved multilayer and second layer of the WS_x spectrum.

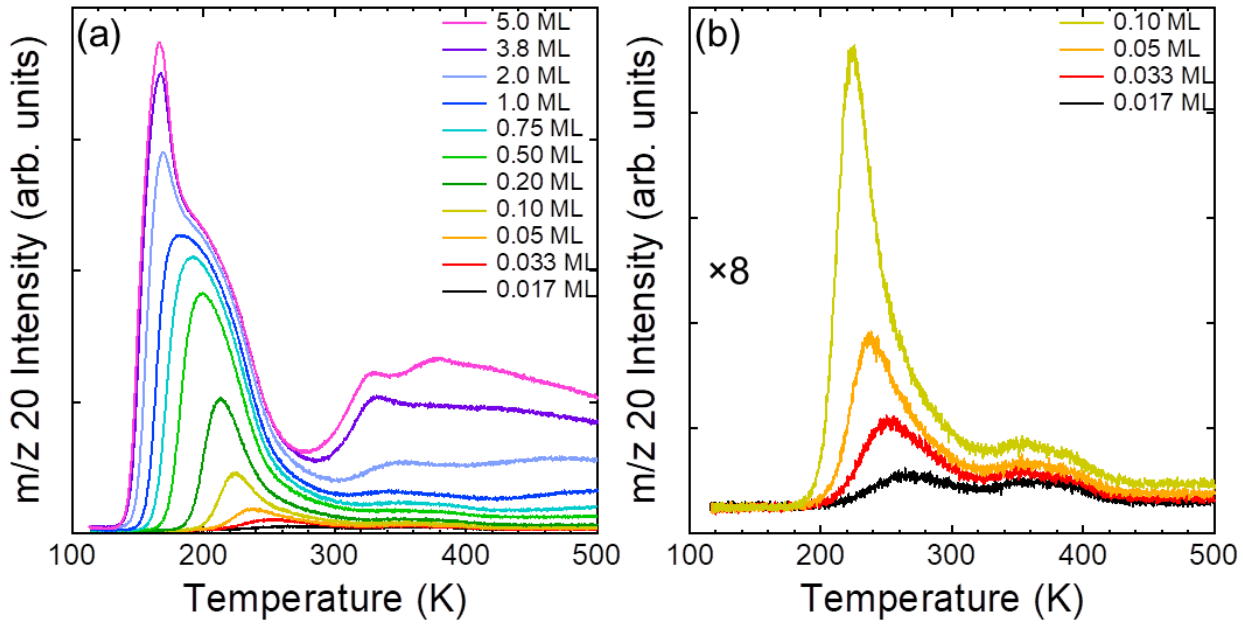

Figure 3.4. (a) D_2O desorption from the WO_x surface and (b) selective low exposures. D_2O adsorption was done at ~120 K and a heating rate of 2 K/s was used.

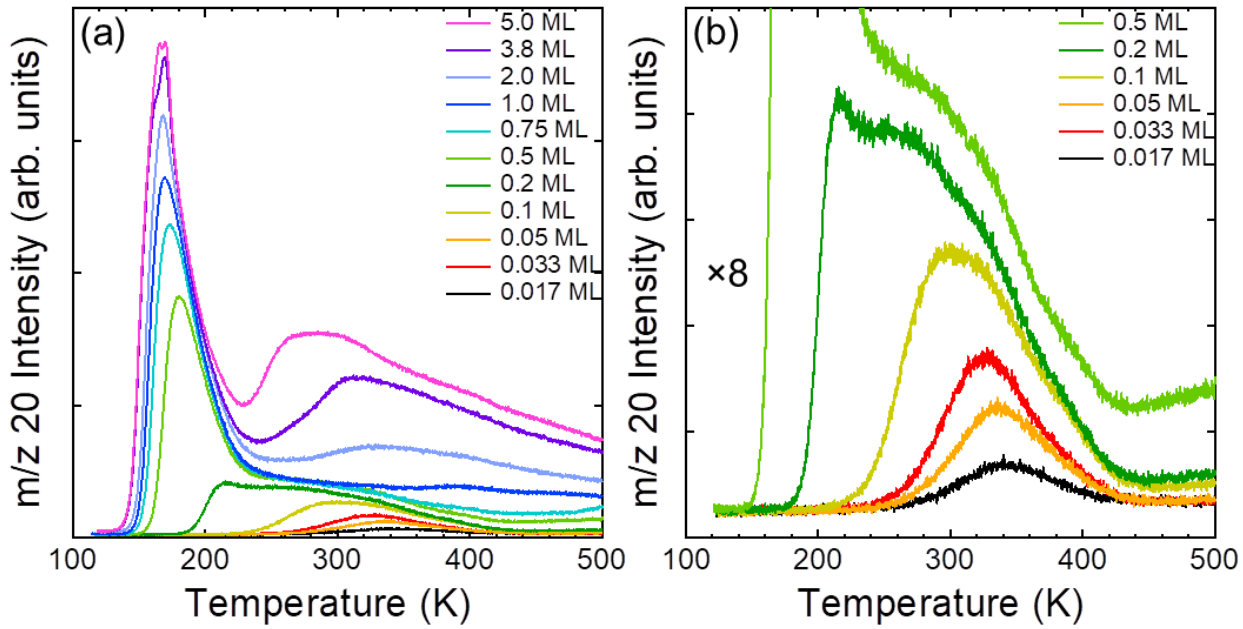

Figure 3.5. (a) D_2O desorption from the WS_x surface and (b) selective low exposures. D_2O adsorption was done at ~120 K and a heating rate of 2 K/s was used.

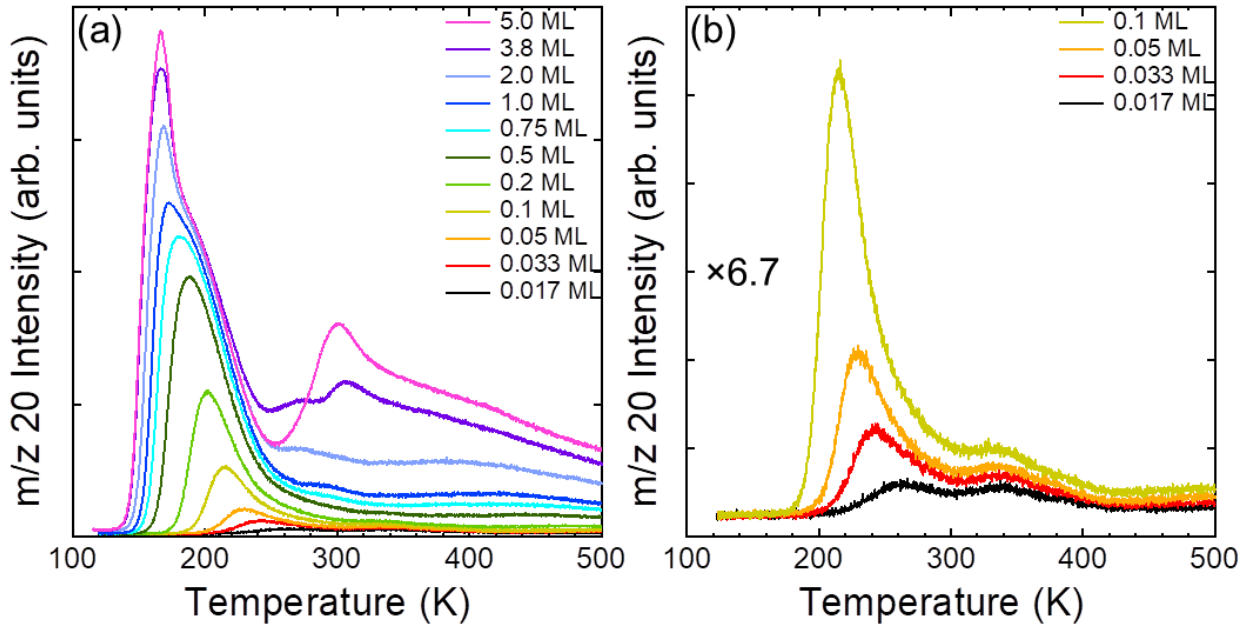

Figure 3.6. (a) D_2O desorption from the WO_xS_y surface and (b) selective low exposures. D_2O adsorption was done at ~120 K and a heating rate of 2 K/s was used.

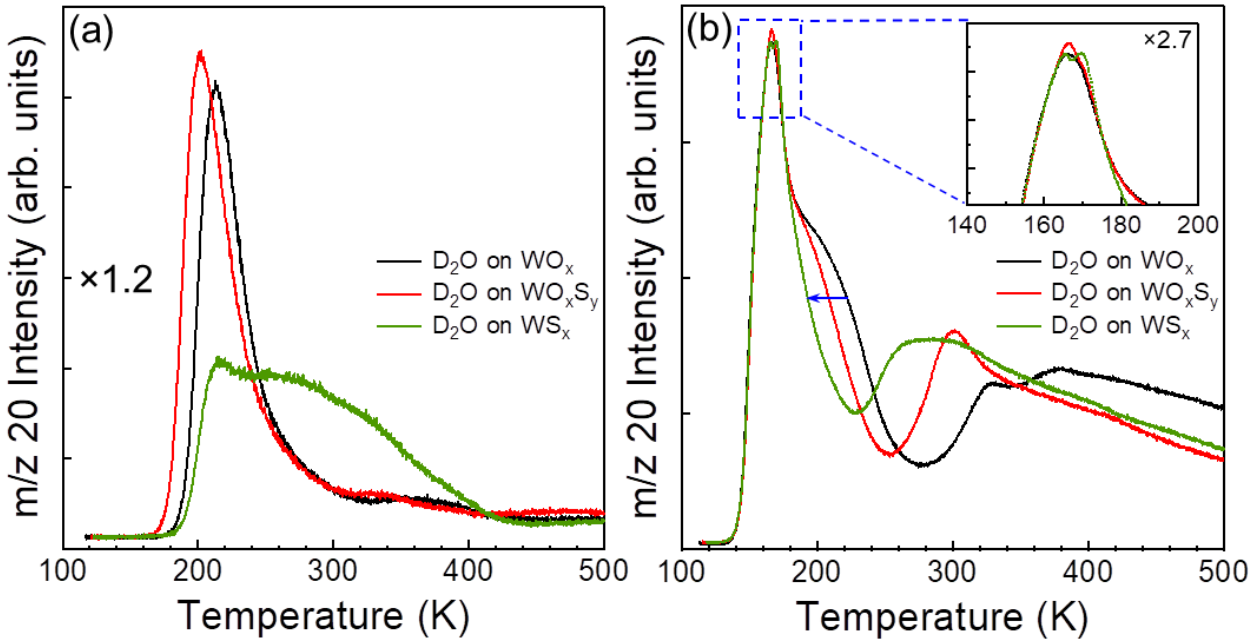

Figure 3.7. TPD overlay of (a) 0.2 ML and (b) 5.0 ML of D_2O on WO_x (black curve), WO_xS_y (red curve), and WS_x (green curve). The inset shows the zoomed-in boxed region of the multilayer.

3.3.3 *Coverage-dependent desorption energies*

For a semi-quantitative comparison of the TPD data, the inversion method[26] was used to calculate the coverage-dependent desorption energies for 0.5 ML initial coverage (Figure 3.8). The calculation was performed assuming a pre-exponential factor of 1×10^{13} sec^{-1}. Figure 3.8a shows the overlaid TPD spectra for 0.5 ML D_2O on the three surfaces investigated. At this coverage, it is apparent that the monolayer peak (~200 K) shifts towards lower temperature with increasing sulfur content on the surface. Figure 3.8b shows the D_2O activation energy of desorption (kJ/mol) as a function of the instantaneous coverage (ML). In general, at low initial coverage the energy is high (80-100 kJ/mol) and drops as the coverage increases. This is the result defect sites on the surface.[26] It is seen that over the coverage region between 0.05 – 0.2 ML the energy of D_2O on WS_x is ~10 kJ/mol larger than that of WO_x and WO_xS_y. This is due to the disproportionation peak in the TPD, only observed for the WS_x system (Figure 3.8a). The coverage region in which the energy curve begins to level (between 0.3 – 0.5 ML) is associated with monolayer desorption. Here we can see that the energy of D_2O on WS_x now drops below WO_xS_y, giving the following energy trend: $WO_x > WO_xS_y > WS_x$. The activation energies for the monolayer desorption at the peak temperature obtained from Figure 3.8 are collected in Table 3.1. Table 3.1 also includes energies calculated using the Redhead method[27] for comparison, assuming a pre-exponential factor of 1×10^{13} sec^{-1} and 2 K/s heating rate.

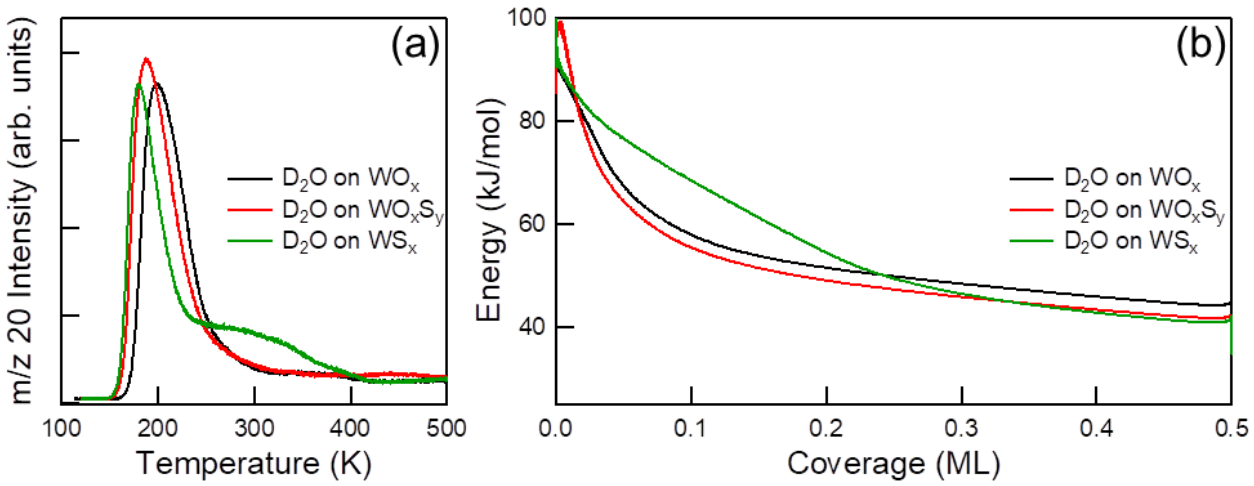

Figure 3.8. (a) TPD overlay of 0.5 ML D_2O coverages and (b) calculated coverage-dependent energy curve. The energies were calculated using the inversion method described by Kay and coworkers assuming a pre-exponential factor of 1×10^{13} sec^{-1}.[26]

Table 3.1. Activation energies of desorption (kJ/mol) for the monolayer desorption state determined from the coverage dependent energy curves of Figure 3.8 (0.50 ML) and values calculated using the Redhead method (using a heating rate of 2 K/s and assuming a pre-exponential factor of 1×10^{13} sec^{-1}).

System	Peak Temperature (K)	Redhead Energy (kJ/mol)	Coverage-dependent Energy (kJ/mol)
D_2O/ WO_x	199.0	57.1	51.1
D_2O/WO_xS_y	188.0	53.9	48.2
D_2O/ WS_x	180.2	51.6	46.1

3.4 Discussion

3.4.1 *Oxidation/sulfidation profiles*

A logical place to begin the discussion is on the nature of the three prepared surfaces, WO_x, WS_x and WO_xS_y. Oxygen adsorption on tungsten has been an intensively studied system.[21,22,24,28–32] Oxygen desorption kinetics from W (100) and Mo (100) showed evidence for the formation of atomic oxygen on the surface at ~1000 K and was also shown to undergo surface reconstruction.[24] Additionally, an investigation of oxygen diffusion using work function measurements and scanning electron beam techniques revealed that diffusion of O adatoms was inhibited by oxygen and surface tungsten place-exchange mechanisms.[28,33] Furthermore, low energy electron diffraction (LEED) of oxygen on W (100) prepared at 860 K confirmed the 1×3 overlayer structure.[20] In the present study, based on the results of previous work, we assume that the state of the oxygen on W (100) adsorbed at 800 K is atomic with minimal surface reconstruction of the (100) plane of tungsten.

H_2S on tungsten is a lesser studied system compared to that of oxygen though several groups have investigated the adsorption behavior.[34–36] H_2S adsorbed on tungsten films at -80 ºC was shown to quickly dissociate.[35,36] This is fortified by theoretical calculations that suggest H_2S adsorption on W (111) exhibits a small energy barrier for dissociative chemisorption.[34] For more insight into H_2S adsorption on W (100), we turn to studies performed on the isoelectronic Mo (100) surface.[37–41] High-resolution electron energy loss spectroscopy (HREELS) combined with TPD data indicated dissociative H_2S adsorption on Mo (100)[38,41] corroborated by density-functional theory (DFT) calculations by H. Luo and coworkers showing kinetic and thermodynamic favorability for dissociation.[40] In addition, Salmeron et al. concluded that three adsorption sites per surface Mo atom are needed for H_2S dissociation.[38] LEED studies of H_2S

adsorbed on Mo (100) between 300 and 750 K showed a predominant $\sqrt{5} \times \sqrt{5}$ overlayer structure that was shown to diminish upon heating to 1000 K and replaced by a C (2×2) structure.[37–39] Combining the results of the above studies, we assume that H_2S dissociates on the W (100) surface and upon annealing to > 700 K (prior to TPD experiments) desorbs hydrogen[42], resulting in a stable sulfide layer on the surface with a stoichiometry of WS_{2-x}. In addition, no reconstruction of the surface is expected contrary to oxygen on W (100).[29,43]

For the WO_xS_y surface, we chose to pre-sulfurize the surface with an exposure of ~1.3×10^{15} molecules H_2S, as this was approximately half-way saturated (based on full saturation of S:W ~ 2.5, Figure 3.2b). A theoretical study of sulfur oxidation on the W (111) surface revealed that sulfur adsorbed on the W (111) oxidized by O_2 led to SO_2 desorption at high temperature via the following reaction pathway[14]:

$$S_{(ads)}/W\ (111) + O_{2(g)} \rightarrow SO_{2(g)} + W\ (111) \qquad (1)$$

Based on the results of AES and oxygen uptake profile of Figure 3.3, it is clear that there was no loss of sulfur after oxidation (at 800 K) within the resolution of the spectrometer; therefore we conclude there is no subsequent oxidation of the adsorbed sulfur under the present conditions. In addition, we have performed background experiments involving partial oxidation of the W (100) surface prior to sulfurization that resulted in uptake of sulfur at room temperature. However, full sulfurization or oxidation of the tungsten crystal inhibits oxygen or sulfur uptake on the surface, respectively. Nevertheless, at the present time we do not yet have a complete picture of the nature of the WO_xS_y. Thus, more studies are imperative to gain a better understanding W (100) co-adsorbed with sulfur and oxygen.

An interesting observation from the oxygen uptake curves of Figures 3.1 – 3.3 of is that oxygen uptake on W (100) (Figure 3.1b) exhibited Langmuirian-like behavior whereas sulfur uptake (Figure 3.2b) appeared linear over the pre-saturation exposure range ($0 – 2 \times 10^{15}$ molec). One explanation for this linear behavior could be attributed to the difference in the exposure method. Exposure of the tungsten crystal to oxygen was done successively via backfilling the chamber whereas H_2S exposures were accomplished using a 1 μm pinhole orifice and directional doser. In addition, each H_2S exposure was done on the pre-cleaned W (100) surface as opposed to cumulatively. Furthermore, H_2S exposure was done at room temperature as opposed to 800 K for oxygen. The above could result in differences in the equilibrium conditions of the adsorbates interacting with the surface. An alternate explanation could lend itself to differences the adsorption process of H_2S versus O_2, in that, there likely exists unique coverage dependencies that lead to changes in the sticking probability for the two adsorbates. However, the differences in sulfur and oxygen uptake on W (100) are most likely the result of variations in experimental procedure as described above. A more in-depth analysis of this behavior is beyond the scope of this work as the uptake curves of Figures 3.1 – 3.3 were mainly intended to observe the saturation point of O and S on the surface.

3.4.2 *Temperature programmed desorption*

From the results of the TPD analysis of Figure 3.4 – 3.6, it is clear that the three surfaces studied are fundamentally different. From Figure 3.7, we see that the greatest change in the desorption behavior exists when comparing D_2O desorption from the WO_x surface versus that of WS_x. It is apparent from Figure 3.7b and 3.8a, that the monolayer desorption peak is shifted when the sulfur content is increased on the surface. This is also accompanied by a decrease in the

desorption energy as seen in Table 1 (WO_x > WO_xS_y > WS_x). The most likely explanation for this observation is due to chemical and physical properties of S atoms vs O atoms. Sulfur having a larger atomic radius than oxygen (1.8 Å vs. 1.5 Å, respectively) and a lesser electronegativity, results in a weaker interaction with the tungsten surface. This is reflected in the x-ray photoelectron spectroscopy (XPS) data for W 4f7/2 in which the binding energy for WS_2 (32.6 eV) is less than that of WO_2 (32.9 eV).[45] As a result, we suggest that this results in a weakened D_2O interaction within the first monolayer on the WS_x surface. It is clear however, that additional studies are needed to gain a more fundamental understanding of the surfaces prepared herein to subsequently better understand this phenomenon.

For the fully sulfurized surface, we see a pronounced desorption state between 300 and 340 K (Figure 3.5b) that is not present in the D_2O desorption spectra of Figure 3.4 and 3.6. An explanation for this observation may lend itself to the nature of H_2S adsorption versus O_2 on W (100). Based on the study by Salmeron et al. that suggests H_2S adsorption on Mo (100) requires ~3 Mo adsorption sites to dissociate the molecule.[38] We suggest that H_2S adsorbed on the W (100) surface also requires multiple adsorption sites for dissociation. If this is true, once the surface is heated (700 K, prior to desorption experiments) and H_2 is subsequently desorbed[42], open W adsorption sites would be left on the sulfurized surface. From looking at the 300 K peak of Figure 3.5, we suggest that the nature of these open W sites offer stronger coordination to an adsorbed D_2O molecule than a W site associated with sulfur. This is accompanied by a greater desorption energy reflected in the coverage-dependent energy curves of Figure 3.8 (green curve, between 0.05 – 2.0 ML). Thiel and Madey state that, in general, water desorption above 250 K on metal surfaces are the result of either disproportionation via:

$$2\ OH_{(ads)} \rightarrow H_2O_{(g)} + O_{(ads)} \quad (2)$$

or recombination[46]:

$$OH_{(ads)} + H_{(ads)} \rightarrow H_2O_{(g)} \quad (3)$$

or

$$2H_{(ads)} + O_{(ads)} \rightarrow H_2O_{(g)} \quad (4)$$

For water adsorbed on clean W (100), HREELs experiments revealed the presence of 77 meV and 425 meV vibrational modes associated with O-W and O-H stretching modes, respectively.[47] From these results, the authors concluded that H_2O dissociates on the W (100) surface. In addition, ultraviolet photoelectron spectroscopy (UPS) experiments revealed evidence for complete dissociation of H_2O on W (001).[48] Based on a background study of D_2O on clean W (100) (Figure S3.1) that exhibits a clear dissociative desorption state between 325-375 K, we suggest that nature of the 300 K state of D_2O on WS_x may be associated with D_2O disproportionation as opposed to recombination. AES data from the background study also concluded that the clean W (100) crystal was oxidized during the experiment, supporting the notion that the high temperature peak is likely due to disproportionation (Figure S3.2). In addition, AES before and after TPD experiments on WS_x showed slight oxidation of the surface, further evidencing disproportionation (Figure S3.3).

As previously mentioned, several studies have suggested that incorporating S atoms into the WO_3 lattice will favorably alter its electronic properties for enhanced visible light absorption.[12–15,17] This could render S-doped WO_3 a suitable material for overall water splitting thus, adsorption of water on the surface is an inherently interesting elementary step. Subsequently, for the case of WO_xS_y, we observe a weakening of the D_2O – surface interaction

within the monolayer by increasing the surface sulfur content compared to D_2O on WO_x. Incorporating sulfur onto the WO_x surface however, did not show evidence for dissociative adsorption as observed on the WS_x surface, with the exception of that on defects at low coverages. From these findings, we suggest that introducing sulfur onto the oxide surface could potentially increase the efficiency of visible light driven photolysis of water from a pure adsorption kinetic standpoint. In looking at the electrochemical oxidation reaction (Equation 6), it is seen that the reaction first involves an adsorbed OH (HO_{ads}) species in the first step followed by abstraction of a hydrogen atom in the second step to give O_{ads}.[49] Coupling this mechanism with the observed weakening of the D_2O – W interaction with the incorporation of sulfur onto the WO_x surface, we suggest that this could facilitate water dissociation in a photoelectrochemical reaction.

Reaction at anode:[49] (5)

$$2H_2O \rightarrow HO_{ads} + H_2O + H^+ + e^-$$

$$\rightarrow O_{ads} + H_2O + 2H^+ + 2e^-$$

$$\rightarrow HOO_{ads} + 3H^+ + 3e^- \rightarrow O_2 + 4H^+ + 4e^-$$

Reaction at cathode:[49] (6)

$$2H^+ + 2e^- \rightarrow H_{ads} + H^+ + e^- \rightarrow H_2$$

Given the interplay between the binding energy of the adsorbed oxygen and hydrogen species and the oxygen and hydrogen evolution activity, respectively (i.e. the volcano-relationship)[49–51], is not unreasonable to correlate these properties to the observed changes in the

desorption behavior. Nevertheless, this is the first experimental look at the interaction of water (D_2O) on the WO_xS_y surface, thus supplementary investigations are essential.

Finally we turn our attention to a previous study done by Madey and coworkers on thermal and electron-stimulated desorption of $H_2{}^{18}O$ on oxidized W (100).[20] In comparing the results from D_2O on WO_x in the present study to that of Madey et al., there is a clear disconnect in the thermal desorption data. The authors showed that $H_2{}^{18}O$ adsorbed on the oxidized W (100) surface at 25 K exhibited two major desorption states, monolayer desorption between 155 and 165 K and multilayer desorption at between 150 and 160 K. From Figure 3.4, we see that we also observe multilayer and monolayer desorption however, monolayer desorption occurred between 190 and 250 K and multilayer desorption at ~165 K. In addition, we have shown evidence for second layer D_2O that begins at ~180 K and shifts to lower temperature until it merges with the multilayer and becomes unresolvable. Discernable experimental differences between the present study* and that of Madey and coworkers[20] include: Use of D_2O* vs $H_2{}^{18}O$, 2 K/s heating rate* vs 3 K/s, 120 K adsorption temperature* vs 25 K, oxidation of W (100) at 800 K* vs 860 K, and 120 – 700 K experimental range* vs 130 – 190 K. Additionally, one of greatest differences lends itself to the preparation procedure of the tungsten crystal in that Madey and coworkers clean the surface by heating to 1600 K prior to oxidation (accomplished using an electron beam heater). In the present study, we are limited by the resistive heating capabilities of the sample holder thus, cleaning is accomplished by cycles of Ar^+ sputtering prior to oxidation. Cleaning in this manner induces defects on the tungsten surface that will subsequently bind oxygen more strongly. Moreover, we must direct our attention to the use of D_2O* versus $H_2{}^{18}O$. It is not unreasonable to assume that there likely exist differences in the adsorption/desorption behavior due to kinetic isotope effects. For example, it has been shown that D_2O on Ru (0001) exhibits significant

differences in the desorption profile compared to H_2O.[52–54] Clay et al., reported two desorption states for H_2O, denoted A1 (210 K) and A2 (165 K), attributed to the decomposition of a mixed OH/H_2O phase and in-tact water molecules, respectively. However, D_2O desorption only resulted in one desorption state (175 K) ascribed to molecular adsorption/desorption.[52] This seems to be an extreme case, however. One study on the ice crystallization kinetics on Pt (111) revealed a 4 K peak shift to higher temperature for D_2O compared to H_2O multilayers, attributed to a difference in the zero-point energies for the ice films.[55] Similarly, J.A. Smith and coworkers have conducted isothermal desorption experiments using optical interferometry for multilayers of H_2O, $H_2{}^{18}O$, and D_2O grown on Ru (001).[56] The authors reported activation energies of 13.9, 13.8, 14.8 kcal/mol for H_2O, $H_2{}^{18}O$, and D_2O, respectively. In addition, they reported that, when compared to H_2O, the isothermal desorption rate for $H_2{}^{18}O$ was ~9% slower and D_2O was 49-62% slower. The authors concluded that larger moment of inertia of D_2O (4 versus 2 for H_2O and $H_2{}^{18}O$) resulting in lower frequencies of hindered rotation on the ice surface and subsequent lower zero-point energy.[56] Obviously, multilayer desorption behavior is quite different than water interacting with the surface within the first monolayer, thus isotope effects are undoubtedly surface dependent. Based on a supporting experiment by the present author comparing D_2O and H_2O desorption on the oxidized W (100), we observe multilayer desorption that is comparable to Ref ([55]) with an observed peak temperature shift of ~3 K (Figure S3.4). Interestingly, a comparison of lower coverage data (0.2 ML) showed that the D_2O monolayer peak was shifted by ~10 K to lower temperature compared to H_2O monolayer. Thus, it is clear that isotope effects alter the desorption kinetics. This is an interesting topic of discussion, but is far beyond the scope of this work. From this, we can conclude that the extreme discrepancies between the oxidized W

(100) data presented herein and that of Madey and coworkers lays in the sample preparation differences, stated previously.

One final observation regarding the study by Madey and coworkers is the authors report a monolayer desorption energy value of 57 kJ/mol calculated using the Redhead method[27] with a pre-exponential factor of 1×10^{13} sec^{-1} which roughly agrees with the energy calculated herein (51 kJ/mol). However, based on the peak temperatures reported by Madey et al., one would expect a calculated value ~20 kJ/mol lower than the reported 57 kJ/mol.[20]

3.5 Conclusion

In this work, we sought to gain a fundamental understanding of the effect of incorporating sulfur atoms into a tungsten oxide material. For a simplistic approach, we have chosen a W (100) as a substrate that could be easily oxidized and sulfurized (H_2S) and analyzed in vacuum. In doing so, we have shown a facile method to produce thin film oxides, sulfides and mixed oxide/sulfides on the surface of W (100). The resulting surfaces were characterized using AES to elucidate the saturation points of the oxygen/sulfur uptake. Oxygen on W (100) was shown to saturate at O:W ~3, sulfur on W (100) at S:W ~2.5, and oxygen on pre-sulfurized W (100) at O:W ~ 2.7. Based on previous studies[20,37], we expect a stoichiometry of WO_2 for oxygen adsorbed on W (100) and WS_2 for H_2S adsorbed on W (100).

To examine the reactivity of three different surfaces (WO_x, WS_x, and WO_xS_y), we used D_2O as a molecular probe. The results of the TPD analyses suggest distinct differences in the desorption characteristics, most notably a shift in the monolayer desorption state to lower temperature when sulfur content is increased on the tungsten surface. We attribute these findings to a weakening of the D_2O – W interaction due to size/electronic effects of incorporating sulfur

onto the surface. This result is accompanied by a decrease in the activation energy of desorption (i.e. from 51.1 – 42.6 kJ/mol). In addition, a new peak at 300 K on the WS_x surface becomes apparent that we attribute to the disproportionation of D_2O at open defect sites.

Based on the initial work by Pacchioni and coworkers[12] that suggest S-doped WO_3 is a suitable material for visible light – driven photocatalyst, this work marks the forefront of fundamental experimental investigations of sulfur-doped tungsten oxide systems. From our results, it is apparent that sulfur incorporation affects the properties of tungsten oxide systems, specifically water adsorption. Thus, more studies are imperative to further develop a better understanding of the chemical properties of these systems.

3.6 References

1. Smith, D. J., Vatelino, J. F., Falconer, R. S. & Wittman, E. L. Stability, sensitivity and selectivity of tungsten trioxide films for sensing applications. *Sensors Actuators B Chem.* **13,** 264–268 (1993).
2. Frühberger, B., Grunze, M. & Dwyer, D. J. Surface chemistry of H2S-sensitive tungsten oxide films. *Sensors Actuators B Chem.* **31,** 167–174 (1996).
3. Chang, X., Sun, S. & Yin, Y. Green synthesis of tungsten trioxide monohydrate nanosheets as gas sensor. *Mater. Chem. Phys.* **126,** 717–721 (2011).
4. Chi, X. *et al.* Tungsten trioxide nanotubes with high sensitive and selective properties to acetone. *Sensors Actuators B Chem.* **194,** 33–37 (2014).
5. Lusis, A., Kleperis, J. & Pentjušs, E. Model of electrochromic and related phenomena in tungsten oxide thin films. *J. Solid State Electrochem.* **7,** 106–112 (2003).
6. Granqvist, C. . Electrochromic tungsten oxide films: Review of progress 1993–1998. *Sol.*

Energy Mater. Sol. Cells **60,** 201–262 (2000).

7. Regragui, M. *et al.* Preparation and characterization of pyrolytic spray deposited electrochromic tungsten trioxide films. *Thin Solid Films* **358,** 40–45 (2000).
8. Bamwenda, G. R. & Arakawa, H. The visible light induced photocatalytic activity of tungsten trioxide powders. *Appl. Catal. A Gen.* **210,** 181–191 (2001).
9. Ahmad, H., Kamarudin, S. K., Minggu, L. J. & Kassim, M. Hydrogen from photo-catalytic water splitting process: A review. *Renew. Sustain. Energy Rev.* **43,** 599–610 (2015).
10. Liu, R. *et al.* Water Splitting by Tungsten Oxide Prepared by Atomic Layer Deposition and Decorated with an Oxygen-Evolving Catalyst. *Angew. Chemie* **123,** 519–522 (2011).
11. Chueh, W. C. *et al.* High-Flux Solar-Driven Thermochemical Dissociation of CO2 and H2O Using Nonstoichiometric Ceria. *Science (80-.).* **330,** 1797–1801 (2010).
12. Wang, F., Di Valentin, C. & Pacchioni, G. Doping of WO 3 for Photocatalytic Water Splitting: Hints from Density Functional Theory. *J. Phys. Chem. C* **116,** 8901–8909 (2012).
13. Marschall, R. & Wang, L. Non-metal doping of transition metal oxides for visible-light photocatalysis. *Catal. Today* **225,** 111–135 (2014).
14. Rettie, A. J. E. *et al.* Improved Visible Light Harvesting of WO 3 by Incorporation of Sulfur or Iodine: A Tale of Two Impurities. *Chem. Mater.* **26,** 1670–1677 (2014).
15. Li, W., Li, J., Wang, X. & Chen, Q. Preparation and water-splitting photocatalytic behavior of S-doped WO3. *Appl. Surf. Sci.* **263,** 157–162 (2012).
16. Migas, D. B., Shaposhnikov, V. L., Rodin, V. N. & Borisenko, V. E. Tungsten oxides. I. Effects of oxygen vacancies and doping on electronic and optical properties of different

phases of WO3. *J. Appl. Phys.* **108,** 93713 (2010).

17. Di Valentin, C., Wang, F. & Pacchioni, G. Tungsten Oxide in Catalysis and Photocatalysis: Hints from DFT. *Top. Catal.* **56,** 1404–1419 (2013).
18. Grimm, R. L., Tobias, D. J. & Hemminger, J. C. D2O water interaction with textured carboxylic acid-terminated monolayer surfaces characterized by temperature-programmed desorption and molecular dynamics. *J. Phys. Chem. C* **114,** 1570–1579 (2010).
19. Mroczkowski, S. & Lichtman, D. Calculated Auger yields and sensitivity factors for K L L – N O O transitions with 1–10 kV primary beams. *J. Vac. Sci. Technol. A Vacuum, Surfaces, Film.* **3,** 1860–1865 (1985).
20. Akbulut, M., Sack, N. J. & Madey, T. E. Adsorption and reaction of water on oxidized tungsten: thermal desorption and electron stimulated desorption measurements. *Surf. Sci.* **351,** 209–227 (1996).
21. Bauer, E., Poppa, H. & Viswanath, Y. Adsorption of oxygen on W(100): Adsorption kinetics and structure. *Surf. Sci.* **58,** 517–549 (1976).
22. King, D. a., Madey, T. E. & Yates, J. T. Interaction of Oxygen with Polycrystalline Tungsten. I. Sticking Probabilities and Desorption Spectra. *J. Chem. Phys.* **55,** 3236–3246 (1971).
23. King, D. a., Madey, T. E. & Yates, J. T. Interaction of Oxygen with Polycrystalline Tungsten. II. Corrosive Oxidation. *J. Chem. Phys.* **55,** 3247–3253 (1971).
24. Vas'ko, N. P., Ptushinskii, Y. G. & Chuikov, B. A. On the state of oxygen adsorbed on the surface of tungsten and molybdenum single crystals. *Surf. Sci.* **14,** 448–456 (1969).
25. Henrich, V. E. and C. P. A. *The Surface Science of Metal Oxides*. (Cambridge University Press, 1994). doi:10.1002/anie.199603471

26. Tait, S. L., Dohnálek, Z., Campbell, C. T. & Kay, B. D. n-alkanes on MgO(100). I. Coverage-dependent desorption kinetics of n-butane. *J. Chem. Phys.* **122,** 164707 (2005).

27. Redhead, P. P. a. Thermal desorption of gases. *Vacuum* **12,** 203–211 (1962).

28. Bowker, M. & King, D. A. Oxygen diffusion on tungsten single crystal surfaces: Secondary electron emission studies. *Surf. Sci.* **94,** 564–580 (1980).

29. Murphy, S., Manai, G. & Shvets, I. V. Oxygen-induced p(3×1) reconstruction of the W(100) surface. *Surf. Sci.* **579,** 65–72 (2005).

30. Anderson, J. & Danforth, W. E. Low energy electron diffraction study of the adsorption of oxygen on a (100) Tungsten surface. *J. Franklin Inst.* **279,** 160–168 (1965).

31. Alnot, P., Auerbach, D. J., Behm, J., Brundle, C. R. & Viescas, A. A surface core-level shift photoemission study of the interaction of oxygen with W{100}. *Surf. Sci.* **213,** 1–24 (1989).

32. Musket, R. G. G. Room-temperature adsorption of oxygen on tungsten surfaces: A review. *J. Less Common Met.* **22,** 175–191 (1970).

33. Wells, M. G. & King, D. A. Chemisorption of oxygen on tungsten (100): combined molecular beam and scanning electron beam study. *J. Phys. C Solid State Phys.* **7,** 4053–4068 (1974).

34. Peng, S.-F. & Ho, J.-J. Theoretical Study of H 2 S Dissociation and Sulfur Oxidation on a W(111) Surface. *J. Phys. Chem. C* **114,** 19489–19495 (2010).

35. Saleh, J. M., Kemball, C. & Roberts, M. W. Interaction of hydrogen sulphide with nickel, tungsten and silver films. *Trans. Faraday Soc.* **57,** 1771 (1961).

36. Saleh, J. M. Chemisorption on platinum and tungsten. *Trans. Faraday Soc.* **67,** 1830 (1971).

37. Wilson, J. M. LEED and AES study of the interaction of H2S and Mo (100). *Surf. Sci.* **53,** 330–340 (1975).

38. Salmeron, M., Somorjai, G. A. & Chianelli, R. R. A leed-aes study of the structure of sulfur monolayers on the Mo(100) crystal face. *Surf. Sci.* **127,** 526–540 (1983).

39. Tabor, D. & Wilson, J. M. Low energy electron diffraction study of O2 and H2S adsorption on Mo (100). *J. Cryst. Growth* **9,** 60–67 (1971).

40. Luo, H., Cai, J., Tao, X. & Tan, M. Adsorption and dissociation of H2S on Mo(100) surface by first-principles study. *Appl. Surf. Sci.* **292,** 328–335 (2014).

41. Gland, J. L., Kollin, E. B. & Zaera, F. Adsorbed sulfhydryl (SH) on the molybdenum(100) surface. *Langmuir* **4,** 118–120 (1988).

42. Tamm, P. W. & Schmidt, L. D. Binding States of Hydrogen on Tungsten. *J. Chem. Phys.* **54,** 4775–4787 (1971).

43. Kramer, H. & Bauer, E. The reconstruction of the W(100) surface in the presence of half a monolayer of oxygen II. Kinetics of the reconstruction. *Surf. Sci.* **93,** 407–422 (1980).

44. Meubus, P. High Temperature Reaction Kinetics of Tungsten with Sulfur Dioxide. *J. Electrochem. Soc.* **125,** 1636 (1978).

45. Naumkin, A. V., Kraut-Vass, A., Gaarenstroom, S. W., Powell, C. J. NIST X-ray Photoelectron Spectroscopy Database, NIST Standard Reference Database Number 20. (2000). doi:10.18434/T4T88K

46. Thiel, P. A. & Madey, T. E. The interaction of water with solid surfaces: Fundamental aspects. *Surf. Sci. Rep.* **7,** 211–385 (1987).

47. Propst, F. M. & Piper, T. C. Detection of the Vibrational States of Gases Adsorbed on Tungsten by Low-Energy Electron Scattering. *J. Vac. Sci. Technol.* **4,** 53–56 (1967).

48. Mueller, D. *et al.* A synchrotron radiation study of BaO films on W(001) and their interaction with H 2 O, CO 2 , and O 2. *J. Vac. Sci. Technol. A Vacuum, Surfaces, Film.* **6,** 1067–1071 (1988).

49. Rossmeisl, J., Qu, Z.-W., Zhu, H., Kroes, G.-J. & Nørskov, J. K. Electrolysis of water on oxide surfaces. *J. Electroanal. Chem.* **607,** 83–89 (2007).

50. Zeradjanin, A. R., Grote, J. P., Polymeros, G. & Mayrhofer, K. J. J. A Critical Review on Hydrogen Evolution Electrocatalysis: Re-exploring the Volcano-relationship. *Electroanalysis* **28,** 2256–2269 (2016).

51. Chen, W.-F., Muckerman, J. T. & Fujita, E. Recent developments in transition metal carbides and nitrides as hydrogen evolution electrocatalysts. *Chem. Commun.* **49,** 8896 (2013).

52. Clay, C., Haq, S. & Hodgson, A. Intact and dissociative adsorption of water on Ru(0001). *Chem. Phys. Lett.* **388,** 89–93 (2004).

53. Hodgson, A. & Haq, S. Water adsorption and the wetting of metal surfaces. *Surf. Sci. Rep.* **64,** 381–451 (2009).

54. Henderson, M. The interaction of water with solid surfaces: fundamental aspects revisited. *Surf. Sci. Rep.* **46,** 1–308 (2002).

55. Smith, R. S., Matthiesen, J., Knox, J. & Kay, B. D. Crystallization Kinetics and Excess Free Energy of H 2 O and D 2 O Nanoscale Films of Amorphous Solid Water. *J. Phys. Chem. A* **115,** 5908–5917 (2011).

56. Smith, J. A., Livingston, F. E. & George, S. M. Isothermal Desorption Kinetics of Crystalline H 2 O, H 2 18 O, and D 2 O Ice Multilayers. *J. Phys. Chem. B* **107,** 3871–3877 (2003).

CHAPTER 4

Thermal desorption of D_2O on TiO_2 heterostructures supported on HOPG

4.1 Introduction

Titanium dioxide has long received considerable attention due to its applicability in numerous fields including electrochemistry, heterogeneous catalysis, photocatalysis, photo-degradation of pollutants, sensors and protective coatings, among others.[1–4] As a result, TiO_2 has become one of the most widely-studied materials. Within its areas of use, the adsorption of water on the surface of TiO_2 is an inherently relevant process, thus, there has been substantial effort devoted to gaining a fundamental understanding of water on these materials. Currently in the literature, the majority of the investigations of water on TiO_2 have been performed on single crystal and powder samples.[1,5,14–17,6–13] with rutile (110) being the most heavily studied due to its thermodynamic stability.[1,5,9] Since single crystals provide well-defined, reproducible surface structures with minimal defects, they are often exploited to obtain fundamental interfacial information, such as the type of adsorption sites, reactivity and desorption kinetics. However, despite the advantages of using single crystals, they are quite different from the types of materials used in industrial processes, i.e. powders and colloidal solutions. This disconnect is often referred to as the "complexity gap".[18] Furthermore, TiO_2 powders are much more catalytically relevant materials, but are difficult to understand as a consequence of the complexity of the samples. Thus, there is a clear need for more complex yet controllable model TiO_2 systems to help close the complexity gap.[19]

In recent years, TiO_2 nanomaterials and thin films have made their way into model systems for catalysis. Materials such as 1D arrays of TiO_2 nanorods and nanotubes have been

reported in the literature in an effort to design improved model catalysts.[19,20] In addition, TiO_2 nanoparticles have been shown to be a suitable support material for precious metal nanoparticles such as platinum or silver.[21] Furthermore, it has been shown that the size and morphology of TiO_2 nanoparticles supported on highly oriented pyrolytic graphite (HOPG) can be precisely controlled by physical vapor deposition (PVD) by varying the substrate temperature upon deposition.[21] In this work we have prepared different TiO_2 heterostructures supported on HOPG with morphologies ranging from ranging from linear arrays of nanoparticles to thin films prepared by PVD. With ability to control the complexity of the TiO_2 system, we can investigate the role the morphology may play on the reactivity.

Historically, temperature programmed desorption (TPD) has been a useful tool in probing the surface of TiO_2 single crystals, however to our knowledge, there have been no water desorption studies on any supported TiO_2 nanoparticles or other heterostructure systems. Thus, the goal of the present study is to assess the differences in water reactivity on TiO_2 as a function of particle morphology using TPD. In this work, Isotopically labeled water (D_2O) was used to probe different TiO_2 heterostructures supported on HOPG, including: a TiO_2 thin film, dendrites, linear dendrites, nanoparticles and high-density nanoparticles, in which we show that variation in the TiO_2 morphology leads to pronounced changes in the thermal desorption spectra.

4.2 Experimental

4.2.1 *Sample Preparation*

TiO_2 samples were prepared *ex situ* by PVD in a bell jar evaporator under high vacuum conditions (~1 x 10^{-7} torr) as described previously [21]. A quartz crystal microbalance was used to measure the amount of titanium deposited on the HOPG substrates. By varying the sample

holder temperature and subsequent adatom mobility, the morphology of the TiO_2 particles was controlled. TiO_2 thin films resulted from a 1 hour anneal at a sample temperature of 200 °C with a deposition flux of 0.1 nm/min and deposition thickness of 1.2 nm. For the preparation of dendrites, linear dendrites and nanoparticles, HOPG substrates were heated to temperatures of 300 ºC, 400 ºC, and 800 ºC during Ti deposition, respectively (Figure 4.1). The high-density nanoparticles were prepared by pretreating the HOPG substrate with oxygen plasma, followed by deposition and annealing at 800 ºC The deposition flux and thickness were kept constant for all samples, 0.1 nm/min and 1.2 nm, respectively. Each sample was annealed for 2 hours after deposition to allow for proper migration of the particles to the step edges of the HOPG surface. Furthermore, bare HOPG samples were cut to a similar thickness as the TiO_2 supported samples and cleaved with scotch tape for use in background experiments.

4.2.2 *Surface Characterization*

Scanning electron microscopy (SEM) was used to confirm the sample morphology of the TiO_2 structures. High resolution imaging was performed with an FEI Magellan XHR 400L SEM at the Laboratory for Electron and X-ray Instrumentation (LEXI) facility at the University of California Irvine. A beam energy of 10 keV and a sample current of 50 pA was used to image the samples before and after TPD analysis. A second FEI Nova NanoSEM 450, housed at the Joint Center for Artificial Photosynthesis at the California Institute of Technology, was used to obtain images of the TiO_2 dendrite and linear dendrite samples using a beam energy of 10 keV and a current of 214 µA.

Auger electron spectroscopy (AES) characterization was performed *in situ*, prior to TPD experiments, using a beam energy of 2 keV. X-ray photoelectron spectroscopy (XPS) was

performed in a Kratos Axis Ultra instrument, housed at the Joint Center for Artificial Photosynthesis at the California Institute of Technology, using Al-Kα monochromatic source at 15 keV and 10 mA emission current. A 20 eV pass energy was used for high resolutions scans, using a 0.05 eV/step and a 300 ms dwell time. XPS data was analyzed using CASA software, where each peak was deconvoluted using a full Gaussian fit and a Shirley background subtraction. The Ti 2p 3/2 and Ti 2p ½ peak areas were constrained in a ratio 2:1. The peak splitting between the 3/2 and ½ peak was determined to be 5.7 eV for all TiO_2 materials.

4.2.3 *TPD measurements*

All TPD experiments were performed in an ultra-high vacuum (UHV) chamber with a base pressure of ~1 x 10^{-10} torr. Each sample was mounted on a removable sample holder where a chromel-alumel thermocouple wire and tungsten heating wires were sandwiched between the TiO_2 sample and a freshly cleaved HOPG sample of similar thickness to allow firm contact of the wires with the sample. Custom made tantalum foil clips and backing tantalum plates were used to compress the TiO_2 sample and backing HOPG in place. The Ta clips were fastened to the Ta backing plates with molybdenum screws to avoid seizing to after heating cycles. To ensure that the TPD signal is a product of only the sample and not the sample holder components, a background TPD experiment was conducted using the same tantalum foil used in the construction of the front clips. These results confirmed that little desorption signal is detected in the mass spectrometer from the tantalum clips or the copper pieces on the manipulator.

D_2O (99.96%, Sigma Aldrich) contained in a Pyrex bulb with a stainless steel neck was fitted to the manifold for surface exposures. D_2O was chosen instead of H_2O as a result of a

lower background concentration in the chamber as described in past work [22]. Several freeze-pump-thaw cycles were used to ensure D_2O purity prior to desorption experiments.

To obtain TPD spectra, samples were first were cooled to temperatures between 100K and 110K before the surface was exposed to D_2O for a given amount of time (seconds) via a directional doser at a pressure of 1 torr behind a 1 μm pinhole gasket. The effusion rate of the gas was calculated to be 3.56 $x10^{12}$ molecules/s leading to exposures ranging from 0.042 to 5.1 ($\times10^{14}$ molecules/cm^2) experiments. Samples were heated to > 500 K using a temperature ramp of 2 K/s and desorbing D_2O signal was monitored using a UTI 100C quadrupole mass spectrometer (MS).

4.3 Results

4.3.1 *Surface characterization*

Figure 4.1a-e shows SEM images of the TiO_2 morphologies supported on HOPG. The resultant TiO_2 structures were formed by taking advantage of the terraces and step edges of the HOPG substrate. By increasing the thermal energy during deposition, the Ti adatoms laterally diffuse on the surface where they may then aggregate, coalesce and orient themselves at the step edges and point defects of the HOPG substrate, as described previously.[21] The surfaces depicted in Figure 4.1 are a TiO_2 (a) thin film, (b) dendrites, (c) linear dendrites, (d) nanoparticles and (e) high-density nanoparticles grown at sample temperatures of 200ºC, 300ºC, 400ºC, 800ºC and 800ºC, respectively. The high-density nanoparticle sample was prepared by pretreating the HOPG substrate with O_2 plasma to generate defects and subsequent nucleation sites for particle formation. The nanoparticles of Figure 4.1d and 4.1e are ~10nm in diameter and TEM diffraction confirmed the rutile structure for the linear nanoparticles[21] and a mix of rutile and

anatase for the high-density nanoparticles (Figure S4.1 and S4.2) However, an explicit crystal structure for all other TiO_2 samples was indeterminable from TEM diffraction.

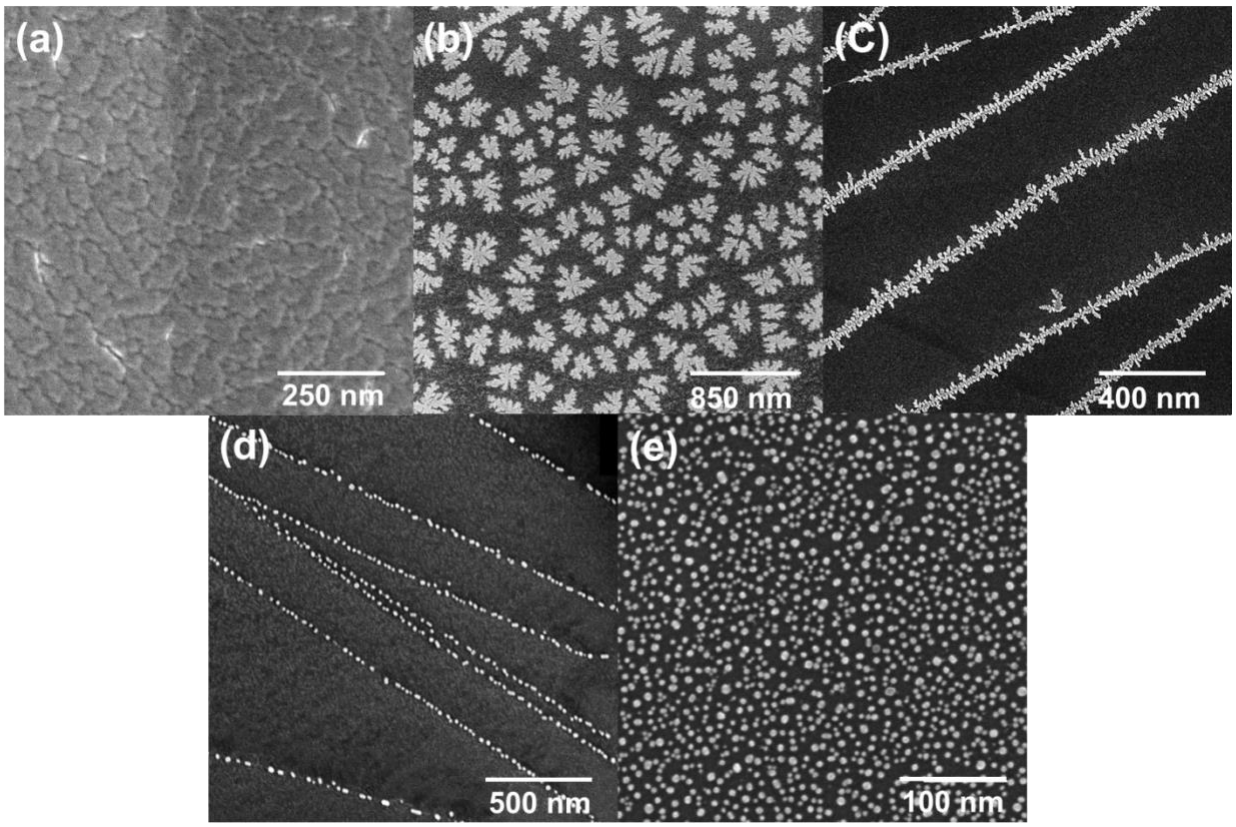

Figure 4.1. SEM images of TiO_2 (a) thin film, (b) dendrites, (c) linear dendrites, (d) nanoparticle and (e) high-density nanoparticles. (a) a non-uniform TiO_2 thin film prepared at a substrate temperature of 200ºC (b) dendritic islands grown at a substrate temperature of 300 ºC (c) linear dendritic arrays grown at a substrate temperature of 400 ºC (d) well-ordered linear arrays of spherical and rod-shaped nanoparticle structures at the HOPG step edges with average particle sizes of ~10 nm (e) high-density nanoparticles grown on oxygen plasma treated HOPG at 800 ºC.

AES and XPS were used to investigate surface composition of each of the samples. Figure 4.2 shows the AES spectra for the different TiO_2 morphologies. All AES spectra yielded peaks for carbon, titanium and oxygen. For qualitative comparison, each sample spectrum was normalized to the carbon peak intensity. In doing so, the amount of titanium on the surfaces decreases between samples as follows: thin film > high density nanoparticles > dendrites > linear

dendrites > nanoparticles, where the Ti and O signal for the nanoparticle sample is difficult to resolve. From XPS (Figure S4.3), the Ti 2p spectra for each of the different morphologies yielded peaks for Ti $2p_{3/2}$ and Ti $2p_{1/2}$ of 459.4 and 465.1 eV, respectively, with a peak splitting of 5.7 eV (ref). The C 1s spectra for all samples show sp^2 carbon peaks at 284.8 eV. The TiO_2 thin film sample showed additional peaks in the C 1s spectrum that correspond to adventitious carbon bound to the surface of the TiO_2. In other samples, these peaks were not resolvable due to a high sp^2 carbon signal from the underlying HOPG substrate. The O 1s spectra yielded two major peaks, the first due to the lattice oxygen of TiO_2 at ~531 eV for all TiO_2 morphologies. Furthermore, a peak at ~532 eV was also observed in the O 1s spectra and is attributed to surface oxygen species.

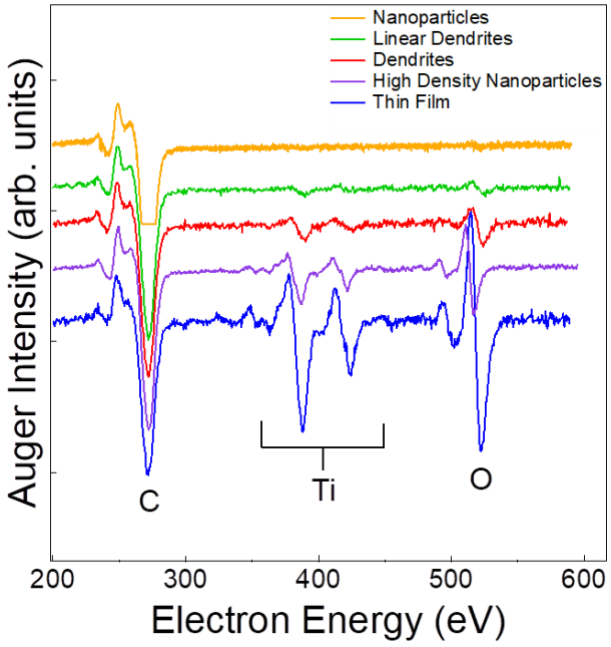

Figure 4.122. Auger electron spectra of TiO_2 nanoparticles (gold), linear dendrites (green), dendrites (red), high-density nanoparticles (purple) and thin film (blue). C: 272 eV, Ti: 388 eV & 424 eV, O: 522 eV.

4.3.2 *D_2O thermal desorption*

Figures 4.3a-e show the D_2O TPD spectra of the different TiO_2 heterostructures supported on HOPG. D_2O on the TiO_2 thin film (Figure 4.3a) yielded two major desorption features. The low temperature peak (*iii)* is assigned to a D_2O multilayer and the broad high temperature peak (*i*) is assigned to D_2O bound to Ti^{4+} sites on the surface.[1,5–7,14,23] For convenience, this peak will be referred to as the monolayer peak, despite no observed saturation of the desorption state (to be discussed in the subsequent section). In addition, a shoulder on the high temperature side of the monolayer peak (Figure 4.3a and 4.3d) is assigned as a small portion of D_2O that dissociates at defect sites and recombines to desorb molecularly as previously described for H_2O on TiO_2 (110)[1]. The desorption spectra in Figure 4.3b-e also exhibit peaks associated with D_2O multilayer and monolayer desorption however, an additional peak (*ii*) is now observed between the multilayer and monolayer states. This peak is assigned to D_2O bound to TiO_2 oxygen anion sites (denoted as "2nd layer").[1,5,6] Furthermore, Figure 4.3f shows D_2O desorption from a freshly cleaved piece of HOPG which only yielded multilayer and monolayer peaks, where in this case, the monolayer state is due to water bound at the step edges and point defects of the HOPG substrate. In all instances, D_2O multilayer desorption occurs at ~155 K, and the 2nd layer and monolayer peaks shift to lower temperature with increasing exposure.

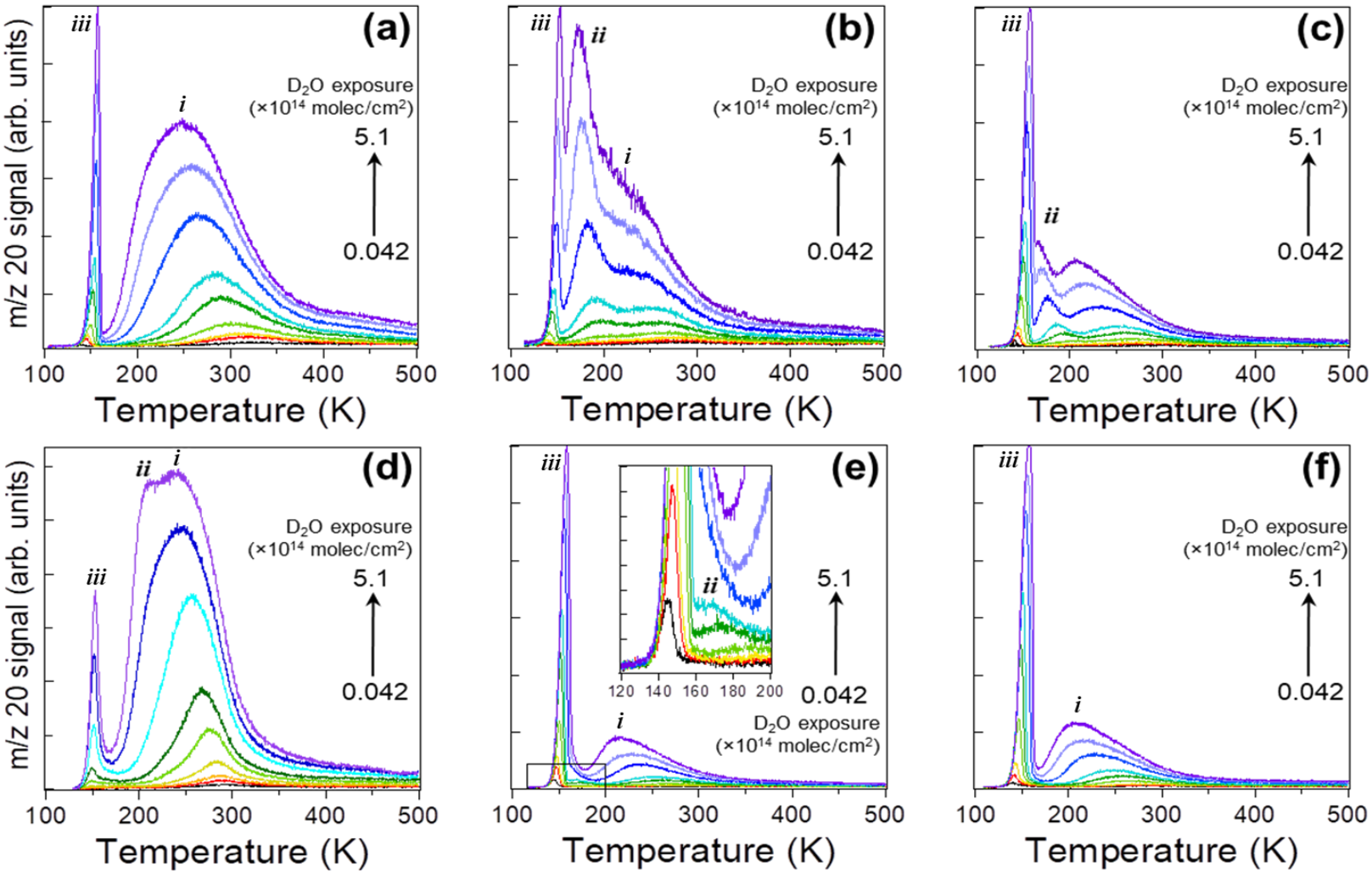

Figure 4.3. TPD spectra of D_2O on (a) TiO_2 thin film, (b) dendrites, (c) linear dendrites, (d) high-density nanoparticles, (e) nanoparticles and (f) HOPG with exposures ranging from 4.2×10^{12} molec/cm^2 to 5.1×10^{14} molec/cm^2. Peak *iii* is the multilayer state, peak *ii* is denoted as second layer and peak *i* is denoted as the monolayer state.

Figure 4.4a shows the 2nd layer desorption peak temperatures as a function of exposure (× 10^{14} molec/cm^2) (peak *ii* of Figure 4.3) for the TiO_2 dendrites, linear dendrites, nanoparticles and high-density nanoparticles. The peak temperature of this state for the aforementioned samples shifts toward lower temperature with increasing exposure. In addition, the TiO_2 high-density nanoparticle sample exhibits the highest peak temperatures, followed by the dendrites and linear dendrites and nanoparticles, respectively. It is interesting to note, the high-density nanoparticle sample's second layer only becomes pronounced at high exposures, as evident in the TPD spectrum in Figure 4.3d. From Figure 4.4b it is observed that the monolayer peak temperatures for the majority of the samples exhibit a similar trend, with the exception of the TiO_2 thin film and high-density nanoparticle samples which are shifted by ~40 K and ~20 K, respectively. In all cases the monolayer peak shifts to lower temperatures with increasing D_2O exposure which is in good agreement with water on TiO_2 (110) and (100).[1,5,24]

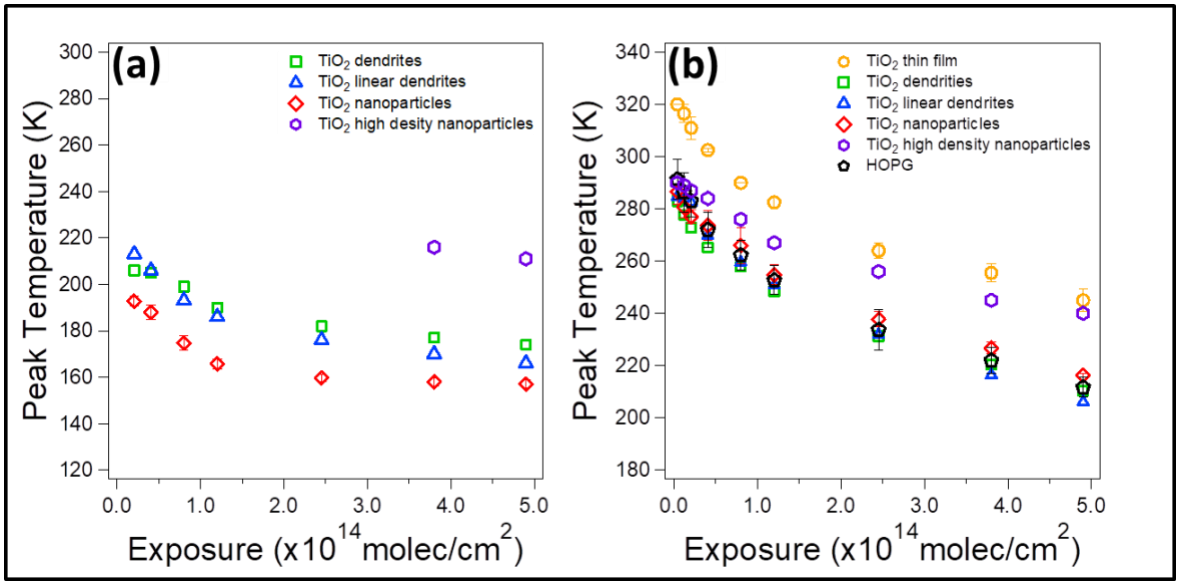

Figure 4.4. Desorption peak temperature as a function of exposure (× 10^{14} molec/cm^2) for the (a) 2nd layer and (b) monolayer.

4.3.3 *Desorption energies of TiO2 heterostructures*

The activation energies of desorption (E_{des}) were calculated for the 2nd and monolayer peaks in the TPD spectra for each of the samples and are reported in Table 1. Desorption energies for the 2nd layer and monolayer peaks were calculated using the Redhead method[25] assuming first order desorption kinetics and a pre-exponential factor of 1×10^{12} sec^{-1}.[1] From Table 1, it is observed the monolayer desorption energies agree within ~3 kJ/mol for the dendrites, linear dendrites, nanoparticles and HOPG samples. The monolayer desorption energy for the thin film, and high-density nanoparticles are higher than that of the other samples, calculated to be 58.6 and 57.0 kJ/mol, respectively. Furthermore, the 2nd layer energies range from 38.0 – 50.2 kJ/mol and increase with increasing TiO_2 material on the surface such that TiO_2 nanoparticles < linear dendrites < dendrites < high density nanoparticles.

Table 4.1. Calculated energies for the multilayer, 2nd layer and monolayer

Sample	2nd layer Energy (kJ/mol)	Monolayer Energy (kJ/mol)
TiO_2 thin film	N/A	58.6 ± 0.9
TiO_2 high density nanoparticles	50.2	57.0
TiO_2 dendrites	40.4	52.0
TiO_2 linear dendrites	39.8	49.0
TiO_2 nanoparticles	38.0 ± 0.05	51.3 ± 0.05
HOPG	N/A	50.0 ± 0.05

4.3.4 *Coverage-dependent desorption energy*

Considering the coverage dependence of the monolayer and 2nd layer, the Inversion method[26] was used to obtain the desorption energy as a function of the coverage for all of the different surfaces. From the Polanyi-Winger equation (Equation 1), the coverage-dependent E_{des}

(θ) can be determined by mathematical inversion, assuming first order desorption kinetics, where $-d\theta/dt$ is the desorption rate, v is the pre-exponential factor, and θ is the instantaneous coverage[26].

$$E_{des}(\theta) = -RT \ln\left[\frac{-d\theta/dt}{v\theta}\right] \quad (1)$$

The coverage-dependent desorption energies were calculated by first obtaining values for the initial coverages per given exposure. Since the present TiO_2 samples are not well defined surfaces in which monolayer saturation is explicitly observed, initial coverages were calculated assuming one monolayer equals 5.4×10^{14} molec/cm^2 based on that of TiO_2 (110).[5] Each desorption spectra was then integrated over all temperatures to determine θ and then Equation 1 was applied, as described by Kay *et al*[26]. Figure 4.5a-c shows the coverage-dependent energy profiles as a function of the coverage for D_2O desorption on each of the different surfaces at three different initial coverages (0.08, 0.5 and 1.0 ML). Here we are assuming a pre-exponential factor of 1×10^{12} sec^{-1} for consistency with calculated energies from Table 1 and previous studies.[1]

From Figure 4.5, the different peaks shown in the TPD spectra (Figure 4.3) correspond to plateau regions of the energy curves. In general, the first portion of the energy curve encompasses the range of the monolayer peaks. At very low coverages, it is observed that the desorption energy is very high and quickly begins to level; attributed to point defects on the surface.[26] For the surfaces that yielded 2nd layer peaks in the D_2O desorption spectra, the energy decreases as the coverage further increases. This is the case for the dendrites (red curve), linear dendrites (green curve) and nanoparticles (gold curve) (2nd layer regions highlighted in gray).

The final drop in energy, to where the energy plateaus, is associated with the coverage-independent multilayer region.[26]

When comparing the energy curves of the three different initial coverages, it is seen that as initial coverage increases from 0.08 → 1.0 ML (4. 5a to 4.5c) the energy difference between the HOPG, nanoparticle, linear dendrites and dendrite sample converges for the 2nd layer and monolayer state. This observation is most pronounced in Figure 4.5a where the energy increases such that: HOPG ≤ nanoparticles < linear dendrites < dendrites < high-density nanoparticles < thin film. Similarly, the 2nd layer energies of Figure 4.5a proceed as nanoparticles < linear dendrites < dendrites < high-density nanoparticles. In contrast, based on Figure 4.5c, it is difficult to construct a significant trend in the energy as majority of the curves overlay between 0 and 0.5 ML. Additionally, the energy of the high-density nanoparticles more closely resembles that of the thin film, where both energy curves clearly stand out from the other four samples.

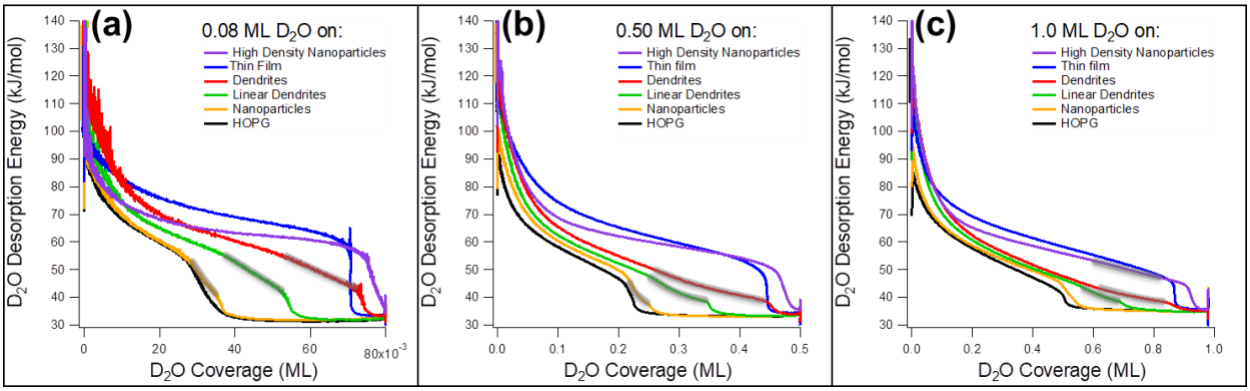

Figure 4.5. Coverage dependent energy curves for initial coverages of (a) 0.08, (b) 0.5 and (c) 1.0 MLs corresponding to exposures of 4.2×10^{14}, 2.5×10^{14} and 5.1×10^{14} molec/cm^2, respectively. 2nd layer energy regions are highlighted in gray.

4.3.5 *Isotope Analysis*

For each sample, mass/charge (m/z) ratios of 18, 19 and 20 were followed during the TPD experiments. In order to determine the relative amount of hydroxyl groups present on the surface, the percent (%) HOD^+ was calculated using Equation 2, where A_{18}, A_{19}, and A_{20} are the integrated areas of the m/z 18, 19 and 20 desorption spectra, respectively.

$$\frac{A_{19}}{\sum(A_{18}A_{19}A_{20})} \times 100 \quad (2)$$

The % HOD^+ versus exposure ($\times 10^{14}$ molec/cm^2) for the five different samples is shown in Figure 4.6.

From Figure 4.6, it is observed for all samples the % HOD^+ is initially high and decreases with increasing exposure and plateaus at high exposures. This decrease in the % HOD^+ suggests that the hydroxyls on the surface are being titrated by D_2O. At high exposures H-D exchange is ceased and the resulting % HOD^+ corresponds to H-D that may occur in the dosing lines and is irrespective of the surface.

In general, the % HOD^+ for the dendrites (red points), linear dendrites (green points), nanoparticles (gold points) and HOPG (black points) are indistinguishable. However, the % HOD^+ for the high-density nanoparticles (purple points) and thin film (blue points) is clearly greater than the other samples at low exposures but converges with the other samples at high exposures. This indicates that the TiO_2 high-density nanoparticles and thin film sample have a greater number of hydroxyl species initially when compared to the other samples.

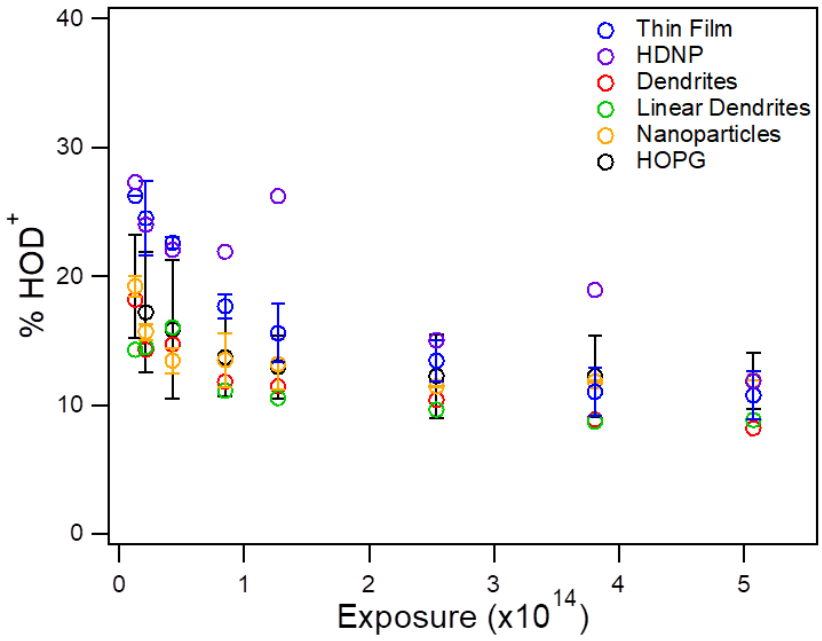

Figure 4.6. % HOD^+ vs. exposure ($\times 10^{14}$ molec/cm^2)

4.4 Discussion

The TPD spectra of Figure 4.3 clearly show that changes in the TiO_2 morphology (Figure 4.1) leads to pronounced changes in the desorption of D_2O. The most notable differences between the five TiO_2 structures analyzed are as follows: the 2nd layer (O anion sites) is not observed on the thin film, the 2nd layer shifts towards lower temperatures as the amount of TiO_2 morphology decreases (i.e. high to low: high-density nanoparticles > dendrites > linear dendrites > nanoparticles) and the relative second layer intensity decreases as the amount of TiO_2 material decreases on the HOPG surface. Furthermore, monolayer D_2O is more strongly bound on the surface of the thin film compared to the other TiO_2 samples and a tail on the high temperature side of the monolayer peak is present in thin film and high-density nanoparticle spectra.

Second layer water, i.e. water that is molecularly adsorbed on O anion sites, has been shown to desorb in a single peak between 160 K and 180 K on Rutile (110) that saturates at an

exposure of ~ 1.3 × 10^{15} molecules/cm^2.[5] Similarly, second layer water is observed on TiO_2 (100), however due to the shortened distance between a water molecule adsorbed at a Ti^{4+} site and the O^{2-} adsorption site (2.8 Å compared to 3.2 Å for the TiO_2 [110] surface), the TiO_2 (100) surface is more active for water dissociation which, in turn, reduces the population of water hydrogen bonded to O anion sites.[6,27] From Figure 4.3, D_2O bound to O^{2-} sites of TiO_2 is realized by a peak that desorbs roughly between 160 K and 200 K for the dendrites, linear dendrites, high-density nanoparticles and nanoparticles (Figures 4.3b, 4.3c, 4.3d and 4.3e, respectively). For each respective TPD spectrum, the second layer shifts toward lower temperature with increasing exposure for all occurrences; consistent with that of water TiO_2 (110).[1,5,6] Figure 4.4a more clearly demonstrates the shift of the second layer peak between samples such that, as the TiO_2 structures become more ordered (Figure 4.1a-d) the peak shifts to lower temperature. However, the second layer of the high-density nanoparticles is shifted to higher temperature (~200 K) compared to other samples. This shift is best explained by the crystallinity of the high-density nanoparticles (mixed rutile and anatase phase determined from TEM diffraction) coupled with the added adsorption sites due to the increase TiO_2 surface area. Water populates the Ti cation sites first followed by the O-anion sites on the TiO_2 as also described in previous work.[1,5,6,12,24] This not only explains the later appearance of the 2^{nd} layer state but also since the 2^{nd} layer peak is not fully developed, a complete shift to its saturation point is yet to be observed in the present work. Based on our calculations (Table 1), an energy change of ~ 12 kJ/mol is exhibited between the second layer of the nanoparticle sample to that of the high-density nanoparticles. It is interesting to note that the peak temperatures of the 2^{nd} layer for the high-density nanoparticles and nanoparticles do not coincide as one might expect. We speculate that this may be in part due to the small amount of TiO_2 in the nanoparticle sample such that, the

observed second layer may be a different adsorption site due to defects on the HOPG surface, but more careful analyses are needed for conformation. In comparing the SEM images of Figure 4.1b, 4.1c and 4.1d with the respective desorption spectra of Figure 4.3 (b, c and e), the disordered, branched structure of the dendrites may provide O-anion desorption sites that reside close enough to each other such that the binding of D_2O to these sites may exhibit a greater degree of coordination or stronger hydrogen bonded networks that explains the slight increase in the adsorption energy. Similarly, the close proximity of the individual crystalline nanoparticles of the high-density nanoparticles could facilitate hydrogen bonding of D_2O to O-anion sites resulting in the higher energy desorption state. An additional observation of the second layer peaks (*ii*) of Figure 4.3b-e, is that there is no explicit saturation of the peak as is the case for water on single crystal TiO_2. We owe this lack of saturation to the inherent complexity of supported TiO_2 heterostructures, in that the amount of possible adsorption sites differs greatly compared to a TPD study of water on a well-defined, homogenous TiO_2 crystal.

Interestingly, no second layer desorption state was present for the thin film sample (Figure 4.3a). It has been reported that, when water is strongly bound to a surface, bilayer formation is inhibited[27]. Specifically is the case for metal oxides in which the cation sites are available to bind water; though single crystal TiO_2 (rutile and anatase) seems to be an exception to this rule.[5,7,12] Based on our energy calculations, it is clear that the D_2O monolayer desorption state on the thin film surface is ~ 7-10 kJ/mol higher than the activation energies of desorption for all of the other TiO_2 samples with the exception of the high-density nanoparticles, in which it compares quite well (Table 1). Thus, for the present case of D_2O on the thin film (Figure 4.3a) we suggest that the higher water binding energy in the thin film may prevent 2nd layer formation. Another possible explanation for the broad monolayer peak and downward shift in temperature,

is that there exists a distribution of desorption states for which a second layer peak may be unresolvable. Furthermore, an additional explanation is that due to the amorphous nature of the thin film, there are simply no O anion sites available to bind D_2O. However, a more in-depth analysis of the surface is needed for this justification. Such information could be obtained from a High Resolution Electron Energy Loss (HREELS) experiment.

The monolayer desorption state for the thin film TPD spectrum (peak *i* from Figure 4.3a) is the result of D_2O bound to the Ti^{4+} sites. It has been widely reported that monolayer water desorption on TiO_2 (110) occurs at a peak temperature of 270-275 K[1,5,6] and is shifted to ~250 K for TiO_2 (100).[23] Water on anatase (101) similarly yields monolayer desorption at ~250 K.[12] Water on rutile powder yielded three major peaks: the first of which was a poorly resolved doublet centered at ~210 K that was assigned as a mixed multilayer and monolayer state. The second was a peak at ~310 was assigned to an additional molecularly adsorbed H_2O state and the third was a high temperature species at 568 K that was due to the reaction of water with hydroxyl species[28]. In comparison to literature, TiO_2 thin film desorption spectrum of Figure 4.3a agrees best with water desorption on the 1×3 surface of TiO_2 (100), the exception being the absence of the O-anion peak as previously stated.

When compared to the monolayer peak of the thin film, that of the high-density nanoparticles (peak *i* from Figure 4.3d) is narrower as well as shifted to lower temperature (as illustrated in Figure 4.4b). This is again best explained by the crystallinity of the high-density nanoparticles which exhibits more discrete adsorption sites as opposed to an array of adsorption sites that likely exist in a non-uniform film. This is fortified by the results of the coverage dependent energy analysis (Figure 4.5), in which the slope of monolayer energy region for the thin film curves is clearly steeper than that of the high-density nanoparticles for all initial

coverages. A greater slope corresponds to a greater degree of coverage dependence of the energy, explained by a distribution of desorption sites. Furthermore, the peak temperature range for the high-density nanoparticles ~290-240 K which compares well with both monolayer water desorption from anatase (101) (~250 K)[12] and rutile (110) (~270 K).[1,5] In comparison to the other TiO_2 samples, the TPD spectrum of the high-density nanoparticles (Figure 4.3d) is comparable to both the dendrite TPD spectrum (Figure 4.3b) and the thin film TPD spectrum (Figure 4.3a). The monolayer peak temperatures of the high-density nanoparticles more closely align with those of the thin film (Figure 4.4b) however, presence, position and relative intensity of the of the 2nd layer peak more closely resembles the dendrite TPD spectrum (Figure 4.3b).

The monolayer desorption state of the dendrites, linear dendrites, nanoparticles show little change in the desorption peak temperatures over all exposures. From Figure 4.4b, it is seen that monolayer desorption for these three samples begins at ~290 K and shifts to ~210 K with increasing exposure. In addition, the energy values obtained in Table 1 for the dendrites, linear dendrites and nanoparticles are consistent within 3 kJ/mol. However, from the coverage dependent energy analysis for low initial coverage (Figure 4.5a) there is clear separation of the energy curves and a distinct trend in the desorption energy of the monolayer region between samples such that the monolayer energy increases with increasing TiO_2 material on the surface (nanoparticles < linear dendrites < dendrites < high density nanoparticles < thin film). When the initial coverage increases to 0.5 ML and further to 1.0 ML (Figure 4.5b and c, respectively), the energy curves converge and become consistent with the energy values calculated in Table 1 (between 50-60 kJ/mol). This indicates that D_2O desorption on different TiO_2 surfaces is most susceptible to changes at low exposures. At higher exposures (i.e. higher initial coverages, Figure 4.5c), the convergence of the energy curves over the monolayer region suggests that

different D_2O adsorption sites from both the underlying HOPG and the TiO_2 structures on the surface cannot be resolved and instead result in a single broad desorption feature given in Figure 4.3b-d. Furthermore, the monolayer energy region for the TiO_2 nanoparticle sample and HOPG sample give energy curves that nearly perfectly overlap. This suggests that there is not enough TiO_2 material on the nanoparticle sample to differentiate between the nanoparticle monolayer and HOPG monolayer even at low exposures.

4.5 Conclusion

We have performed water (D_2O) desorption experiments on five different TiO_2 heterostructures supported on HOPG; including a TiO_2 thin film, dendrites, linear dendrites, nanoparticles and high-density nanoparticles. The results of the TPD analysis showed distinct differences in the desorption spectra with varying TiO_2 morphology. Complex TiO_2 structures such as the dendrites and linear dendrites samples show pronounced peaks associated with water bound to O-anion sites therefore the branched structures may facilitate hydrogen bonding of water between these sites of close proximity. However, water desorption from the TiO_2 thin film did not display a 2^{nd} layer desorption state which may be associated with the high activation energy for desorption (58.6 kJ/mol) that may inhibit the formation of 2^{nd} layer water. When the TiO_2 material becomes crystalline as in the case of the high-density nanoparticles, the desorption behavior is clearly different from that of the non-crystalline TiO_2 samples with a high monolayer desorption energy (57 kJ/mol) and a high energy 2^{nd} layer peak that only becomes pronounced at high exposures.

Historically, majority of TiO_2 water desorption studies have been performed on single crystals and powders. Single crystals are non-representative of industrial catalysts and powders

are complex and difficult to study. Up to this point, there have been no studies that consider the effect on TiO_2 morphology on the water desorption behavior. Precisely controllable TiO_2 heterostructures supported on HOPG offer a unique way to investigate these effects and serve to bridge the existing complexity gap between industrial relevant TiO_2 surfaces and single crystals.

4.6 References

1. Hugenschmidt, M. B., Gamble, L. & Campbell, C. T. The interaction of H2O with a TiO2(110) surface. *Surf. Sci.* **302,** 329–340 (1994).
2. Henderson, M. A. A surface science perspective on TiO2 photocatalysis. *Surf. Sci. Rep.* **66,** 185–297 (2011).
3. Diebold, U. The surface science of titanium dioxide. *Surf. Sci. Rep.* **48,** 53–229 (2003).
4. Gupta, S. M. & Tripathi, M. A review of TiO2 nanoparticles. *Chinese Sci. Bull.* **56,** 1639–1657 (2011).
5. Henderson, M. A. An HREELS and TPD study of water on TiO2(110): the extent of molecular versus dissociative adsorption. *Surf. Sci.* **355,** 151–166 (1996).
6. Henderson, M. A. Structural Sensitivity in the Dissociation of Water on TiO 2 Single-Crystal Surfaces. *Langmuir* **12,** 5093–5098 (1996).
7. Brinkley, D. *et al.* A modulated molecular beam study of the extent of H2O dissociation on TiO2(110). *Surf. Sci.* **395,** 292–306 (1998).
8. Brookes, I. M., Muryn, C. A. & Thornton, G. Imaging Water Dissociation on TiO2 (110). *Phys. Rev. Lett.* **87,** 266103 (2001).
9. Zhang, C. & Lindan, P. J. D. Multilayer water adsorption on rutile TiO2(110): A first-principles study. *J. Chem. Phys.* **118,** 4620–4630 (2003).

10. Beck, D. D., White, J. M. & Ratcliffe, C. T. Catalytic reduction of carbon monoxide with hydrogen sulfide. 2. Adsorption of water and hydrogen sulfide on anatase and rutile. *J. Phys. Chem.* **90,** 3123–3131 (1986).

11. Suda, Y. & Morimoto, T. Molecularly adsorbed water on the bare surface of titania (rutile). *Langmuir* **3,** 786–788 (1987).

12. Herman, G. S., Dohnálek, Z., Ruzycki, N. & Diebold, U. Experimental Investigation of the Interaction of Water and Methanol with Anatase−TiO 2 (101). *J. Phys. Chem. B* **107,** 2788–2795 (2003).

13. Kurtz, R. L. *et al.* Synchrotron radiation studies of H2O adsorption on TiO2(110). *Surf. Sci.* **218,** 178–200 (1989).

14. Smith, R. S., Li, Z., Dohnálek, Z. & Kay, B. D. Adsorption, Desorption, and Displacement Kinetics of H 2 O and CO 2 on Forsterite, Mg 2 SiO 4 (011). *J. Phys. Chem. C* **118,** 29091–29100 (2014).

15. Hammer, B., Wendt, S. & Besenbacher, F. Water adsorption on TiO2. *Top. Catal.* **53,** 423–430 (2010).

16. Pan, J. -M., Maschhoff, B. L., Diebold, U. & Madey, T. E. Interaction of water, oxygen, and hydrogen with TiO $_2$ (110) surfaces having different defect densities. *J. Vac. Sci. Technol. A Vacuum, Surfaces, Film.* **10,** 2470–2476 (1992).

17. Wang, L. Q., Baer, D. R., Engelhard, M. H. & Shultz, A. N. The Adsorption of Liquid and Vapor Water on TiO2 (110) Surfaces: the Role of Defects. *Surf. Sci.* **344,** 237–250 (1995).

18. Freund, H.-J. *et al.* Bridging the pressure and materials gaps between catalysis and surface science: clean and modified oxide surfaces. *Top. Catal.* **15,** 201–209 (2001).

19. Centi, G. *et al.* Oxide thin films based on ordered arrays of 1D nanostructure. A possible

approach toward bridging material gap in catalysis. *Phys. Chem. Chem. Phys.* **9,** 4930 (2007).

20. Ampelli, C. *et al.* Synthesis of TiO2 Thin Films: Relationship Between Preparation Conditions and Nanostructure. *Top. Catal.* **50,** 133–144 (2008).
21. Taing, J., Cheng, M. H. & Hemminger, J. C. Photodeposition of Ag or Pt onto TiO 2 Nanoparticles Decorated on Step Edges of HOPG. *ACS Nano* **5,** 6325–6333 (2011).
22. Grimm, R. L., Tobias, D. J. & Hemminger, J. C. D2O water interaction with textured carboxylic acid-terminated monolayer surfaces characterized by temperature-programmed desorption and molecular dynamics. *J. Phys. Chem. C* **114,** 1570–1579 (2010).
23. Henderson, M. a. The influence of oxide surface structure on adsorbate chemistry: desorption of water from the smooth, the microfaceted and the ion sputtered surfaces of TiO2(100). *Surf. Sci.* **319,** 315–328 (1994).
24. Henderson, M. A. The influence of oxide surface structure on adsorbate chemistry: desorption of water from the smooth, the microfaceted and the ion sputtered surfaces of TiO2(100). *Surf. Sci.* **319,** 315–328 (1994).
25. Redhead, P. P. a. Thermal desorption of gases. *Vacuum* **12,** 203–211 (1962).
26. Tait, S. L., Dohnálek, Z., Campbell, C. T. & Kay, B. D. n-alkanes on MgO(100). I. Coverage-dependent desorption kinetics of n-butane. *J. Chem. Phys.* **122,** 164707 (2005).
27. Henderson, M. The interaction of water with solid surfaces: fundamental aspects revisited. *Surf. Sci. Rep.* **46,** 1–308 (2002).
28. Beck, D. & White, J. Catalytic reduction of CO with hydrogen sulfide. 2. Adsorption of water and hydrogen sulfide on anatase and rutile. *Am. Chem. Soc.* **90,** 3123–3131 (1986).

CHAPTER 5

Insights into the selective photodeposition of Pt nanoparticles on TiO_2 nanoparticles supported on HOPG using TPD

5.1 Introduction

Platinum nanoparticles supported on TiO_2 is a system that has received considerable attention in recent years due to its relevance to catalysis and photocatalysis.[1] Platinum has been long recognized as one of the most active catalysts useful for numerous applications including the oxidation of CO[2,3], water gas shift reaction[4–7] and methanol oxidation.[8,9] In addition, loading Pt nanoparticles onto TiO_2 has proved useful for enhancing catalytic reactions such as the hydrogenation of alkenes and alkynes[10,11] and decomposition of carboxylic acids[12,13] and photocatalytic water splitting[14], among others.

It has been shown that Pt nanoparticles can be selectively photodeposited on the surface of TiO_2 nanoparticles using above-band gap radiation.[1] Preparing Pt/TiO_2 nanoparticles in this manner offers added control of the model catalyst system. Moreover, a recent study in the group has shown that the oxidation state of the photodeposited platinum (Pt [IV]) can be reduced to Pt (II) on the TiO_2 surface by photoreduction in a methanol/water solution.[15] Strong metal support interactions (SMSI) (i.e. oxidation of the active metal from the oxide support) that occur at high temperatures (>800 K) have been found to detract from the catalytic efficiency of supported nanomaterials, specifically Pt on TiO_2.[16–20] Thus, partial reduction (i.e. Pt[IV] → Pt [II]) using the photoreduction method allows for full reduction to Pt (0) by heating to occur at a lower temperature (>500 K), eliminating any potential SMSI.[15]

Since it is clear that Pt/TiO_2 systems are of great interest for water gas shift reactions, this chapter exploits water (D_2O) thermal desorption as a method to gain insight into the

photodeposition of Pt on the surface of TiO_2 nanoparticles supported on HOPG. To do so, a systematic approach was taken to first determine the water (D_2O) adsorption sites on the TiO_2 nanoparticles supported on HOPG followed by photodeposition (and partial photoreduction) of Pt on the TiO_2 sample. TPD was used with D_2O as a molecular probe to elucidate changes in the reactivity and adsorption characteristics of the model catalyst system. Lastly, CO desorption on Pt/TiO_2 will be briefly discussed.

5.2 Experimental

The TiO_2 nanoparticle samples was prepared by physical vapor deposition of Ti on an Ar plasma treated HOPG substrate (ZYB grade, MikroMasch) at 800 °C as described in Section 2.5.1. The resulting TiO_2 particles were found to be rutile phase TiO_2 by transmission electron microscopy (TEM) and x-ray absorption (XAS).[1] Selective Pt deposition onto the TiO_2 nanoparticles was accomplished by irradiation of the TiO_2/HOPG sample in a 1 μM aqueous K_2PtCl_4 (99.99% trace metal basis, Sigma Aldrich) mixed with HPLC grade water (Sigma Aldrich). To do so, the TiO_2/HOPG samples were mounted on an in-house constructed sample holder and exposed to a He UV source (365 nm) for up to 3 hours. A more detailed description of platinum photodeposition and photoreduction is presented in Ref[15]. Scanning electron microscopy (SEM) imaging was performed at the Laboratory for Electron and X-ray Instrumentation (LEXI) facility at University of California, Irvine. An SEM image of the Pt/TiO_2/HOPG sample is presented in Figure 5.1 in which no Pt deposition occurred on the underlying HOPG substrate.

TPD experiments were performed as described in Section 2.5.2 using D_2O (99.96%, Aldrich) and CO (Research grade, AirGas). Samples were heated to 700 K for 10 min prior to desorption experiments. A schematic of the experimental progression is shown in Figure 5.2.

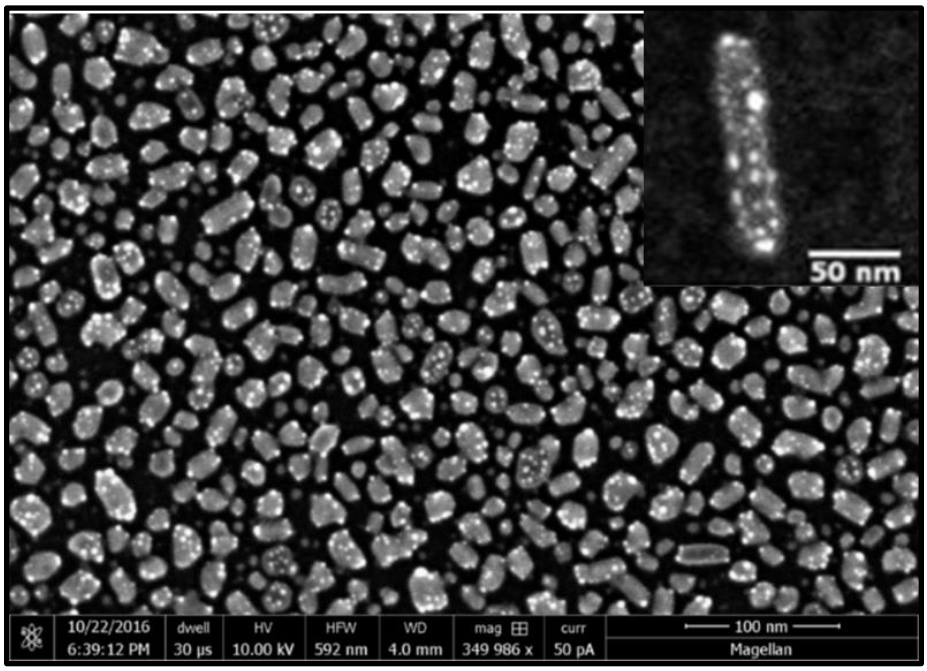

Figure 5.1. SEM image of Platinum nanoparticles selectively deposited on TiO_2 nanoparticles supported on HOPG resulting from a 3hr deposition. Pt (small bright spots) and TiO_2 nanoparticles are ~5 nm and ~20 nm, respectively.

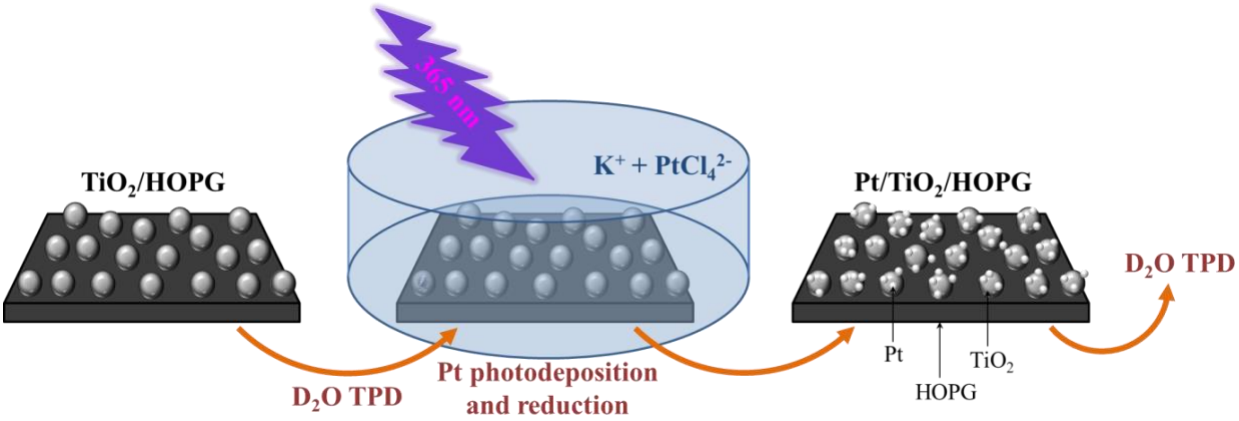

Figure 5.2. Schematic representation of the experimental procedure. D_2O TPD experiments were performed systematically; first on the TiO_2/HOPG and again after Pt deposition.

5.3 D_2O thermal desorption on TiO_2/HOPG vs. Pt/TiO_2/HOPG

Figure 5.3 presents the D_2O TPD spectra on (a) TiO_2/HOPG and (b) Pt/TiO_2HOPG. Each spectrum is comprised of D_2O exposures ranging from 3.6×10^{12} – 4.3×10^{14} molecules calculated using the gas flux through the 1 μm pinhole doser with a pressure of 1 torr behind the doser as described in Section 2.5.3.

In Figure 5.3a, 4 different desorption states are observed for D_2O adsorbed on the TiO_2/HOPG surface. First, at lower exposures, a peak that propagates at ~275 K and shifts to ~250 K is attributed to water (D_2O) desorption from Ti^{4+} sites on the TiO_2 particles. A small peak at low exposures is also observed at ~180 K and is the result of defects generated during O_2 plasma treatment prior to SEM imaging, which shall be discussed in more detail in Chapter 6. At higher exposures ($> 1.1 \times 10^{14}$ molecules) a new peak grows in at ~225 K and shifts to ~200 K. This peak is assigned to water (D_2O) hydrogen bonded to O^{2-} sites on the TiO_2 particles. Lastly, multilayer D_2O desorption is observed at 155 K. The desorption spectrum of Figure 5.3a is consistent with water desorption from singe crystal TiO_2.[21–26]

From Figure 5.3b, it is observed that D_2O desorption from the Pt/TiO_2/HOPG surface is much different than that of Figure 5.3a. In this case, only two peaks are observed; a broad peak that begins at ~275 K and shifts to ~205 K and the multilayer desorption state.

To further investigate the differences in the desorption spectra for D_2O on TiO_2/HOPG and Pt/TiO_2/HOPG (Figure 5.3a and 5.3b, respectively) an overlay of a low exposure (0.71×10^{14} molec) and high exposure (4.3×10^{14} molec) TPD trace are shown in Figure 5.4a and 5.4b, respectively.

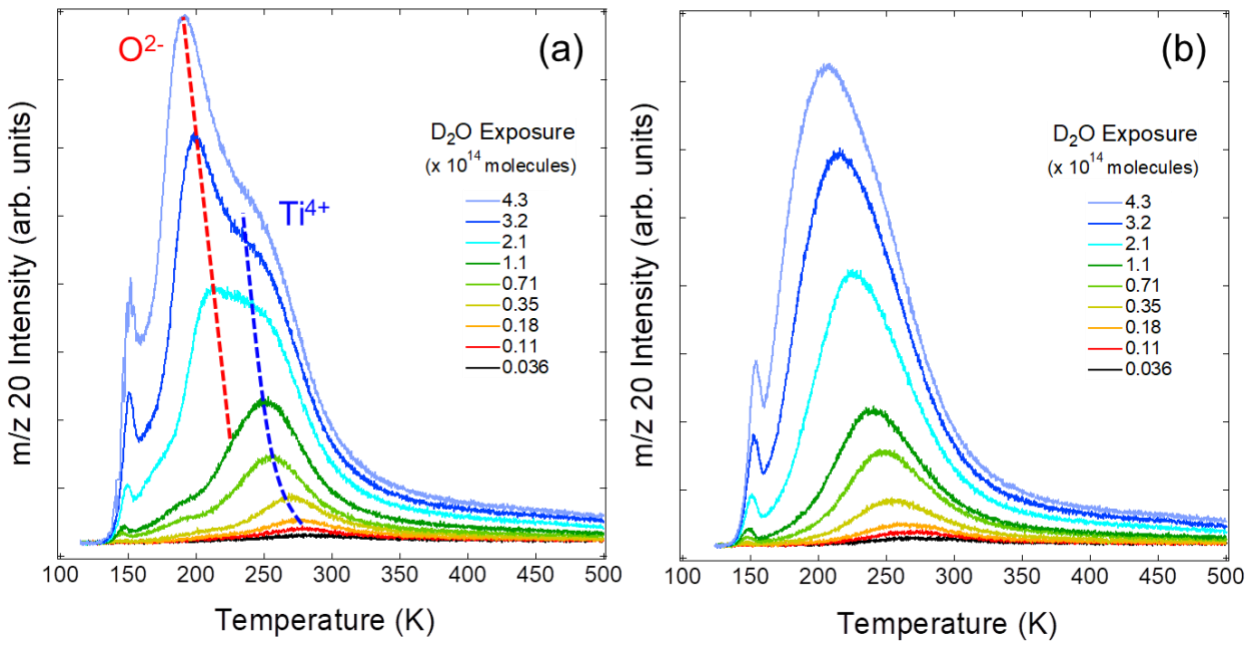

Figure 5.3. D_2O thermal desorption spectrum for (a) TiO_2 nanoparticles supported on HOPG and (b) Pt nanoparticles supported on TiO_2 nanoparticles on HOPG. The desorption state highlighted by the red dotted line (spectrum [a]) is assigned to D_2O adsorbed at O^{2-} sites on the TiO_2 and the blue dotted line is indicative of D_2O adsorbed at Ti^{4+} sites on the TiO_2 particles.

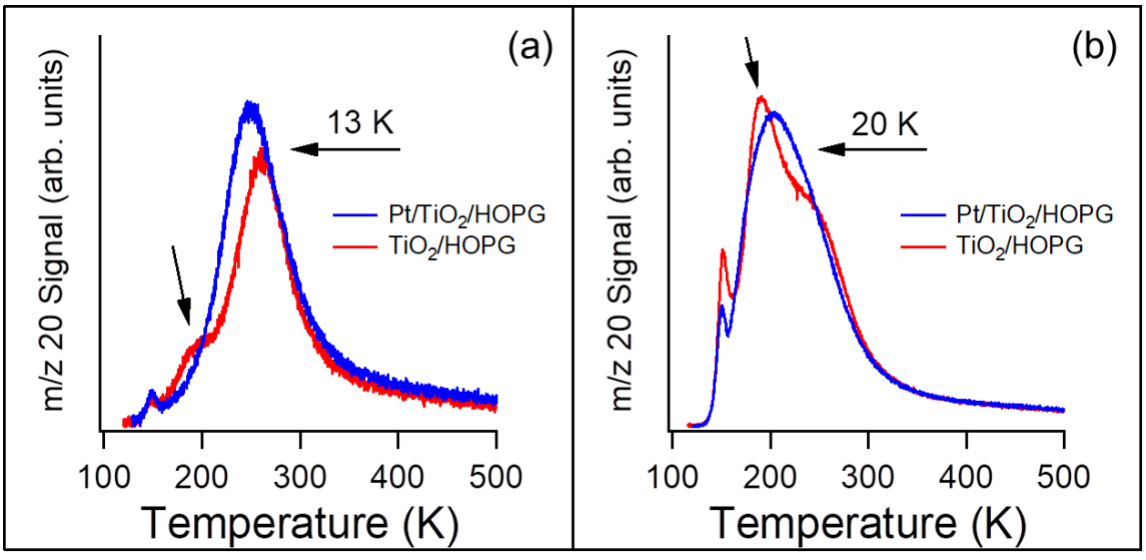

Figure 5.4. Overlay of D_2O TPD traces from TiO_2/HOPG and Pt/TiO_2/HOPG for (a) low exposure (0.71×10^{14} molecules) and (b) high exposure (4.3×10^{14} molecules). Plot (a) shows the disappearance of the defect peak and a ~13 K shift of the Ti^{4+} peak and plot (b) shows a reduction of the O^{2-} peak and a ~20 K shift of the Ti^{4+} peak.

From Figure 5.4, there are several distinct differences in the D_2O desorption profile after Pt has been deposited on the TiO_2 sample. First, from Figure 5.4a, we see a prominent shift in the Ti^{4+} desorption state of ~13 K, this shift is likely the result of added contribution from the Pt^0 sites in which D_2O monolayer desorption from Pt (111) occurs at ~215 K (Figure 5.5). This peak shift corresponds to a ~3 kJ/mol decrease in activation energy according to the Redhead equation[27] (assuming a frequency factor of 1×10^{13} sec^{-1}). In addition, the defect site generated during O_2 plasma treatment prior to SEM imaging is no longer observed. Two explanations for this occurrence could be that Pt is adsorbed on these defect sites on the TiO_2 or that the added D_2O desorption contribution from the Pt particles is overshadowing this state. For the high exposure spectral overlay (Figure 5.4b), the shift of the Ti^{4+} is now more pronounced (~20 K, ~4.8 kJ/mol) which would be expected given the Pt (111) TPD spectrum of Figure 5.5. Finally, the most interesting observation, is the reduction of the O-anion site for the TiO_2/HOPG after the addition of Pt nanoparticles on the TiO_2. This indicates that the Pt photodeposition occurs on the O^{2-} sites of the TiO_2 particles. Thus, coupled with previous experiments, it is suggested that the Pt deposition mechanism involves photogenerated holes on the TiO_2 surface that create hydroxyl radicals that subsequently adsorb platinum from solution in the form of Pt (IV).[15]

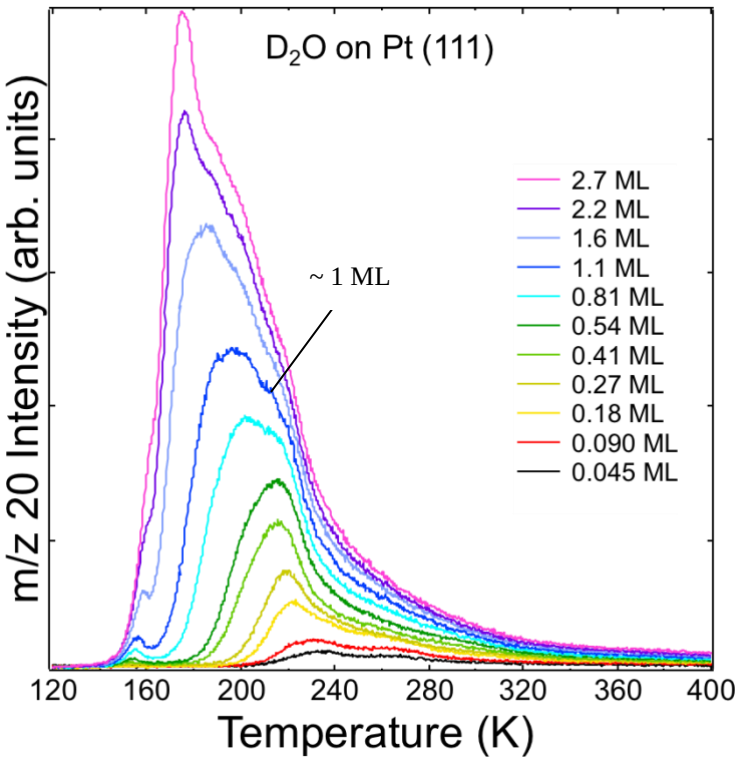

Figure 5.5. D_2O on Pt (111). Monolayer desorption occurs between 240 and 210 K. Coverages are in monolayers (ML).

5.4 CO adsorption on Pt/TiO_2/HOPG

With the interest of Pt supported on TiO_2 as water gas shift catalyst, the adsorption of CO on the Pt/TiO_2/HOPG is naturally of interest. In the present work, an attempt was made to observe CO desorption at room temperature, however, our efforts were unsuccessful. It is well known that CO adsorbs on the Pt (111) surface at room temperature.[28] An explanation into the lack of CO adsorption at room temperature could be due to the observation of water (m/z 18) desorption during the TPD experiment. It is likely that a small leak in the CO dosing line resulted in an impure CO exposure. If H_2O competes for the same adsorption sites, then perhaps this competition may have hindered the adsorption of CO. Furthermore, a more likely explanation lends itself to probable adventitious carbon contamination inhibiting CO adsorption at room

temperature. Since SMSI was a concern in the present study, relatively low temperatures (< 700 K) were used to (a) reduce the Pt from (IV) to (0) oxidation, and (b) perform TPD experiments. In doing so, it is likely adventitious carbon was still present on the Pt particles. However, given the support material used in this study was HOPG, adventitious carbon was unobservable via Auger electron spectroscopy (AES) and X-ray photoelectron spectroscopy (XPS) due to a high carbon background.

5.5 Conclusions and future work

Preparing a Pt/TiO_2 system as described in this chapter allows for better control of the catalyst material thus allowing for systematic investigations to be performed to gain a fundamental understanding of the properties of these model catalyst systems. The systematic TPD experiments performed herein are, to my knowledge, the first of their kind and an invaluable tool to gain more insight into supported catalysts. From the results of this study, it was determined that Pt photodeposited on the surface of TiO_2 nanoparticles reside on the O^{2-} sites. Undoubtedly more complementary investigations would be paramount to further develop an understanding of the reactivity of Pt/TiO_2/HOPG, including scanning tunneling microscopy (STM), high-resolution electron energy loss spectroscopy (HREELS) and infrared techniques.

Furthermore, given the limitations observed for CO desorption from Pt/TiO_2/HOPG, it is clear more studies are needed to better investigate CO adsorption. To do so, a mild Ar plasma treatment could be performed prior to CO TPD experiments to attempt to remove adventitious carbon thus promoting adsorption. In addition, different substrates to support the TiO_2 nanoparticles could also be explored to remove the high carbon background allowing for better surface characterization and observation of carbon contaminants.

5.6 References

1. Taing, J., Cheng, M. H. & Hemminger, J. C. Photodeposition of Ag or Pt onto TiO 2 Nanoparticles Decorated on Step Edges of HOPG. *ACS Nano* **5,** 6325–6333 (2011).
2. Porsgaard, S. *et al.* In Situ Study of CO Oxidation on HOPG-Supported Pt Nanoparticles. *ChemPhysChem* **14,** 1553–1557 (2013).
3. Solla-Gullón, J., Vidal-Iglesias, F. J., Herrero, E., Feliu, J. M. & Aldaz, A. CO monolayer oxidation on semi-spherical and preferentially oriented (100) and (111) platinum nanoparticles. *Electrochem. commun.* **8,** 189–194 (2006).
4. Grabow, L. C., Gokhale, A. A., Evans, S. T., Dumesic, J. A. & Mavrikakis, M. Mechanism of the water gas shift reaction on Pt: First principles and microkinetic modeling. *J. Phys. Chem. C* **112,** 4608–4617 (2008).
5. Rajesh, T., Rajarajan, A. K., Gopinath, C. S. & Devi, R. N. Evidence of Cationic Pt Active for Water–Gas Shift Reaction: Pt-Doped BaCeO3 Perovskite. *J. Phys. Chem. C* **116,** 9526–9532 (2012).
6. Royer, S. & Duprez, D. Catalytic Oxidation of Carbon Monoxide over Transition Metal Oxides. *ChemCatChem* **3,** 24–65 (2011).
7. Panagiotopoulou, P., Christodoulakis, A., Kondarides, D. I. & Boghosian, S. Particle size effects on the reducibility of titanium dioxide and its relation to the water–gas shift activity of Pt/TiO2 catalysts. *J. Catal.* **240,** 114–125 (2006).
8. Şen, F. & Gökağaç, G. Different Sized Platinum Nanoparticles Supported on Carbon: An XPS Study on These Methanol Oxidation Catalysts. *J. Phys. Chem. C* **111,** 5715–5720 (2007).

9. Xia, X. H., Iwasita, T., Ge, F. & Vielstich, W. Structural effects and reactivity in methanol oxidation on polycrystalline and single crystal platinum. *Electrochim. Acta* **41,** 711–718 (1996).

10. Matsuoka, M. *et al.* Photocatalysis for new energy production. *Catal. Today* **122,** 51–61 (2007).

11. Anpo, M., Aikawa, N. & Kubokawa, Y. Photocatalytic hydrogenation of alkynes and alkenes with water over titanium dioxide. Platinum loading effect on the primary processes. *J. Phys. Chem.* **88,** 3998–4000 (1984).

12. Gallezot, P., Laurain, N. & Isnard, P. Catalytic wet-air oxidation of carboxylic acids on carbon-supported platinum catalysts. *Appl. Catal. B Environ.* **9,** L11–L17 (1996).

13. Kraeutler, B. & Bard, A. J. Heterogeneous Photocatalytic Preparation of Supported Catalysts. Photodeposition of Platinum on TiO2 Powder and Other Substrates. *J. Am. Chem. Soc.* **100,** 4317–4318 (1978).

14. Kitano, M., Takeuchi, M., Matsuoka, M., Thomas, J. M. & Anpo, M. Photocatalytic water splitting using Pt-loaded visible light-responsive TiO2 thin film photocatalysts. *Catal. Today* **120,** 133–138 (2007).

15. Bruce, J. P., Babore, A. D., Galhenage, R. P., Hemminger, J. C. Photodeposition and control of Pt oxidation states on TiO2 nanoparticles supported on HOPG. *In Preparation.* (2018).

16. Somorjai, G. A. The surface science of heterogeneous catalysis. *Surf. Sci.* **299–300,** 849–866 (1994).

17. Tauster, S. J., Fung, S. C. & Garten, R. L. Strong Metal-Support Interactions - Group-8 Noble-Metals Supported on Tio2. *J. Am. Chem. Soc.* **100,** 170–175 (1978).

18. Tauster, S. J. & Fung, S. C. Strong Metal-Support Interactions - Occurrence among Binary Oxides of Groups Iia-Vb. *J. Catal.* **55,** 29–35 (1978).

19. Tauster, S. J., Fung, S. C., Baker, R. T. & Horsley, J. A. Strong interactions in supported-metal catalysts. *Science (80-.).* **211,** 1121–1125 (1981).

20. Tauster, S. J. STRONG METAL-SUPPORT INTERACTIONS. *Acc. Chem. Res.* **20,** 389–394 (1987).

21. Henderson, M. A. Structural Sensitivity in the Dissociation of Water on TiO 2 Single-Crystal Surfaces. *Langmuir* **12,** 5093–5098 (1996).

22. Henderson, M. A. An HREELS and TPD study of water on TiO2(110): the extent of molecular versus dissociative adsorption. *Surf. Sci.* **355,** 151–166 (1996).

23. Henderson, M. a. The influence of oxide surface structure on adsorbate chemistry: desorption of water from the smooth, the microfaceted and the ion sputtered surfaces of TiO2(100). *Surf. Sci.* **319,** 315–328 (1994).

24. Herman, G. S. *et al.* Experimental Investigation of the Interaction of Water and Methanol with Anatase−TiO 2 (101). *J. Phys. Chem. B* **107,** 2788–2795 (2003).

25. Brinkley, D. *et al.* A modulated molecular beam study of the extent of H2O dissociation on TiO2(110). *Surf. Sci.* **395,** 292–306 (1998).

26. Smith, R. S., Li, Z., Dohnálek, Z. & Kay, B. D. Adsorption, Desorption, and Displacement Kinetics of H 2 O and CO 2 on Forsterite, Mg 2 SiO 4 (011). *J. Phys. Chem. C* **118,** 29091–29100 (2014).

27. Redhead, P. Thermal desorption of gases. *Vacuum* **12,** 203–211 (1962).

28. Hopster, H. & Ibach, H. Adsorption of CO on Pt(111) and Pt 6(111) × (111) studied by high resolution electron energy loss spectroscopy and thermal desorption spectroscopy.

Surf. Sci. **77,** 109–117 (1978).

CHAPTER 6

Effect of surface treatment on D_2O desorption: oxygen and argon plasma

6.1 Introduction

Surface treatment by means of ion sputtering with inert gas (typically Argon) or with oxygen plasma is advantageous for many applications in surface science. For example, it is well known that metal surfaces can be bombarded with argon ions to effectively remove adventitious carbon and other contaminating species.[1] In addition, oxygen/argon plasma treatment has been shown to be useful for removing carbon contaminants from samples to obtain high quality scanning electron microscopy (SEM), transmission electron microscopy (TEM), and energy-dispersive x-ray spectroscopy (EDS) data.[2] Plasma cleaning has also been exploited to promote the adhesion of thin/thick films on substrate surfaces; such as polyethylene terephthalate on oxygen plasma treated silver.[3] Furthermore, plasma treatment techniques have been utilized for surface modification/functionalization of polymer surfaces.[4,5]

As previously mentioned, oxygen plasma cleaning prior to SEM imaging is typically necessary to obtain high resolution data. In the present work, TPD experiments were often performed after SEM imaging which led to the question of how does plasma treatment affect the adsorption behavior of D_2O. To answer this question, this chapter touches on three fundamental studies of plasma treatment effects: the effect of oxygen plasma treatment on the adsorption of D_2O on TiO_2 nanoparticles supported on HOPG, argon versus oxygen plasma treatment on the adsorption of D_2O on HOPG, and briefly, D_2O desorption from high density TiO_2 nanoparticles grown on HOPG prepared using oxygen plasma versus argon plasma .

6.2 Experimental

For the present chapter, the experimental progression is presented in Figure 6.1. Oxygen plasma treatment was done in the FEI Magellan XHR 400L SEM housed at the LEXI facility at the University of California, Irvine. Argon plasma treatment was performed in the TPD chamber via an ion gun using an argon pressure of 7.5×10^{-5} torr, 20 mA emission current, and 0.5 kV beam energy for 30 minutes. Titanium was evaporated on the pre-treated HOPG (9 nm, measured by a quartz crystal microbalance) at 800 ºC for 1.5 hours followed by annealing in the bell jar for an additional 2.5 hours post deposition. SEM imaging was performed at the LEXI facility. For TPD experimental procedure, please refer to Chapter 2.

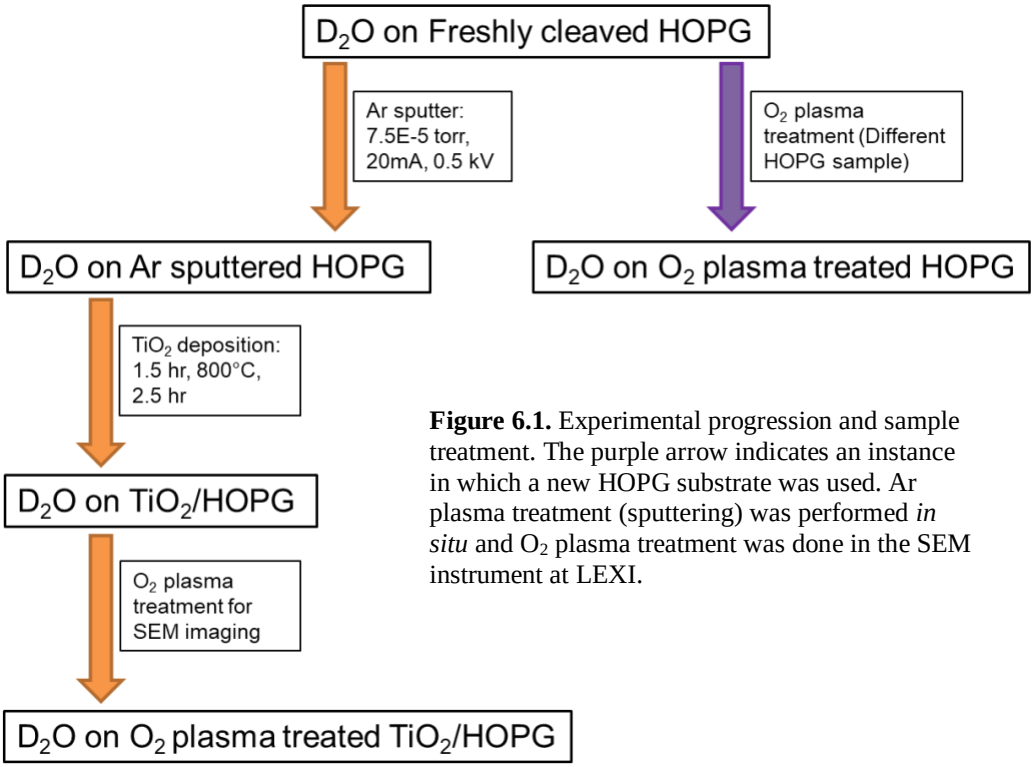

Figure 6.1. Experimental progression and sample treatment. The purple arrow indicates an instance in which a new HOPG substrate was used. Ar plasma treatment (sputtering) was performed *in situ* and O_2 plasma treatment was done in the SEM instrument at LEXI.

6.3 D_2O adsorption on argon sputtered versus oxygen plasma treated HOPG

To investigate the effect of inert versus reactive plasma (Ar vs O_2, respectively), TPD was used to observe D_2O desorption from a freshly cleaved piece of HOPG, Ar plasma treated HOPG and O_2 plasma treated HOPG. Figure 6.2 shows the TPD spectrum of D_2O adsorbed on the freshly cleaved HOPG surface. From Figure 6.2 we observe two desorption states, a high temperature peak that begins at ~250 K and shifts to ~200 K with increasing D_2O exposure (sec). This state is assigned to molecularly adsorbed D_2O bound to the surface at steps and point defects on the HOPG. The second peak at 162 K is due to D_2O multilayers and is consistent with previous work.[6,7]

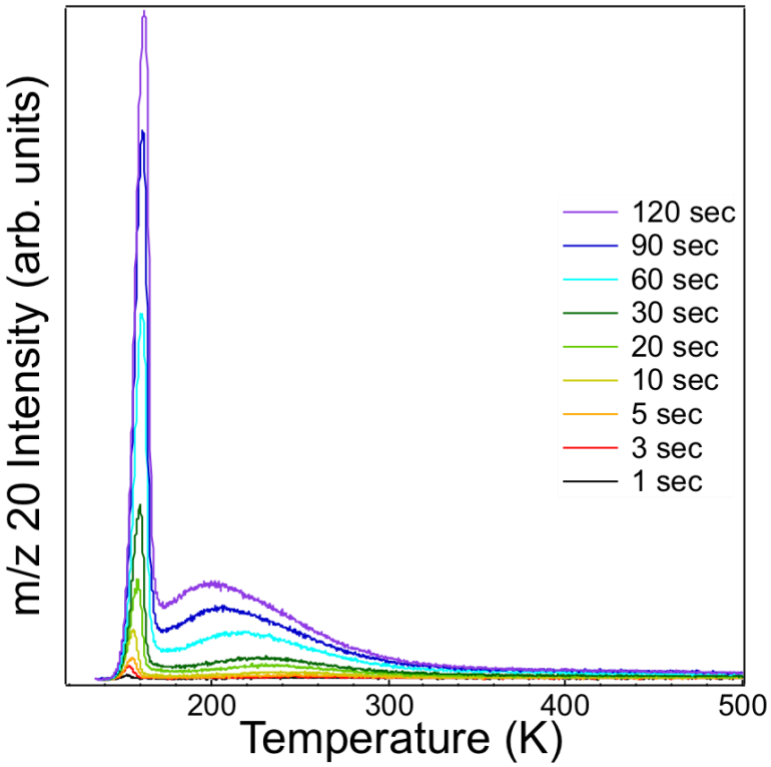

Figure 6.2. D_2O on freshly cleaved HOPG TPD spectrum (m/z 20 intensity vs temperature, K) Exposures are shown in units of seconds in which the pressure behind the 1 μm pinhole doser was 1.0 torr.

Figure 6.3 shows the D_2O thermal desorption spectrum from Ar plasma treated HOPG. In this case, an observed broadening and shift of the high temperature peak of Figure 6.2 indicates an increased distribution of defects induced by the Ar plasma as well as an increase in binding strength. Additionally, a shoulder on the high temperature of the multilayer suggests that roughening of the surface by argon bombardment is disrupting the lateral water (D_2O) diffusion and subsequent 3-dimensional clustering on the HOPG surface as expected for water on HOPG.[6] As a result this shoulder may be attributed to surface-influenced hydrogen bonding between D_2O molecules, further fortifying the observed shift toward lower temperature with increasing coverage indicative of surface coverage dependency. For a clearer comparison, Figure 6.4 shows the overlaid TPD spectra from Figures 6.2 and 6.3 for (a) low doses and (b) high exposures of D_2O.

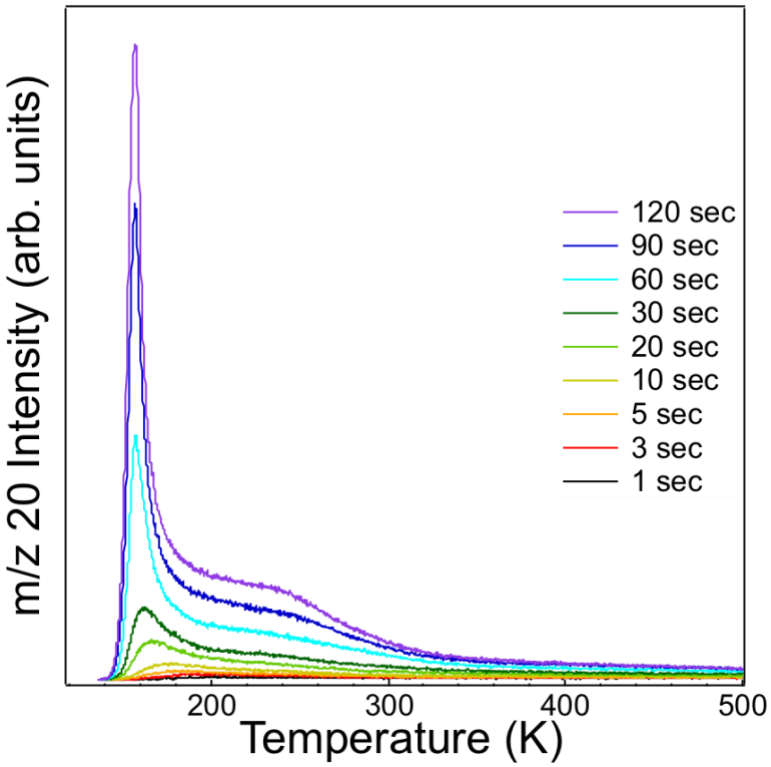

Figure 6.3. D_2O thermal desorption from Ar plasma treated HOPG. Exposures are shown in units of seconds in which the pressure behind the 1 μm pinhole doser was 1.0 torr.

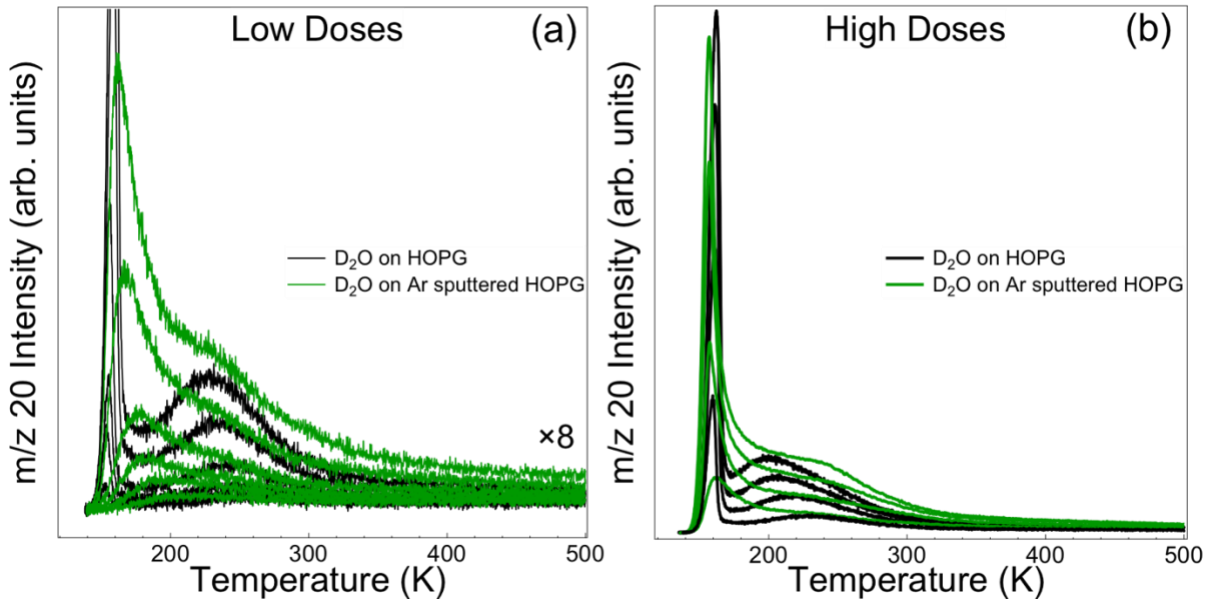

Figure 6.4. Overlaid TPD spectra for D_2O on freshly cleaved HOPG (black traces) versus D_2O on Ar sputtered HOPG (green traces). "Low doses" (1 – 20 sec exposure) are shown in plot (a) and "high doses" (30 – 120 sec exposure) are shown in plot (b).

When looking at the interaction of D_2O on O_2 plasma treated HOPG, the desorption behavior is noticeably different from Figure 6.5. A shift of the high temperature peak to even higher temperatures is observed when compared to D_2O/HOPG (Figure 6.6). This shift suggests an increase in the binding strength of D_2O at induced point defects generated from the O_2 plasma. In addition, a new peak becomes apparent at ~200 K and shifts to lower temperatures with increasing exposure. This peak is attributed to oxygen functionality that is introduced on the surface from the plasma treatment in which water (D_2O) can hydrogen bond.

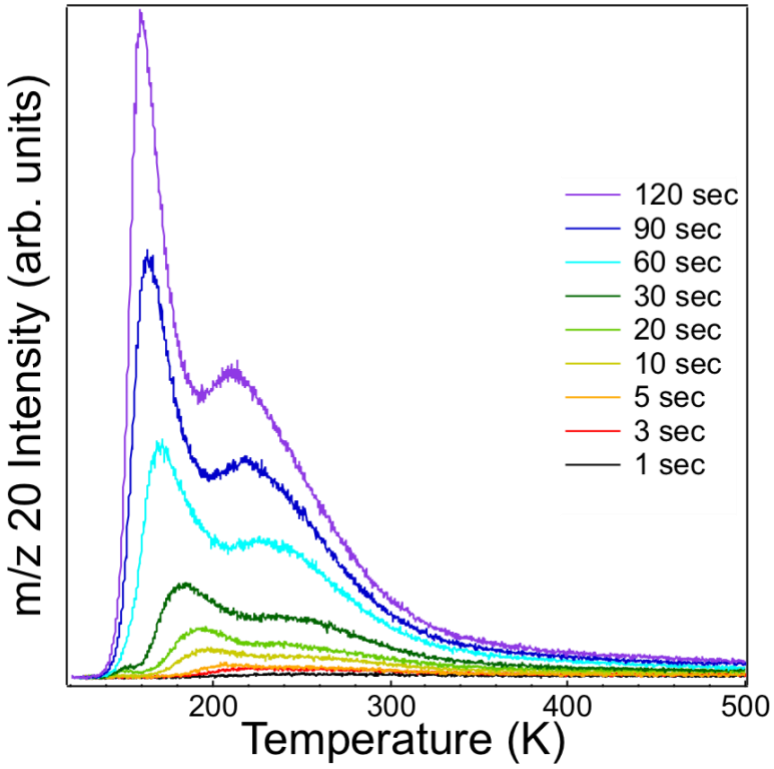

Figure 6.5. D_2O TPD spectrum from oxygen plasma treated HOPG. Exposures are shown in units of seconds in which the pressure behind the 1 μm pinhole doser was 1.0 torr.

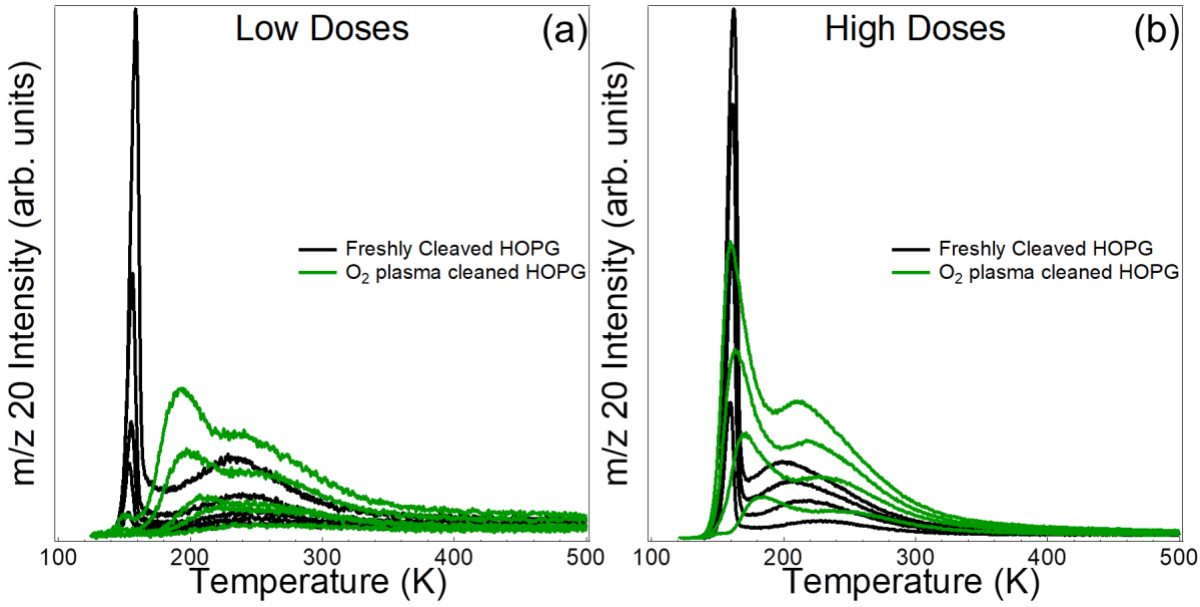

Figure 6.6. Overlaid TPD spectra for D_2O on freshly cleaved HOPG (black traces) versus D_2O on O_2 plasma treated HOPG (green traces). "Low doses" (1 – 20 sec exposure) are shown in plot (a) and "high doses" (30 – 120 sec exposure) are shown in plot (b).

To help justify the assignment of the 200 K peak of Figure 6.5, the other masses followed during the desorption experiments (m/z 18 and 19) can be used to evaluate the degree of isotopic exchange between D_2O and hydroxyls present on the surface. By calculating the %HOD (as described in Section 2.3.7) a qualitative view of the amount of hydroxyls present on the surface can be obtained. Figure 6.7 shows the %HOD calculated as a function of exposure (sec) for the three HOPG surfaces investigated in this study: freshly cleaved, Ar sputtered and O_2 plasma treated. From Figure 6.6 it is observed that the %HOD for all three HOPG samples exhibit similar behavior. In general, the %HOD (i.e. amount of surface hydroxyls) is initially high and then decreases with increasing exposure. This indicates that H-D exchange interactions are occurring such that:

$$OH_{(ad)} + D_2O_{(ad)} \rightarrow OD_{(ad)} + HOD_{(d)}$$

The drop in %HOD with increasing exposure is due to the surface hydroxyls being titrated thus reacting all of the $OH_{(ad)}$. Interestingly, there is a pronounced %HOD for low exposures of the oxygen plasma treated HOPG and to a lesser extent on the Ar plasma treated HOPG. This suggests that there is an enhancement of H-D exchange occurring thus a higher population of OH species on the surface, which can be attributed to the induced oxygen functionality from O_2 plasma treatment.

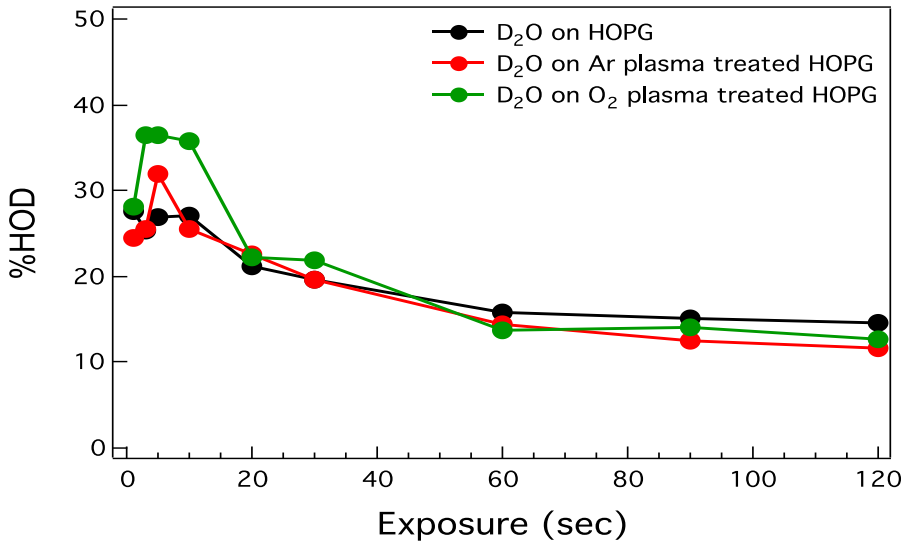

Figure 6.7. %HOD vs Exposure (sec) for freshly cleaved HOPG (black curve), Ar sputtered HOPG (red curve) and O_2 plasma treated HOPG (green curve).

6.4 D_2O adsorption on TiO_2/HOPG versus O_2 plasma treated TiO_2/HOPG

As previously mentioned, plasma treatment is often necessary to obtain high resolution SEM images, thus it is important to understand how plasma treatment affects the reactivity of surfaces. In this case, the post-Ar sputtered HOPG was used to prepare TiO_2 nanoparticles and analyzed using TPD with D_2O as a probe molecule. The D_2O on TiO_2/HOPG desorption spectrum is shown in Figure 6.8. From the figure, we see three major desorption states. The high temperature peak begins at ~270 K and shifts to 225 K with increasing exposure and is attributed to D_2O bound to Ti^{4+} sites. The second peak between 200 K and 165 K is assigned as water bound to O – anion sites on the surface and the low temperature peak is indicative of multilayer desorption. The D_2O desorption spectrum of Figure 6.8 is consistent with water desorption from single crystal TiO_2 (110).[8–10]

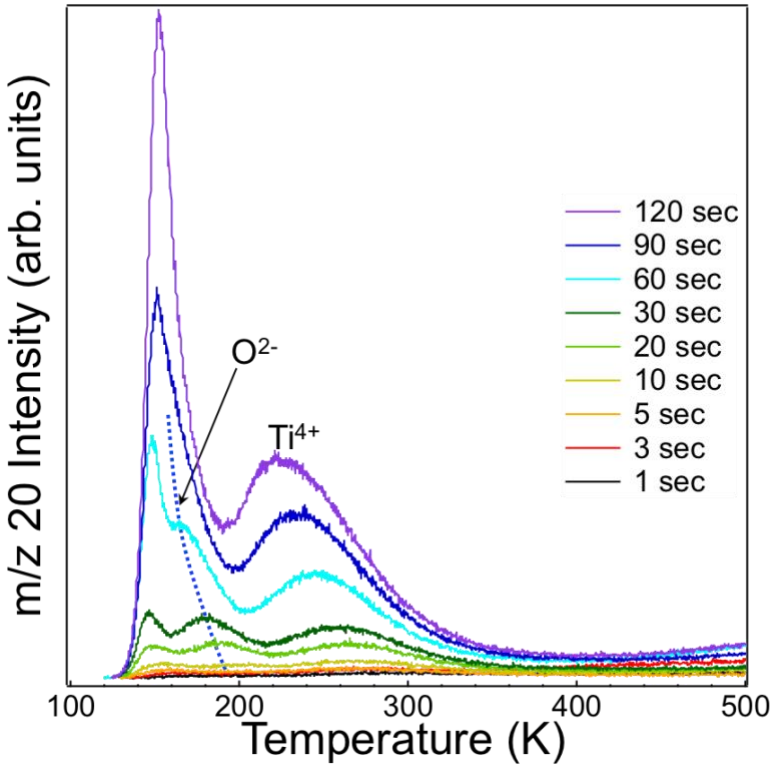

Figure 6.8. D_2O on TiO_2/HOPG TPD spectrum.

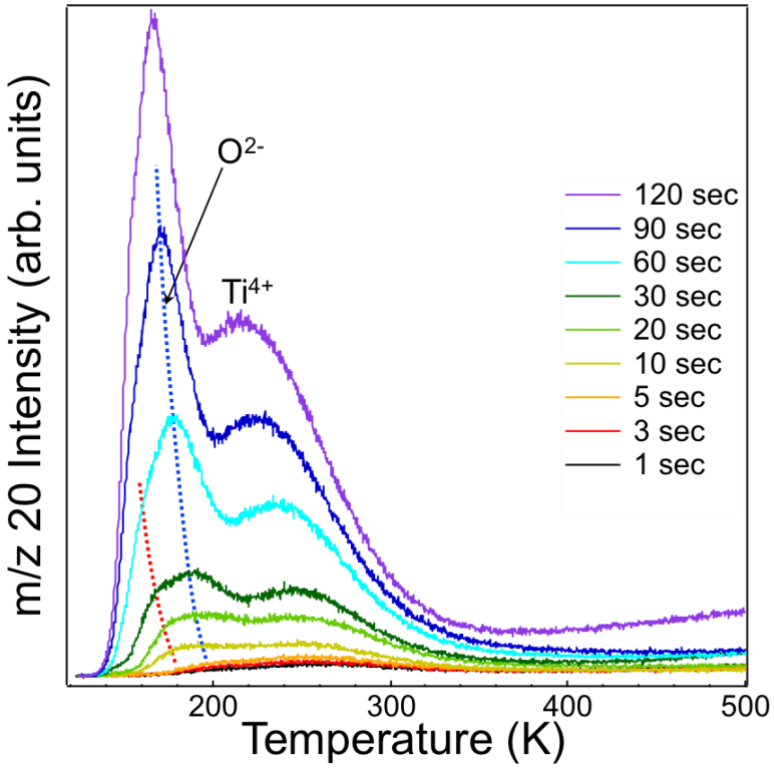

Figure 6.9. D_2O on O_2 plasma treated TiO_2/HOPG TPD spectrum

Figure 6.9 shows D_2O desorption from the same TiO_2 sample that has been O_2 plasma treated for SEM imaging. From the results of the TPD, it is clear that the desorption spectrum now exhibits some new features. For a better comparative look, Figure 6.10 shows the overlaid TPD spectra of D_2O on TiO_2/HOPG (Figure 6.8) and D_2O on O_2 plasma cleaned TiO_2/HOPG (Figure 6.9). From Figure 6.10, it is apparent that a new desorption feature appears on the low temperature side of the O – anion peak (between 200 K and 160 K) after plasma treatment. From Section 6.3 it was determined that O_2 plasma treatment introduced oxygen functionality onto the surface. In the case of O_2 plasma treated HOPG, it is suggested that the 160 K peak of Figure 6.9 (red dotted line) is also associated water (D_2O) hydrogen bound with oxygen species induced on the sample surface from the plasma cleaning. Another interesting observation from Figure 6.10 is the increase in intensity for both the O^{2-} and Ti^{4+} peaks. This occurrence could be due to the removal of adventitious carbon that may have been present before the plasma cleaning which would, in turn, create more D_2O adsorption sites on the TiO_2 nanoparticle surface. Furthermore, though it is clear that the O_2 plasma cleaning affects the desorption of D_2O on the TiO_2/HOPG system, it is interesting to note that there is no introduction of defects that promote dissociative adsorption of D_2O, as was observed for Ar sputtered TiO_2 (110) preheated to 700 K.[10] Clearly there exist differences in the choice of plasma, as demonstrated in Section 6.3; however, it is suggested that the O_2 plasma treatment in the present study may be mild enough as to not induce defects that facilitate dissociative water adsorption, though it certainly alters the surface reactivity and adsorption behavior of D_2O.

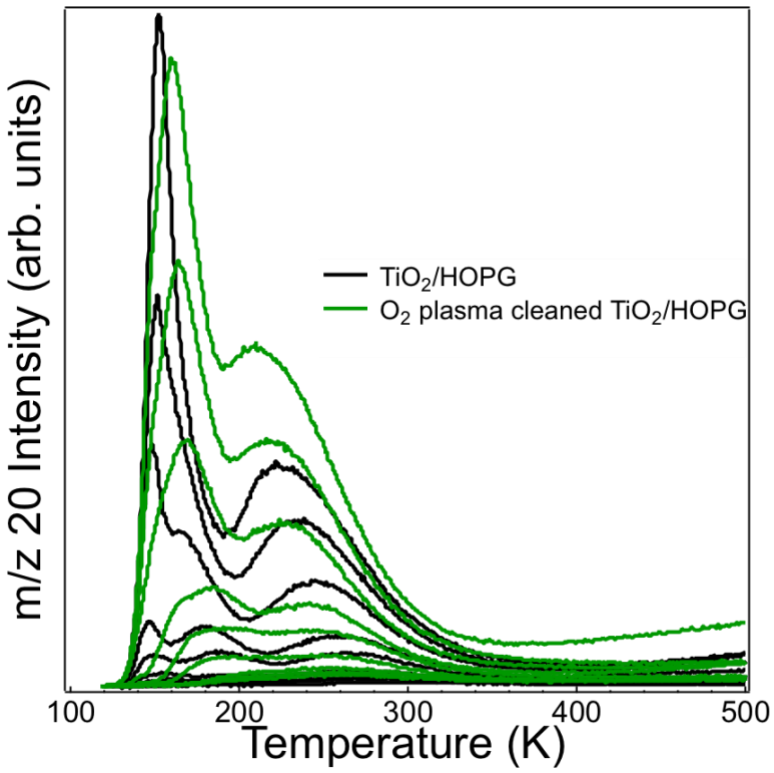

Figure 6.10. TPD spectral overlay for D_2O on TiO_2/HOPG before O_2 plasma treatment (black curves) and after O_2 plasma treated (green curves).

6.5 Effect of Ar vs O_2 plasma on TiO_2 nanoparticle deposition

One important fundamental question regarding the preparation of TiO_2 nanoparticles supported on HOPG is the effect of the surface pre-treatment on the resulting sample. As demonstrated in Section 6.3, O_2 plasma results in oxygen species formed on the HOPG surface, whereas Ar plasma only alters the surface by physical bombardment. To gain insight into this effect, two different TiO_2 nanoparticle samples were analyzed using TPD with D_2O to probe the reactivity of the surface. Figure 6.11 shows SEM images of the two TiO_2 nanoparticle samples: the first prepared by pretreating the HOPG substrate with Ar plasma (Figure 6.11a) and the second prepared using O_2 plasma treatment (Figure 6.11b).

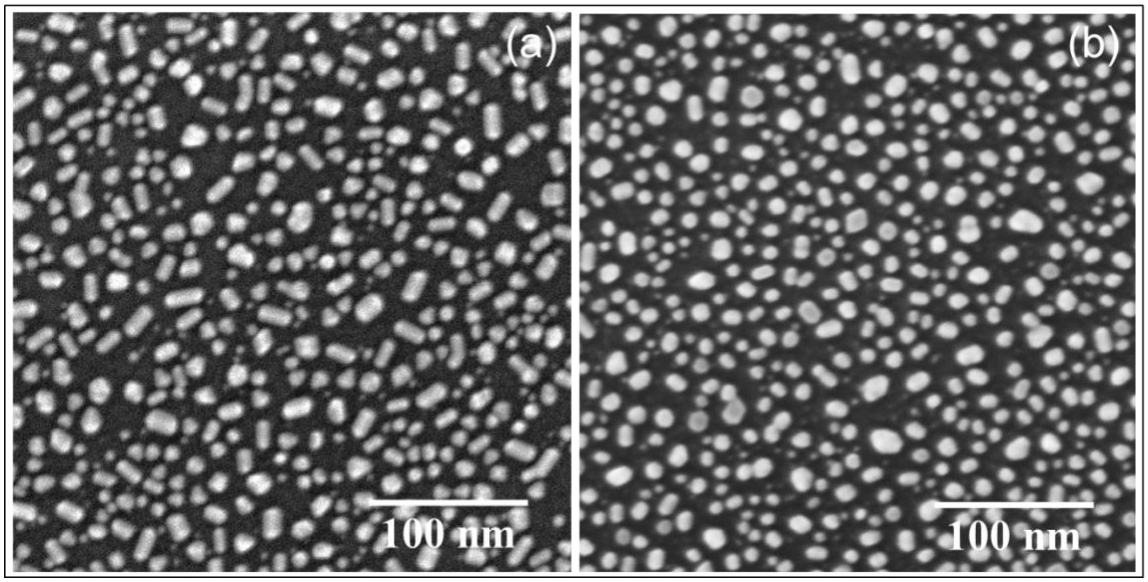

Figure 6.11. SEM images of (a) Pt/TiO_2/HOPG prepared using Ar plasma pretreatment and (b) TiO_2 nanoparticles prepared using O_2 plasma pretreatment

From the SEM images of Figure 6.11, it is observed that the TiO_2 nanoparticles prepared by (a) Ar plasma treatment and (b) O_2 plasma treatment are quite similar in size and morphology. An *ImageJ* analysis revealed average particle diameters of 10.2 ± 8 nm for Figure 6.11a and 9.6 ± 7 nm for Figure 6.11b. Further *ImageJ* analysis also resulted in % areas (i.e. the % HOPG covered by TiO_2 particles) of 27.6% and 29.1% for Figure 6.11a and 6.11b, respectively.

Figure 6.12 shows the D_2O TPD spectra for (a) TiO_2/HOPG prepared with Ar plasma and (b) TiO_2/HOPG prepared with O_2 plasma in which the TPD spectra correspond to the SEM images of Figure 6.11. From Figure 6.12, some similarities and differences are observed in the D_2O thermal desorption spectra. Both spectra exhibit three major desorption states due to Ti^{4+} sites (~250 K), O^{2-} sites (~200 K) and multilayer D_2O (~160 K). The fourth minority desorption state between 150 and 200 K at low exposures is due to defects generated by O_2 plasma cleaning prior to SEM imaging. Figure 6.13 shows the desorption spectra of Figure 6.12a and 6.12b

overlaid to obtain a clearer comparison of the two surfaces. From Figure 6.13, it becomes clear that the peak temperatures for all of the desorption states described above are in good agreement, suggesting that the same D_2O adsorption sites are present on the surface whether Ar or O_2 plasma is used to prepare the TiO_2 nanoparticles. From Figure 6.13, it also becomes apparent that the relative peak intensities differ between the two TPD spectra. This observation could be rationalized by the sample-to-sample variation, in which it is unsurprising to see slight differences in the desorption spectra. From these results, it is suggested that there exist no major observable changes in the reactivity of TiO_2/HOPG samples prepared by Ar or O_2 plasma treatment, however more precise control over sample preparation would be necessary to elucidate any differences.

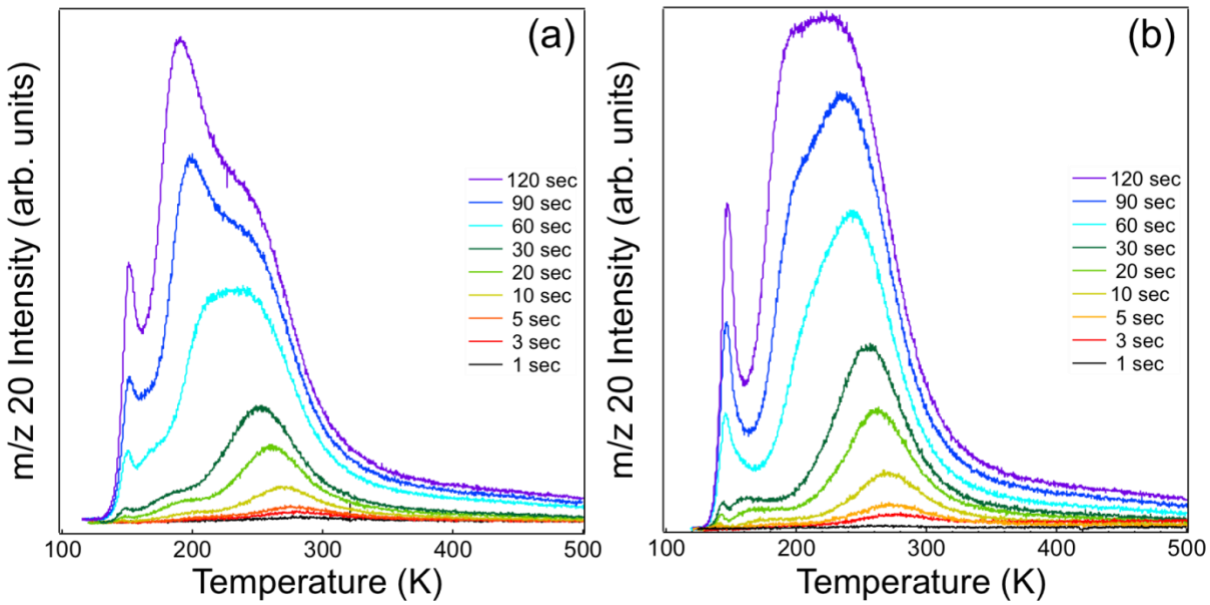

Figure 6.12. TPD spectra for D_2O on TiO_2/HOPG prepared by (a) Ar plasma treatment and (b) O_2 plasma treatment. Exposures (sec) were done with a backing pressure of 1 torr behind the pinhole doser.

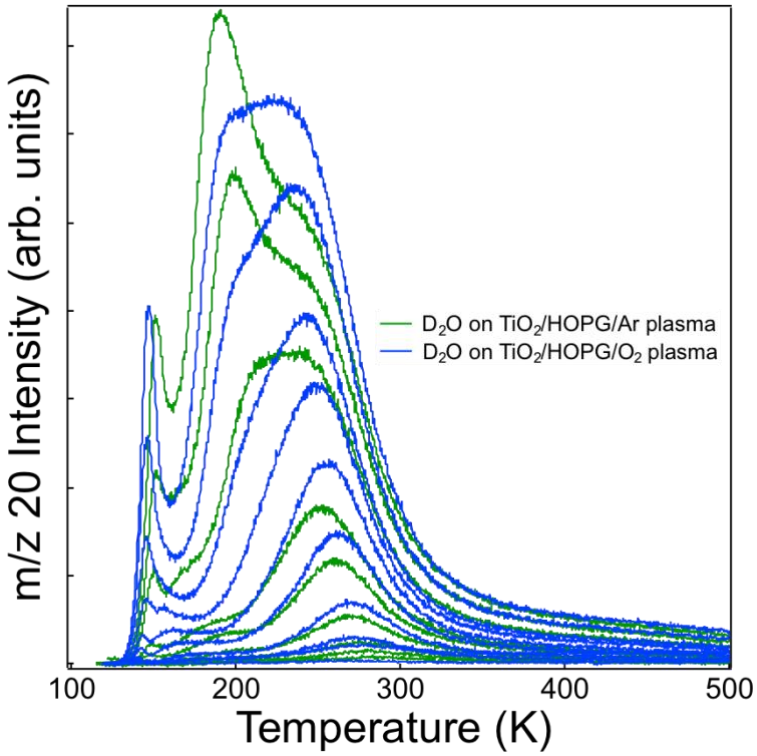

Figure 6.13. Overlay of D_2O on TiO_2/HOPG prepared by Ar plasma treatment (Figure 6.12a) and O_2 plasma treatment (Figure 6.12b).

6.6 Conclusions

This chapter explored the effects of inert (argon) and reactive (oxygen) plasma treatment on three different systems. For a first fundamental approach, the reactivity of D_2O on Ar and O_2 plasma treated HOPG was investigated and compared to that of freshly cleaved HOPG. From the results, it is concluded that both Ar and O_2 induce defects on the HOPG surface that facilitates D_2O adsorption however, O_2 plasma acts to functionalize the surface with oxide species that promote hydrogen bonding of water (D_2O). To understand the effect of O_2 plasma on surface reactivity, D_2O TPD was performed on a TiO_2/HOPG sample before and after O_2 plasma cleaning. The results suggest that O_2 plasma again induces defects with oxygen functionality that present in the form of an additional peak in the thermal desorption spectrum between 160 – 200 K. In addition, a noticeable increase in the relative peak intensities are likely the result of the removal of adventitious carbon on the nanoparticle surface that creates more adsorption sites for D_2O to bind. Furthermore, the effect of oxygen versus argon plasma on the reactivity of TiO_2 nanoparticles supported on HOPG was investigated. The results display some slight differences in the thermal desorption spectra for TiO_2 grown on Ar plasma treated versus O_2 plasma treated HOPG. However, based on the similarity displayed in the SEM data and the inherent variation between prepared TiO_2 samples, there is not enough evidence to support any real changes in the D_2O reactivity on the surfaces.

6.7 References

1. O'Kane, D. F. & Mittal, K. L. Plasma cleaning of metal surfaces. *J. Vac. Sci. Technol.* **11,** 567–569 (1974).
2. Baker, M. A. Plasma cleaning and the removal of carbon from metal surfaces. *Thin Solid*

Films **69,** 359–368 (1980).

3. Gerenser, L. J. Photoemission investigation of silver/poly(ethylene terephthalate) interfacial chemistry: The effect of oxygen-plasma treatment. *J. Vac. Sci. Technol. A Vacuum, Surfaces, Film.* **8,** 3682–3691 (1990).
4. Gerenser, L. J. X-Ray photoemission study of plasma modified polyethylene surfaces. *J. Adhes. Sci. Technol.* **1,** 303–318 (1987).
5. Lee, S. D., Sarmadi, M., Denes, F. & Shohet, J. L. Surface modification of polypropylene under argon and oxygen-RF-plasma conditions. *Plasmas Polym.* **2,** 177–198 (1997).
6. Chakarov, D., Österlund, L. & Kasemo, B. Water adsorption on graphite (0001). *Vacuum* **46,** 1109–1112 (1995).
7. Clemens, A., Hellberg, L., Grönbeck, H. & Chakarov, D. Water desorption from nanostructured graphite surfaces. *Phys. Chem. Chem. Phys.* **15,** 20456 (2013).
8. Hugenschmidt, M. B., Gamble, L. & Campbell, C. T. The interaction of H,O with a TiO2(110) surface. *Surf. Sci.* **302,** 329–340 (1994).
9. Henderson, M. A. An HREELS and TPD study of water on TiO2(110): the extent of molecular versus dissociative adsorption. *Surf. Sci.* **355,** 151–166 (1996).
10. Henderson, M. A. Structural Sensitivity in the Dissociation of Water on TiO 2 Single-Crystal Surfaces. *Langmuir* **12,** 5093–5098 (1996).

APPENDIX A

List of acronyms

AES – Auger electron spectroscopy

APXPS – ambient pressure X-ray photoelectron spectroscopy

CMA – cylindrical mirror analyzer

DFT – density functional theory

EDS – energy dispersive x-ray spectroscopy

HOPG – highly oriented pyrolytic graphite

LEED – low energy electron diffraction

LEXI – Laboratory for Electron and X-ray Instrumentation

LN_2 – liquid nitrogen

m/z – mass to charge ratio

ML – monolayers

MS – mass spectrometer

NHE – normal hydrogen electrode

PVD – physical vapor deposition

RSF – relative sensitivity factor

RT – room temperature

SEM – scanning electron microscopy

SMSI – strong metal support interaction

SS – stainless steel

STM – scanning tunneling microscopy

TC – thermocouple

TDS – thermal desorption spectroscopy

TEM – transmission electron microscopy

TPD – temperature programmed desorption

TSP – titanium sublimation pump

UHV – ultra-high vacuum

UPS – ultra-violet photoelectron spectroscopy

UV – ultra-violet

XAS – X-ray absorption

XPS – X-ray photoelectron spectroscopy

APPENDIX B

Supporting Information

B.1 Chapter 3 supporting figures

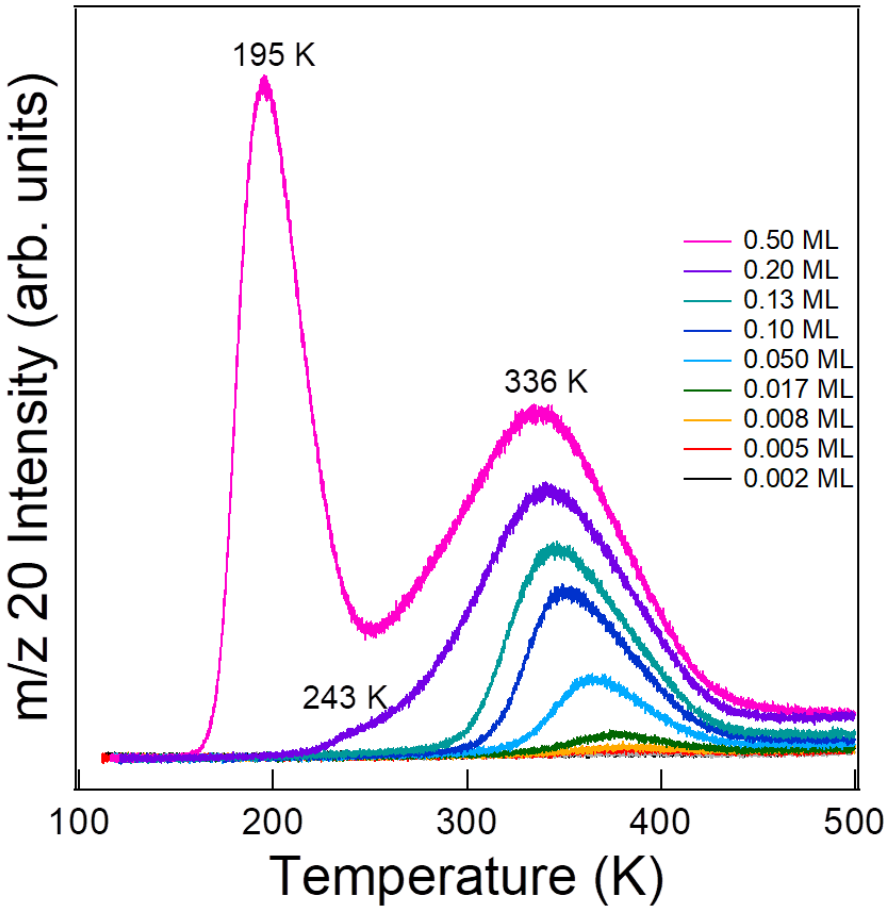

Figure S3.1. TPD spectrum of D_2O desorption from a clean W (100) surface. The peak at 336 K is attributed to D_2O disproportionation, the peak at 195 K is assigned to oxidation of the surface during the experiment. Experiment was performed using a heating rate of 0.5 K/s

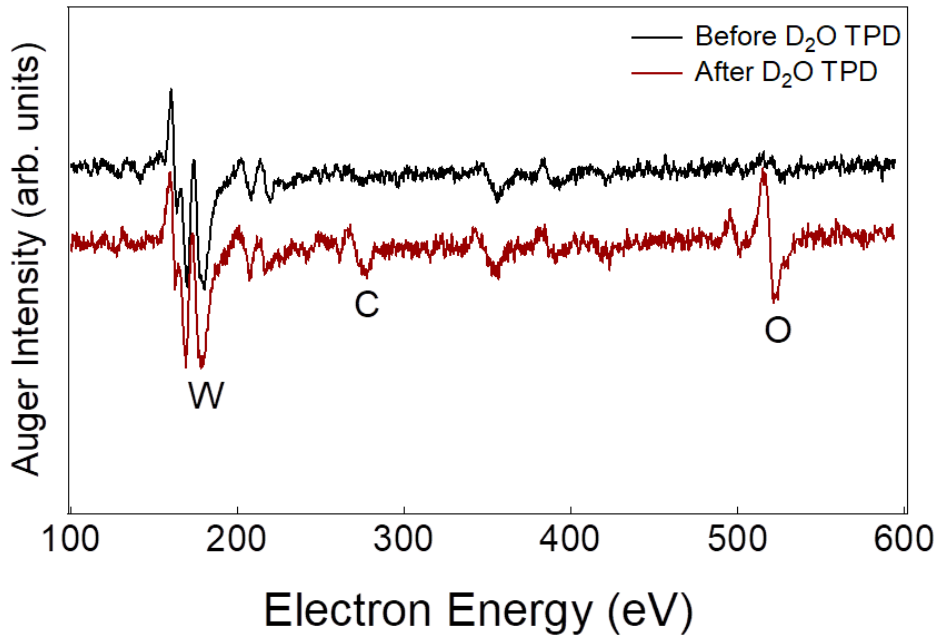

Figure S3.2. AES spectrum showing oxidation of the clean W (100) before (black trace) and after (red trace) D_2O TPD experiment.

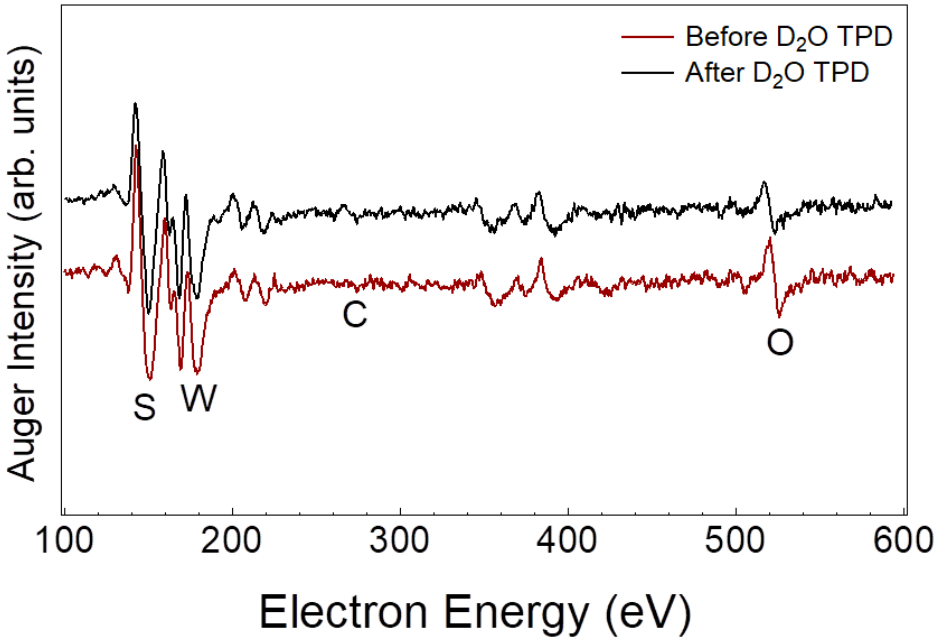

Figure S3.3. AES spectrum showing slight oxidation of the sulfurized W (100) before (black trace) and after (red trace) D_2O TPD experiment.

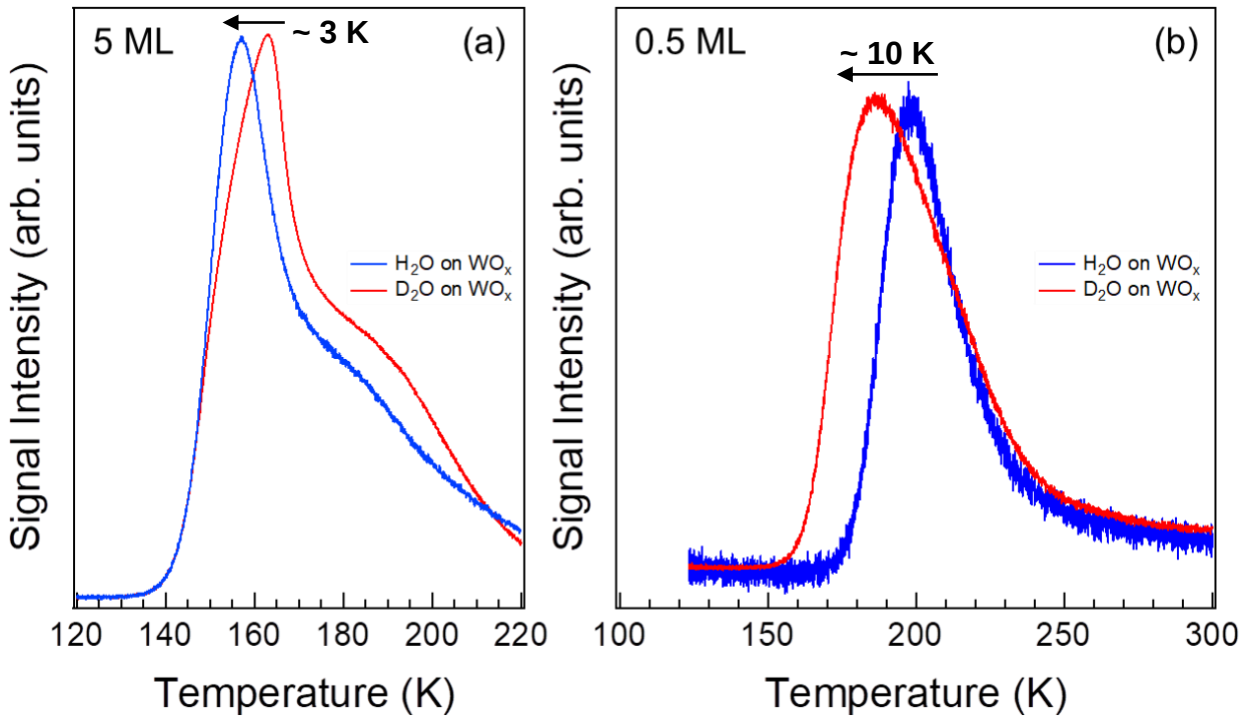

Figure S3.4. Comparison of H_2O (blue traces) and D_2O (red traces) desorption from the oxidized W (100) surface for the (a) multilayer peak (5 ML coverage) and (b) monolayer peak (0.5 ML coverage) and the respective shift in peak temperature (indicated on the individual plots.

B.2 Chapter 4 supporting figures

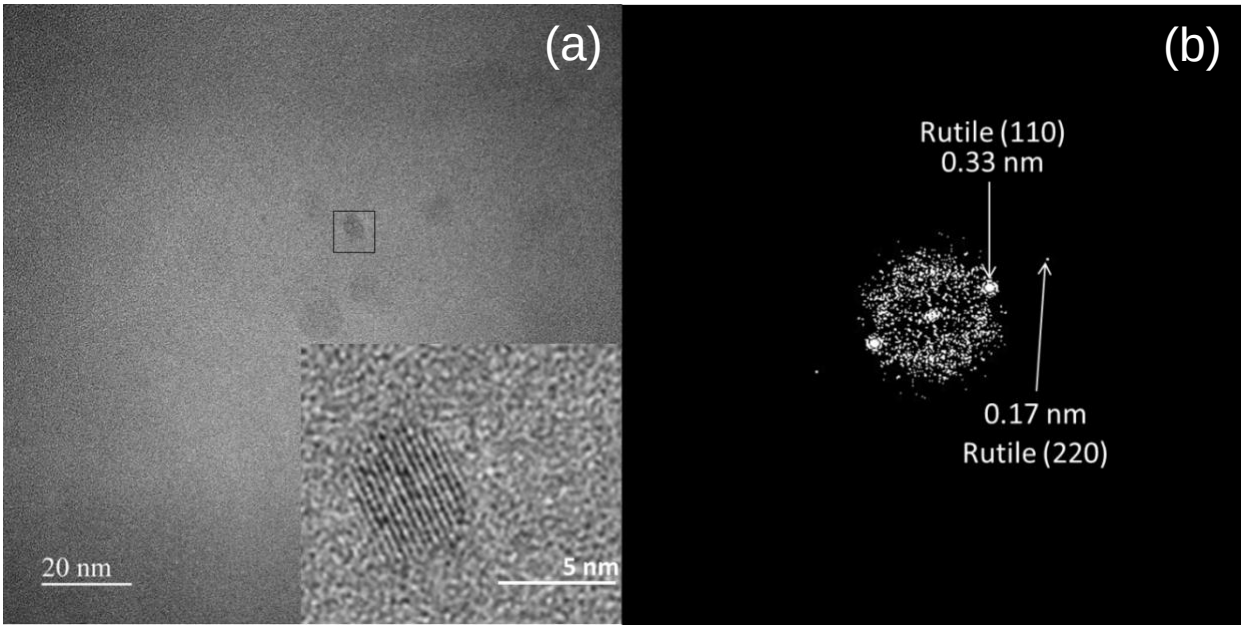

Figure S4.1. (a) TEM image of TiO_2 nanoparticles and (b) TEM diffraction pattern displaying the Rutile phase of TiO_2. The inset of (a) is the blown up portion of the boxed region in which the lattice fringes can be observed.

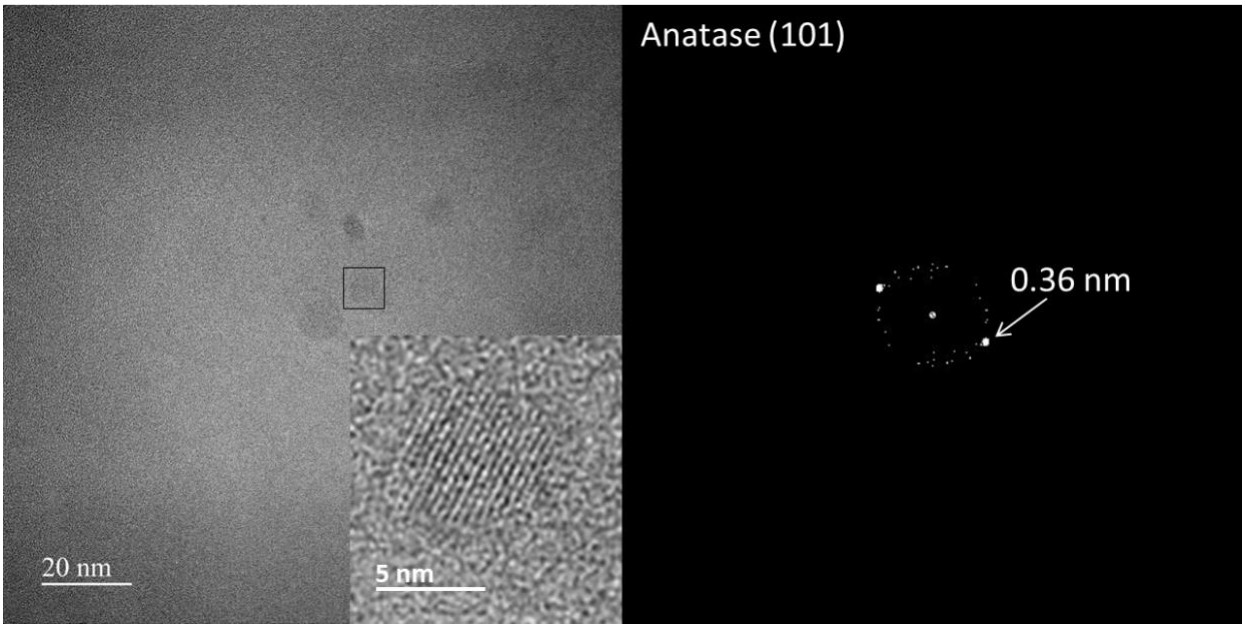

Figure S4.2. (a) TEM image of TiO_2 nanoparticles and (b) TEM diffraction pattern displaying the Anatase phase of TiO_2. The inset of (a) is the blown up portion of the boxed region in which the lattice fringes can be observed.

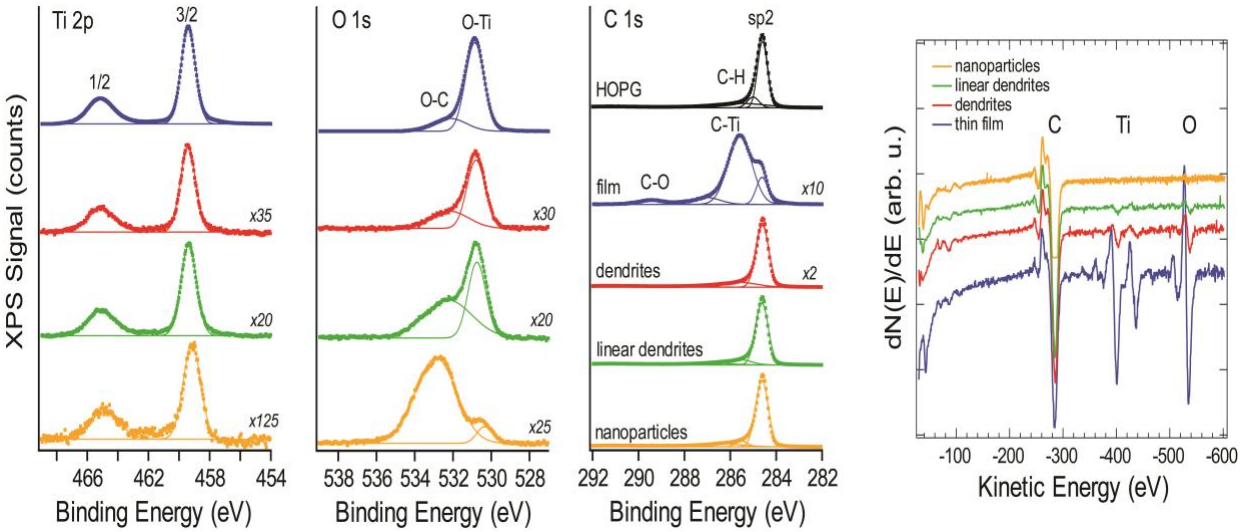

Figure S4.3. XPS and AES data for nanoparticles (gold), linear dendrites (green), dendrites (red), and thin film (blue). XPS data shows the Ti 2P region, O1s region and C1s regions. The peaks for C, Ti, and O are labeled on the AES spectrum.